TÉCNICO LISBOA

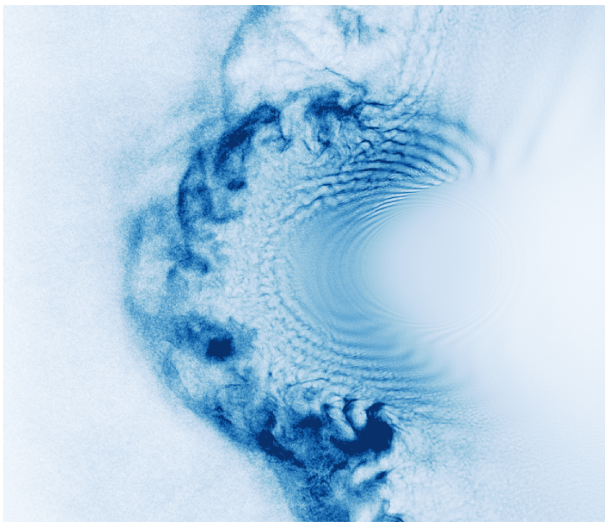

Mini magnetospheres in the laboratory

Filipe da Silva Duarte Cruz

Thesis to obtain the Master of Science Degree in

Engineering Physics

Supervisors: Dr. Fábio Alexandre Lopes Cruz
Prof. Luís Miguel de Oliveira e Silva

Examination Committee

Chairperson: Prof. João Alberto dos Santos Mendanha Dias
Supervisor: Dr. Fábio Alexandre Lopes Cruz
Member of the Committee: Prof. Marta Leitão Mota Fajardo

May 2022

I declare that this document is an original work of my own authorship and that it fulfills all the requirements of the Code of Conduct and Good Practices of the Universidade de Lisboa.

Declaro que o presente documento é um trabalho original da minha autoria e que cumpre todos os requisitos do Código de Conduta e Boas Práticas da Universidade de Lisboa.

Acknowledgments

I would like to thank:

My supervisors Dr. Fábio Alexandre Cruz and Prof. Luís Oliveira e Silva, for their guidance through this project and for the opportunities they made available to me.

Dr. Derek Schaeffer for the guidance and the collaboration with the experiments performed at the LAPD.

Everyone at GoLP, for the great working environment and for introducing me to research in plasma physics.

To the IST cluster (Lisbon, Portugal) and PRACE for awarding access to MareNostrum (Barcelona Supercomputing Center, Spain), where most of the simulations presented in this Thesis were performed.

To my friends and family for the support during all these years, in particular, to Óscar, Gonçalo, Tiago, and Diogo for the very interesting discussions and for the feedback during the development of this work.

Resumo

"Mini magnetosferas" à escala iónica fornecem um meio único para estudar física de plasmas à escala cinética e foram observadas à volta de cometas, asteróides fracamente magnetizados, e regiões localizadas da Lua. Nesta Tese, apresentamos simulações *particle-in-cell* (PIC) não colisionais de magnetosferas à escala iónica que reproduzem recentes experiências em laboratório realizadas no Large Plasma Device (LAPD) na UCLA. Nas nossas simulações PIC, um plasma impulsionador super-Alfvénico flui contra um campo magnético dipolar que está incorporado num plasma ambiente uniforme e magnetizado. As simulações replicam as principais estruturas magnetosféricas observadas nas experiências, nomeadamente a magnetopausa à escala cinética e as distribuições de corrente do plasma. As propriedades de mini magnetosferas criadas nesta interação são estudadas para diferentes parâmetros do dipolo e do plasma, e simulações PIC são utilizadas para extrair observáveis chave para as experiências e as condições em que se formam.

Adicionalmente, também desenvolvemos um modelo semi-analítico dos parâmetros que caracterizam o acoplamento entre os plasma impulsionador e ambiente. O modelo semi-analítico é comparado com as simulações, mostrando boa concordância. O modelo é também usado para fornecer limites para os parâmetros experimentais, tais como as densidades dos plasmas.

Palavras-chave: mini magnetosferas, acoplamento de plasmas, simulações PIC, astrofísica no laboratório, física do espaço

Abstract

Ion-scale “mini magnetospheres” provide a unique environment for studying kinetic-scale plasma physics and have been observed around comets, weakly-magnetized asteroids, and localized regions of the Moon. In this Thesis, we present collisionless particle-in-cell (PIC) simulations of ion-scale magnetospheres that reproduce recent laboratory experiments performed in the Large Plasma Device (LAPD) at UCLA. In our PIC simulations, a super-Alfvénic driver plasma flows against a dipolar magnetic field that is embedded in a uniform magnetized background plasma. The simulations replicate the main magnetospheric structures observed in the experiments, namely the kinetic-scale magnetopause and the plasma current distributions. The properties of mini magnetospheres created in this interaction are studied for different dipole and plasma parameters, and PIC simulations are utilized to extract key observables for the experiments and conditions in which they form.

Additionally, we develop a semi-analytical model of the parameters that characterize the coupling between the driver and the magnetized background plasmas. The semi-analytical model is compared with the simulations, showing good agreement. The model is also used to provide bounds for the experimental parameters, such as the densities of the plasmas.

Keywords: mini magnetospheres, plasma coupling, PIC simulations, laboratory astrophysics, space physics

Contents

List of Tables

List of Figures

Nomenclature

Greek symbols

α	Compression ratio.
β_e	Ratio of electron plasma pressure to magnetic pressure.
ω_{ci}	Ion cyclotron frequency.
ω_{pe}	Electron plasma frequency.
ρ_i	Ion gyroradius.
Φ	Energy flux.
Δ	Variation / Magnetic field ramp width of magnetic cavity to magnetic compression.
δ	Regularization parameter.

Roman symbols

v_0	Fluid velocity.
v_ϕ	Phase velocity.
v_c	Coupling velocity.
v_f	Front velocity.
B	Magnetic Field.
E	Electric field / Energy.
J	Density current.
P	Pressure.
W	Energy.
L_0	Standoff distance.
L_{stop}	Maximum length of the magnetic cavity.
L_x	Length of the driver plasma.

L_y Width of the driver plasma.

M Magnetic moment of the dipole.

M_0 Standard magnetic moment of the dipole.

c Light speed in vacuum.

c_s Sound speed of medium.

e Electron charge.

r Distance to the dipole.

m Mass of each component.

n Plasma density.

t Time.

d_i Ion skin depth.

A_T Area transverse to the plasma flow.

M_A Alfvénic Mach number.

R_n Quantity defined from the driver and background densities and ion masses.

T Temperature.

Subscripts

fl Fluid component.

th Thermal component.

x, y, z Cartesian components.

A Alfvén.

dip Dipolar.

ini Initial.

e Electrons.

i Ions.

0 Background plasma.

d Driver plasma.

ele Electric field.

mag Magnetic field.

Superscripts

’	Parameter after interaction / Parameter in reference frame of discontinuity.

Acronyms

CGS Centimeter-gram-second system of units.

GoLP Group of Lasers and Plasmas.

IST Instituto Superior Técnico.

LAPD LArge Plasma Device — 20 m long, 1 m diameter, cylindrical facility for general-purpose research in plasma physics at UCLA.

LULI Laboratoire pour l'Utilisationdes Lasers Intenses (Laboratory for the User of Intense Lasers).

MHD Magnetohydrodynamics.

MS Magnetosonic.

OSIRIS A massively parallel fully relativistic 3D electromagnetic PIC code, developed by GoLP and a team in UCLA.

PIC Particle-in-cell — kinetic codes that resolve the dynamics of plasmas, by considering macro-particles in a electromagnetic field grid.

RAL Rutherford Appleton Laboratory.

RH Rankine-Hugoniot jump conditions.

UCLA University of California, Los Angeles.

Chapter 1

Introduction

1.1 Motivation

A vast range of space and astrophysical scenarios are driven by the rapid expansion of plasmas, gases with free ions and electrons, through space. Such examples include interplanetary coronal fast ejecta [1], the expansion of the stellar material from supernovae remnants [2], and artificial magnetospheric releases of tracer ions [3]. When these expanding plasmas encounter obstacles of magnetic nature, the resultant interaction leads to highly nonlinear and complex dynamics.

In the solar system, the upper region of the Sun's atmosphere is continuously expanding at velocities close to 400 km s^{-1}, which can lead to similar scenarios in space. This results in the emission of a plasma, designated by solar wind [4], that near the Earth has a density of a few particles per cm^3. This plasma travels through interplanetary space, interacting with planets, satellites, and other smaller objects, and it is very dynamic as its density, temperature, and speed change in space and time.

As it approaches the Earth, it is under the effect of the strong magnetic fields associated with Earth's intrinsic magnetic field structure. The fields are strong enough to significantly reduce the velocities of solar wind particles and deflect them around the Earth. Plasmas also pile up in this interaction, forming a compressed bow-shaped region called the bow shock. As the plasma gets even closer, the magnetic field increases until the magnetic pressure is enough to stop the plasma particles, forming a rarefied plasma surrounding the Earth. The region where the magnetic field dominates the pressure exerted by the solar wind is designated by **magnetosphere**.

Even though the magnetosphere is a tenuous plasma region in space, with a density close to 50 particles per cm^3 [5], it prevents the solar wind from reaching the atmosphere and protects the surface from the hazard radiation and energetic particles emitted by the Sun, that could otherwise compromise life on Earth. Additionally, as the solar wind leads to sudden changes in the magnetic field, the magnetosphere prevents magnetic disturbances that could trigger large voltages on power grids, pipelines, and transoceanic cables, which could seriously affect human activities. Figure 1.1 illustrates Earth's magnetosphere.

The region of space where the pressure exerted by the solar wind equals the pressure exerted by the Earth's magnetic field, which defines the region of the immobilization of the plasma, is designated by

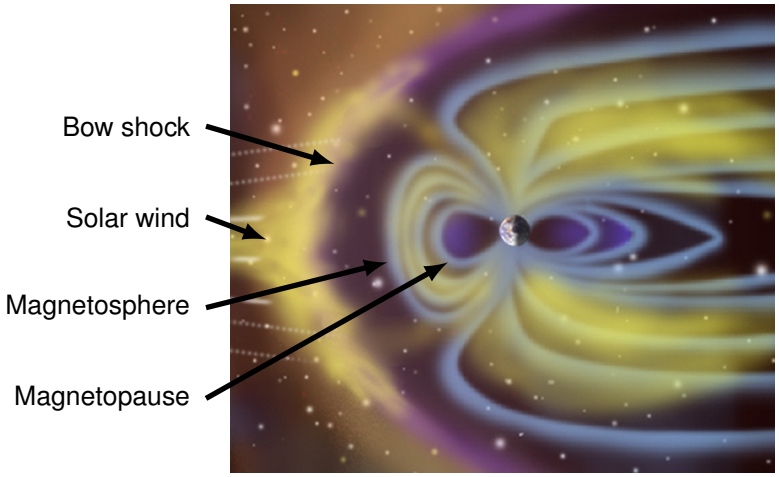

Figure 1.1: Representation of Earth's planetary magnetosphere and identification of its main features. The blue lines represent magnetic field lines. Original image from NASA.

magnetopause and determines the effective radius of the magnetic obstacle associated with the magnetosphere. This pressure equilibrium can be described approximately by the magnetohydrodynamics (MHD) formalism [6], and it is expressed in CGS units by $n_0 m_i v_0^2 = B^2/8\pi$, where the left-hand side represents the plasma ram pressure, with density n_0, ion mass m_i, and fluid velocity v_0, and the right-hand side represents the pressure associated with the magnetic field B. For the Earth, the magnetic field is approximately dipolar, described by $B_{\text{dip}} = M/r^3$, where $M \approx 7.95 \times 10^{22}$ A m^2 is the magnetic moment, and r the distance to the dipole, resulting in magnetic fields close to 50 µT at the Earth's surface [7]. The distance at which we obtain the pressure balance determines the effective magnetic obstacle radius designated by standoff distance L_0, which is close to 65 000 km (around 10 Earth radii) for the Earth.

When the standoff distance L_0 is of the same order as the typical ion kinetic scales of the plasma, *i.e.*, comparable to the ion gyroradius and/or the ion skin depth, the magnetospheres formed are designated by mini magnetospheres. Mini magnetospheres occur at much smaller scales, unlike the planetary magnetospheres, such as Earth's, where the obstacle size is around a hundred times larger than the gyroradius.

Additionally to Earth's magnetic field, the internal magnetic field B_0 of the solar wind plasma is also present. The properties of the plasma flow can be summarized in its Alfvénic Mach number, defined as $M_A \equiv v_0/v_A = v_0\sqrt{4\pi n_0 m_i}/B_0$, and corresponds to the ratio between the fluid velocity v_0 and the Alfvén velocity v_A, related to the information travel speed of magnetized media. In large-scale magnetospheres, plasmas can be divided in the super-Alfvénic ($M_A > 1$) unperturbed plasma flow of the solar wind, and the sub-Alfvénic ($M_A < 1$) turbulent flow surrounding the Earth [8].

1.1.1 Observations and futuristic applications of mini magnetospheres

The study of mini magnetospheres in past years was mainly motivated by the observation of crustal magnetic anomalies on the lunar surface [9–13]. Although the Moon does not have a global magnetic field like Earth, it does have small localized regions of crustal magnetic field of 10–100 nT over distances of 100–1000 km [9], which are of the same order of magnitude as the gyroradius of solar wind ions near

the Moon's surface. As a result, when these regions of the lunar surface are exposed to the solar wind, mini magnetospheres can form.

Mini magnetospheres are closely related to the "lunar swirls" structures observed on the Moon's surface [13, 14], which have been associated with magnetic anomalies. As the solar wind gets under the effect of the magnetic field of these anomalies, it starts to be deflected, leading to side regions that are under a high exposure of the solar wind, and regions below the magnetic cavity with a low concentration of plasma. As a result, the regions of the lunar surface that are shielded from the solar wind bombardment are surrounded by darker regions due to the increased erosion by the solar wind. An example of a lunar swirl is shown in Figure 1.2.

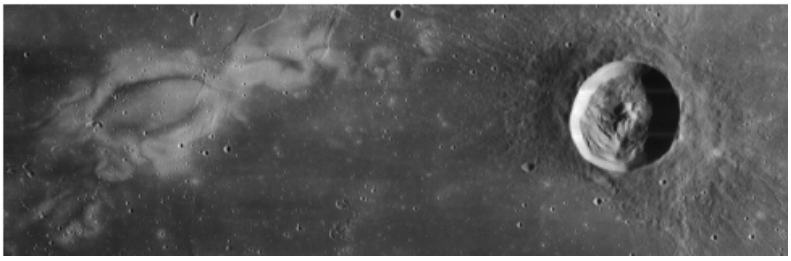

Figure 1.2: The Reiner Gamma formation, an example of a lunar swirl, pictured on the left side of the image. The formation is named after the Reiner impact crater, shown on the right, at a distance of 117 km to the east, and has a diameter of 30 km [14].

Other interactions between the solar wind and small-sized patches of magnetic field also occur in other regions of the solar system. Such examples include Mars [15], where the induced magnetosphere interacts with the crustal fields; Mercury [16] and Ganymede [17], where the small magnetospheres interact with the solar wind and Jupiter's magnetosphere, respectively, and comets and asteroids [18], when interacting with the solar wind.

The concept of shielding in the magnetic-dominated region of mini magnetospheres can be extended to multiple futurist applications. One of the most interesting proposals consists in using mini magnetospheres to protect spacecrafts from energetic particles, which would allow human space exploration for long term missions [19, 20]. Such design would be highly effective, as it would not need to stop the interplanetary plasma particles, only deflecting them instead. It would also be preferable to the purely proposed electromagnetic deflector shields, as the efficiency can be boosted with the addition of plasma to the shield.

A concept of mini magnetospheric plasma propulsion for spacecrafts was also proposed [21]. Such a prototype would create a magnetic bubble around a spacecraft, deflecting and picking up the momentum from the solar wind high velocities particles. It would require a low power consumption and only a few mechanical structures and could reach velocities higher than 50 km s^{-1}.

After the different observations of the ion-scale magnetospheres in the solar system and the revolutionary applications that these systems could bring for space exploration, the astrophysical and plasma community performed multiple studies with simulations and in laboratories to improve our knowledge of the formation of these systems. In our work, we explore multiple simulations of mini magnetospheres in laboratory plasmas and resort to analytical models to determine the necessary conditions for the

formation of magnetospheric characteristics in laboratory configurations.

1.2 State of the art

1.2.1 Efforts in reproducing space and astrophysical scenarios in the laboratory

The observations made with space probes of mini magnetosphere systems, although useful to understand the interaction of space plasmas with magnetic obstacles, have multiple limitations. These include the limited accessible space regions that can be studied and the difficulty in performing high-resolution measurements. To complement these studies, the space and astrophysics plasma communities have attempted, over the last decades, to perform laboratory experiments that would reproduce diverse space and astrophysical scenarios.

Such attempts achieved significant progress, for example, in the RAL Space, at the Rutherford Appleton Laboratory [22], in the Large Plasma Device (LAPD) at the University of California, Los Angeles [23], and in the Laboratoire pour l'Utilisationdes Lasers Intenses (LULI) at École Polytechnique, in France [24]. In such experiments, explosive, laser-produced debris plasmas, designated as driver plasmas, and preformed, magnetized ambient plasmas, designated as background plasmas, were created to replicate space and astrophysical scenarios, such as the ones observed in the expansion of stellar material through the surrounding interstellar medium in supernova remnants and the interaction of interplanetary coronal mass ejections with the Earth's magnetosphere. The fast-moving plasma flows are usually driven by resorting to high-intensity lasers focused onto solid targets of plastic or metal composition [25–27]. These laser-ablated plasmas can be mildly collisional or collisionless, replicating astrophysical conditions [28–31].

To ensure that these experiments could be properly executed, many studies focused on the coupling between the laser-driven plasma and the preformed magnetized plasma to ascertain if the driver plasma could transfer enough energy in the laboratory and allow the study of astrophysical scenarios. Such experiments studied the different coupling regimes observed in the laboratory [32, 33] and the physics of the coupling [29, 34, 35]. By adding dipole field sources against the plasma flows, we can study mini magnetospheres in the laboratory. Previous experiments studied possible applications for spacecrafts [19, 22, 36], the formation of lunar swirls [14], and the conditions for the formation of magnetosphere features [6, 24, 37, 38]. Although these experiments achieved important breakthroughs in the study of ion-scale magnetospheric physics, they were limited to i) 1D measurements of the magnetic field and plasma density profiles and ii) fixed properties of the obstacle and plasma flow.

1.2.2 Recent LAPD experiments with ion-scale magnetospheres

To overcome the limitations of previous experiments with mini magnetospheres, a new experimental platform to study ion-scale magnetospheres was recently developed in the LAPD [39]. In these experiments, fast collisionless plasma flows generated by high-repetition-rate lasers were collided with the magnetized ambient plasma provided by the LAPD and with a dipolar magnetic field obstacle, leading to the formation of ion-scale magnetospheres. Using motorized probes, high spatial and temporal

resolution measurements of the magnetic field allowed the characterization of 2D magnetic field and current density structures. The goals of these new experiments are to study the formation and structure of laser-driven ion-scale magnetospheres, the effect of magnetic reconnection on magnetosphere dynamics, and the generation of bow shocks.

In these LAPD experiments, a laser-driven plasma expands into a dipole magnetic field embedded in an ambient magnetized plasma (see Figure 1.3) so that the total magnetic field topology is analogous to that of the Earth's magnetosphere. In Figure 1.4, we can observe the first results of these experiments, which focused on the formation of magnetosphere structures with sub-Alfvénic flows.

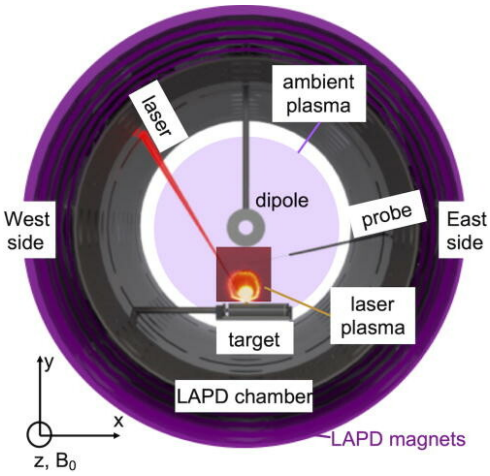

Figure 1.3: Schematic of the experimental setup on the LAPD [39]. A laser ablates a plastic target to create a supersonic plasma flow, which flows toward a dipole magnet inserted into the LAPD from the top. The dipole magnet is embedded in a uniform magnetized background plasma generated by the LAPD. Probes inserted from the east port collect volumetric data from the regions around the dipole. A fast-gate image shows the expansion of the laser-driven plasma.

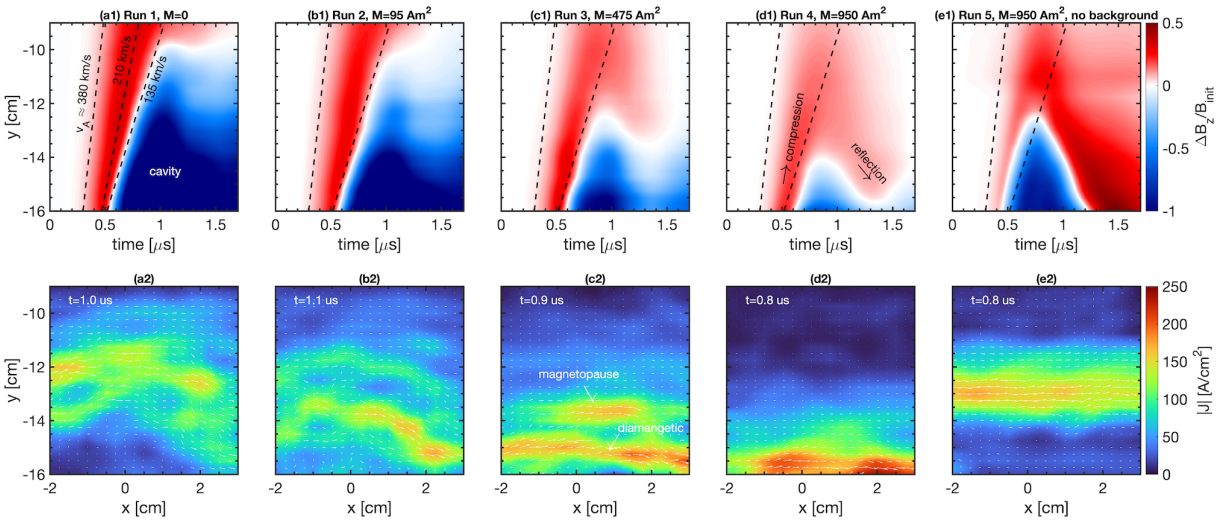

Figure 1.4: Main results of the LAPD experiments [39]. (Top panels) Dayside magnetic field streak plots along y in the plane perpendicular to the field $\{x, z\} = \{0.75, 0\}$ cm for different dipole magnetic moments M. In (e), there is no background plasma or magnetic field B_0. The colorbars are saturated to make features clearer. (Bottom panels) 2D contour plots of the derived dayside current density in the x–y plane, taken at the time of peak current for each M. Overplotted is the current density vector field (white arrows).

Figure 1.4 shows the magnetic field variation and the current density structures for different dipolar magnetic moments. We can observe the formation of a magnetic cavity upstream and a magnetic compression downstream, and for most cases, a reflection of the magnetic compression. In the current plots, we observe the formation of two current structures near the dipole [39].

Because the dimensions of space and astrophysical plasma physics are much higher than the dimensions in the laboratory, the parameters for the experiments require proper rescaling [40] so that the main parameter relations in space scenarios, such as the ratio between the standoff distance and the ion gyroradius or the ion skin depth, remain the same. These include, for example, increasing the magnetic field and the plasma densities in the laboratory. Furthermore, in these experiments, the system parameters must ensure that the coupling between the driver and background plasmas is sufficient to observe the astrophysical scenarios being studied. The understanding of the coupling mechanism is, therefore, of high interest for the design of laboratory experiments of space scenarios.

1.2.3 Analytical work

Multiple analytical calculations were performed to interpret the physics of the interaction between collisionless plasmas and miniature obstacles. The first attempts used the MHD formalism, consisting of the macroscopic description of plasma as a single electrically charged fluid subject to the presence of self-consistent and external magnetic fields. Using the MHD equations, the balance between the plasma pressure and the magnetic field pressure allowed us to obtain a good estimate of the standoff distance of mini magnetospheres [6].

Furthermore, the MHD equations can also be used to understand the interaction of an expanding unmagnetized driver plasma with a magnetized background plasma, which commonly occurs in the laboratory and astrophysical scenarios, such as in ion-scale magnetospheres. When we have a discontinuity separating two plasmas with different properties, the relationship between the states of both sides of the discontinuity obeys the Rankine-Hugoniot (RH) jump conditions [8], which can be used to evaluate the coupling between the two plasmas.

By considering hybrid models, where the ion species are treated kinetically and the electrons as a charge-neutralizing fluid, other works were able to calculate the electric field that describes the collisionless coupling between the expanding and the magnetized plasmas, *i.e.*, the efficiency of energy and momentum transfers between the two plasmas [29, 30]. For super-Alfvénic and magnetically dominated plasmas, this electric field provides the dominant coupling mechanism. It was also possible to conclude that the increase of the density ratio between the driver and background plasma improves the plasma coupling [41].

Other analytical works focused on calculating the changes to the system parameters during the driver-background interaction [34] and on calculating the spatial scales of the interaction, more specifically, the size of the magnetic cavity created by the driver plasma [42]. As the driver expands against the magnetized background, it expels the magnetic field, which can lead to a magnetic cavity of almost null magnetic field [34]. By considering energy conservation arguments, multiple attempts were made to calculate the maximum extent of this cavity [36, 43–47].

1.3 Simulations and the particle-in-cell method

The interaction of plasma flows with magnetic obstacles is a highly nonlinear process [8]. Numerical simulations are therefore essential in complementing the study from analytical and experimental research, as they can resolve the dynamics of such systems and play a key role in interpreting and designing experiments [48].

Early MHD simulations attempted to explain the formation and characteristics of lunar ion-scale magnetospheres and validate experimental and analytical models [37, 49, 50]. Hybrid simulations were used to study the role of ion kinetic effects, obtain conditions for the formation of magnetospheres [51], and replicate previous experimental results [52]. However, these simulations do not resolve the electron scales nor capture important kinetic effects on the magnetosphere's boundary, e.g. charge separation effects and nonthermal particle distributions, that are necessary to resolve these systems [8].

For collisionless electron kinetic-scale systems, particle-in-cell (PIC) codes are ideal numerical methods, and they were already used to study the formation of ion-scale magnetospheres [8, 48]. The PIC method consists of self-consistently solving the equations of motion for all the particles in a discretized spatial grid [53]. In PIC codes, the numerical particles represent an ensemble of real particles, called macro particles, which are initialized in the grid. From the macro particles' position and velocity, $\mathbf{x_p}$ and $\mathbf{v_p}$, the charge and current densities, ρ and $\mathbf{J}$, are deposited at the grid cells' edges, from which the electric and magnetic fields, $\mathbf{E}$ and $\mathbf{B}$, are calculated using Maxwell's equations. The fields are then interpolated to the velocities, and these are updated in time by integrating the relativistic equation of motion with the Lorentz force. This loop process is repeated for each simulation time step, as represented in Figure 1.5.

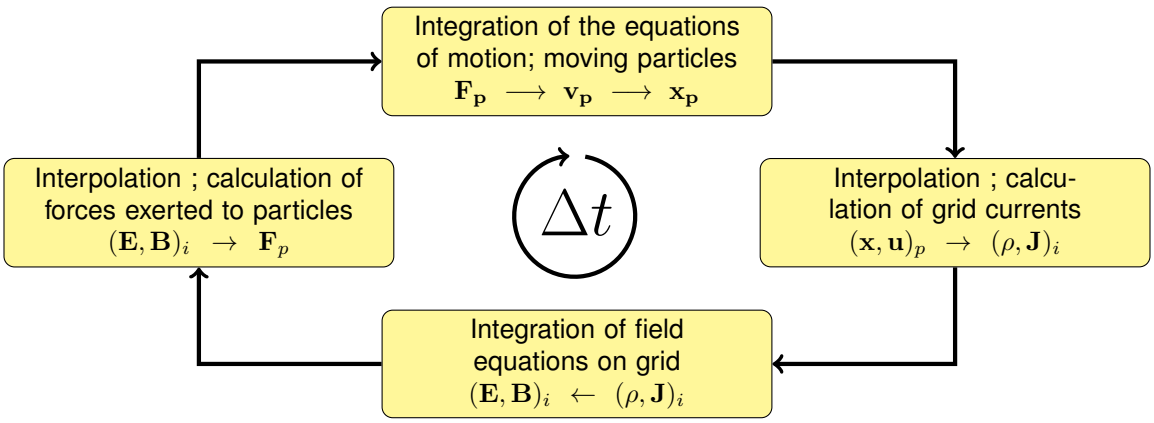

Figure 1.5: Scheme of a typical cycle of the PIC algorithm [53]. The quantities are represented for a particle p and grid cell i.

Because the PIC method does not apply fluid and collective approximations that would compromise the observation of the microphysical processes associated with kinetic scale plasmas, it is ideal for studying mini magnetospheres, of kinetic-scale and collisionless nature.

Previous studies used fully kinetic simulations, such as PIC, to study mini magnetospheres. The first works studied the formation of lunar mini magnetospheres and confirmed that the lunar magnetic anomalies are strong enough to standoff the solar wind [54–56] and that kinetic effects play important

roles in the properties of the lunar plasma environment [57, 58]. In more recent works, PIC simulations were employed to study the formation of collisionless shocks in mini magnetospheres [59]. They successfully obtained conditions for shock formation and different regimes of the magnetic obstacle size for the motion of the particles. Other studies also concluded that the obstacle size is dependent on the relative orientation of the magnetic fields [60].

1.4 Objectives

The goal of this Thesis is to determine the main characteristics of ion-scale magnetospheres in the laboratory in a similar configuration to the recent LAPD experiments described in Section 1.2.2. We aim to validate the experimental results and method and understand the evolution of the system and the formation of the different structures observed. By performing different parameter scans and configurations with simulations, we also aim to understand how each parameter of the system affects the experimental results and outline the necessary conditions that future experiments must obey to observe the features observed in the experiments.

To better understand the interaction of the experimental plasmas with the magnetospheric obstacle, we also aim to understand the interaction between the commonly used laser-driven and background plasmas. To achieve this, we attempt to describe the interaction of the plasmas analytically and apply these results to the study of mini magnetospheres.

1.5 Outline

The work developed for this Thesis is focused on determining the characteristics of ion-scale magnetospheres performed in the laboratory. To fully understand the evolution of these systems, we need to understand these systems under different parameter regimes and how the system behaves under a simplified configuration, where no magnetospheric obstacle is present.

In Chapter 2, we study the coupling, *i.e.*, the energy and momentum transfer efficiency between a moving plasma and a magnetized plasma, before studying magnetospheric configurations. From multiple 1D PIC simulations, we discover how these systems typically evolve under different regimes of parameters, and from conservation laws, we determine analytical expressions for average quantities that describe these simulations. We also compare the expressions obtained in this Chapter with previous works in the literature and verify, for certain ranges of parameters, that our equations are substantially more accurate.

The main results and characteristics of 2D PIC simulations of ion-scale magnetospheres in laboratory plasmas are studied in Chapter 3. We replicate the main results of the LAPD experiments presented in Section 1.2.2 and successfully validate the formation of ion-scale magnetospheres in the laboratory. By determining the different pressures that arise in the simulations, we study the formation of a magnetopause and derive analytical expressions for the pressure balances that describe the system.

To better understand the role of each parameter of the system, Chapter 4 shows the results of multiple parameter scans for the simulations of ion-scale magnetospheres. We determine how the system changes with the different plasma and dipole parameters and the conditions that these parameters must

obey to ensure the formation of the main characteristics discussed in Chapter 3. At the end of the Chapter, we test the validity of some simplifications assumed in most simulations by performing new simulations with more realistic configurations.

Finally, the conclusions of this Thesis and future work are presented in Chapter 5. In Appendix A, we derive some of the equations presented in Chapter 2, and in Appendix B, we show a list of the main simulations performed with mini magnetospheres and compare the parameters of these simulations with the experiments and space observations.

1.6 Original Contributions

- Posters:
  - F. D. Cruz, D. B. Schaeffer, F. Cruz, R. S. Dorst, P. V. Heuer, C. G. Constantin, P. Pribyl, C. Niemann, A. Bhattacharjee, and L. O. Silva. Particle-in-cell simulations of laser-driven, ion-scale magnetospheres in laboratory plasmas. *62nd Annual Meeting of the APS Division of Plasma Physics*, Remote, VP12.5, 2020.
  - F. D. Cruz, D. B. Schaeffer, F. Cruz, R. S. Dorst, P. V. Heuer, C. G. Constantin, P. Pribyl, C. Niemann, A. Bhattacharjee, and L. O. Silva. Particle-in-cell simulations of laser-driven, ion-scale magnetospheres in laboratory plasmas. *47th EPS Conference on Plasma Physics*, Virtual, SM022, 2021.
  - F. D. Cruz, D. B. Schaeffer, F. Cruz, and L. O. Silva. Particle-in-cell Simulations of Laser-driven, Ion-scale Magnetospheres in Laboratory Plasmas. *AGU Fall Meeting 2021*, New Orleans, USA, 2021.
  - F. D. Cruz, D. B. Schaeffer, F. Cruz, and L. O. Silva. Particle-in-cell simulations of laser-driven, ion-scale magnetospheres in laboratory plasmas. *13th International Conference on High Energy Density Laboratory Astrophysics*, Lisbon, Portugal, 2022.
- Talks:
  - F. D. Cruz, D. B. Schaeffer, F. Cruz, R. S. Dorst, P. V. Heuer, C. G. Constantin, P. Pribyl, C. Niemann, A. Bhattacharjee, and L. O. Silva. Simulações particle-in-cell de mini magnetosferas em plasmas de laboratórios acionados por laser. *FÍSICA 2020 – 22ª Conferência Nacional de Física e 30º Encontro Ibérico para o Ensino da Física*, Lisbon, Portugal, Física de Plasmas, 2020.
  - F. D. Cruz, D. B. Schaeffer, F. Cruz, and L. O. Silva. Particle-in-cell simulations of laser-driven, ion-scale magnetospheres in laboratory plasmas. *XXXI Encontro Nacional de Astronomia e Astrofísica*, Virtual, Solar & Stellar Physics, 2021.
  - F. D. Cruz, D. B. Schaeffer, F. Cruz, and L. O. Silva. Particle-in-cell simulations of laser-driven, ion-scale magnetospheres in laboratory plasmas. *63rd Annual Meeting of the APS Division of Plasma Physics*, Pittsburgh, USA, JO06, 2021.

  - F. D. Cruz, D. B. Schaeffer, F. Cruz, and L. O. Silva. Particle-in-cell simulations of laser-driven, ion-scale magnetospheres in laboratory plasmas. *48th EPS Conference on Plasma Physics*, Virtual, Basic, Space and Astrophysical Plasmas, 2022 (future meeting).

- Papers:

  - D. B. Schaeffer, F. D. Cruz, R. S. Dorst, F. Cruz, P. V. Heuer, C. G. Constantin, P. Pribyl, C. Niemann, L. O. Silva, and A. Bhattacharjee. Laser-driven, ion-scale magnetospheres in laboratory plasmas. I. Experimental platform and first results. *Physics of Plasmas*, 29(4):042901, 2022 (selected as Featured paper, with press release).
  - F. D. Cruz, D. B. Schaeffer, F. Cruz, and L. O. Silva. Laser-driven, ion-scale magnetospheres in laboratory plasmas. II. Particle-in-cell simulations. *Physics of Plasmas*, 29(3):032902, 2022 (selected as Editor's Pick).
  - F. D. Cruz, D. B. Schaeffer, F. Cruz, and L. O. Silva. Coupling between a uniform driven plasma and a magnetized plasma (in preparation).

Chapter 2

Coupling between a fast-driven plasma and a magnetized plasma

In the LAPD experiments described in Section 1.2.2, a mini magnetosphere was produced in a laboratory setting by driving an unmagnetized driver plasma against a dipole embedded in a uniform magnetized background plasma. In this setup, the driver plasma interacts first with the background plasma before suffering significant effects from the magnetic field of the dipole. This early interaction is highly dependent on the coupling between the two plasmas, *i.e.*, the efficiency of energy and momentum transfer from one plasma to the other.

In the early stages, the driver transfers energy and momentum to the background. Due to the large mass discrepancies between the ions and electrons, the driver electrons near the driver-background interface are highly magnetized while the driver ions are effectively unmagnetized. This resulting space charge separation creates the electric field $\mathbf{E}$ near the boundary between the plasmas that deflects the driver ions and provides an $\mathbf{E} \times \mathbf{B}$ drift for the driver electrons. The electrons generate a diamagnetic current that produces an opposing magnetic field to the background magnetic field, forming a magnetic cavity of null magnetic field. With this process, the background moves with the driver plasma. The electron scales are important during this process, and therefore, numerical studies need to resolve the electron scales of the system.

It is the result of the coupling that determines the properties of the plasmas that interact with the dipole and ultimately determines the formation of a mini magnetosphere and the subsequent dynamics. Determining how and by how much the background plasma is compressed may help us understand experiments where we only have limited data, e.g. the magnetic field compression. To fully study the dynamics of mini magnetospheres, we need to understand the interaction of the driver plasma with a uniform magnetized background plasma.

In this Chapter, we study the coupling between a fast unmagnetized driver plasma flow with a magnetized background plasma. Using energy and momentum conservation arguments over averaged quantities, we obtain analytical expressions for multiple parameters of the system, which are consistent with the results of multiple 1D PIC simulations. The results allow us to describe the evolution of the plasmas

from initial conditions.

2.1 PIC simulations and coupling parameters

2.1.1 Setup of the simulations

To study the coupling between the plasmas, we performed multiple 1D simulations with OSIRIS, a massively parallel and fully relativistic PIC code [61, 62]. The simulations consider an unmagnetized plasma flowing against a magnetized background plasma for a wide range of parameters. With PIC simulations, we can accurately resolve the plasma kinetic scales of these systems. These simulations allow us to comprehend how the two plasmas interact with each other and, from it, assume plasma models that help us deduce analytical expressions to describe the dynamics of the interaction.

The 1D simulations consist of a 25 d_i length region with open boundary conditions at $x = -5\ d_i$ and $x = 20\ d_i$, where $d_i = c/\omega_{pi} = \sqrt{m_{i,0}c/4\pi n_0 e^2}$ is the ion skin depth of the background plasma, with c the speed of light in vacuum, ω_{pi} the ion plasma frequency, e the electron charge, and $m_{i,0}$ and n_0 the ion mass and the density of the background plasma, respectively. Note that this length is much larger than any scale of the LAPD experiments since here, we are interested in studying the quasi-stationary regime of the system for a sufficient amount of time. Since the most relevant dynamics of the simulations occur at the ion kinetic scales, the spatial scales were normalized to d_i and the time scales to the ion cyclotron frequency of the background plasma $\omega_{ci}^{-1} = m_{i,0}c/eB_0$, where B_0 is the background magnetic field. The simulations consider 200 particles per cell per species. To resolve the dynamics of the electron kinetic scales, we used 10 grid cells per electron skin depth, $d_e = d_i\sqrt{m_e/m_{i,0}}$.

We consider an idealized and simplified driver plasma in the simulations when compared to the laser-produced plasma in the experiments. The driver flows toward the positive x direction with fluid velocity $\mathbf{v_0} = v_0\ \hat{\mathbf{x}}$, has a uniform density n_d, and a length of L_x, that is typically 5 d_i. The driver is initially located between $x = -5\ d_i$ and $x = 0$, and it is composed of a single species of ions with mass $m_{i,d}$ and electrons. Equivalently, the background plasma has a density of n_0 and a length of 20 d_i. It is located between $x = 0$ and $x = 20\ d_i$, and it is also composed of a species of ions with mass $m_{i,0}$ and electrons. Unlike the driver, the background plasma is magnetized by an internal and uniform magnetic field $\mathbf{B_0} = B_0\ \hat{\mathbf{z}}$. The magnitude of B_0 is calculated from the Alfvénic Mach number, defined as $M_A \equiv v_0/v_A = v_0\sqrt{4\pi n_0 m_{i,0}}/B_0$, where v_A is the Alfvén velocity. For both plasmas, all the ions have charge $q_i = e$, and the electrons have mass m_e.

The simulations consider cold plasmas, reduced ion mass ratios $m_{i,0}/m_e = 100$, and faster fluid velocities $v_0 = 0.1\ c$ than expected in experiments and most astrophysical scenarios. These approximations reduce the computational resources necessary to perform the simulations, allow extended scans over different parameters, and simplify our analysis. The chosen ion-to-electron mass ratio in the simulations is high enough to ensure sufficient separation between electron and ion spatial and temporal scales. In these systems, the thermal effects are typically negligible and do not affect the main results. We considered electron thermal velocities $v_{the} = 0.1\ v_0$, with $v_{the,x} = v_{the,y} = v_{the,z} = v_{the}/\sqrt{3}$, for both the driver and background plasmas, and that the ions and electrons are initially in thermal equilibrium.

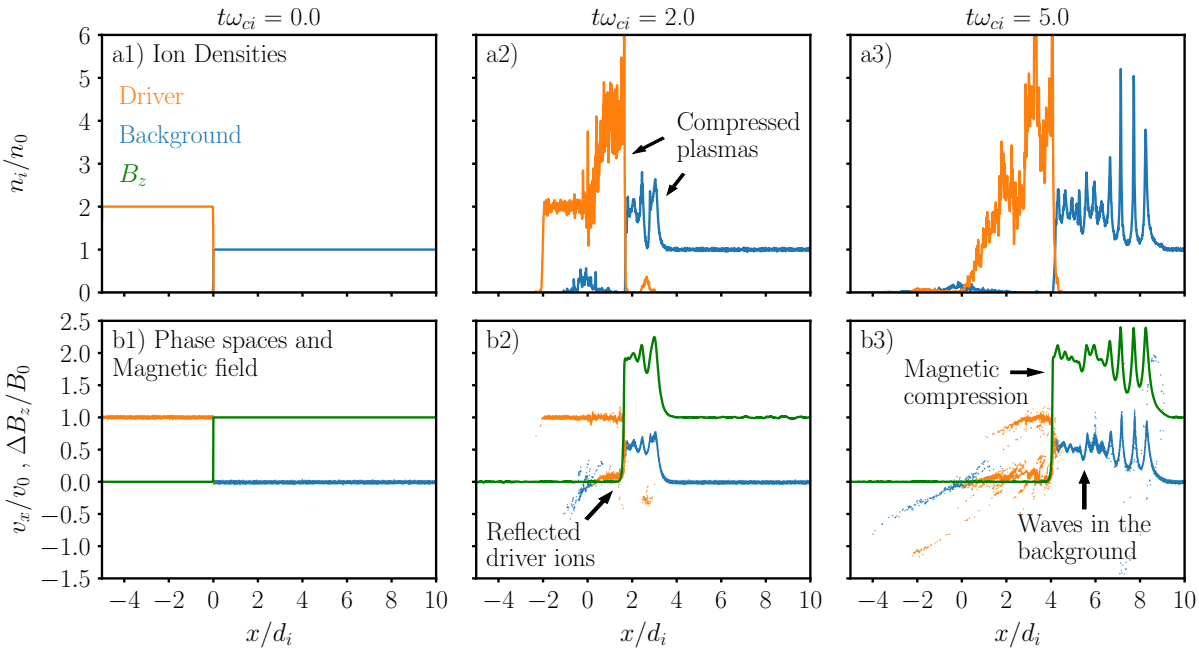

Figure 2.1: a) Ion densities n_i and b) x component of the ion velocities v_x, for the driver (orange) and background (blue) plasmas. The green line shows the magnetic field B_z. Columns 1–3 correspond to three different time steps. The simulation considers $n_d/n_0 = 2$, $m_{i,d}/m_{i,0} = 1$, and $M_A = 1.5$.

Additionally, n_0 is the independent variable of OSIRIS. We ensure that v_0 is low enough to neglect relativistic effects on the system. By using proper space and time scales (d_i, ω_{ci}^{-1}), we expect the system to be v_0 independent if we define the system by the main dimensionless physical parameters (M_A, n_d/n_0 and $m_{i,d}/m_{i,0}$). Therefore, the simplifications considered in the simulations should not affect the main results.

In this Chapter, we show the results of multiple parameter scans from these simulations. During the parameter scans, we keep the background parameters n_0 and $m_{i,0}$ unchanged, and instead change the driver parameters n_d and $m_{i,d}$, and the Mach number M_A. The simulation scans consider driver densities such that $0.2 \leq n_d/n_0 \leq 10$, ion masses for the driver such that $1 \leq m_{i,d}/m_{i,0} \leq 9$ and low Alfvénic Mach numbers such that $0.5 \leq M_A \leq 1.5$.

2.1.2 Basic system dynamics

Figure 2.1 illustrates the basic temporal evolution of the system, and shows the ion densities n_i of the driver and background plasmas, the ion phase spaces, and the magnetic field B_z, for three different time steps. The initial setup of the simulations is represented in Figures 2.1 a1) and b1). The simulation represented considers $n_d/n_0 = 2$, $m_{i,d}/m_{i,0} = 1$, and $M_A = 1.5$.

For the parameters chosen, we observe a strong coupling between the driver and magnetized background plasmas [32]. As the driver flows to the right, it pushes the background plasma and the magnetic field with it, leading to a relocation of the interface between the two plasmas and creating two high-density regions on both sides of the interface, as we can see in Figures 2.1 a2) and a3). During this process, the driver plasma is mostly confined in the upstream region, relative to the plasma flow, while the background plasma is mostly confined downstream.

In the transition between the unmagnetized driver and the magnetized background regions, there is a sudden jump in the magnetic field profile. The existence of a gradient in B_z leads to the presence of an electric field in the x direction. This electric field is discussed in Section 2.3.2. As the driver particles flow with velocity v_0 against the background, they interact with this electric field and end up reflected upstream with a new velocity $v_1 < v_0$, as we observe in Figures 2.1 b1) to b3). This reflection leads to the increase of the driver and background densities observed in Figures 2.1 a2) to a3). As this happens, the bulk of the driver travels to the right through the region initially occupied by the background plasma and, due to the diamagnetic property of the plasmas created by the $\mathbf{E} \times \mathbf{B}$ drift of the electrons, it also expels the magnetic field, creating a magnetic cavity with null magnetic field in the region of the driver.

The energy and momentum lost by the driver plasma during this process are transferred to the background, resulting in a perturbation of the system characteristics. The initially stationary background ions are accelerated, and the magnetic field in the background is compressed. During this process, multiple waves and instabilities form in the background region, leading to the oscillations observed in Figure 2.1. We also see in Figure 2.1 that the size of the perturbed background region also increases over time.

Figure 2.1 also shows that the magnetic field and the plasma densities of the system are not constant. However, some averaged quantities of the system do not change significantly over time. The average velocity of the accelerated background ions and the average of the compressed magnetic field are such examples. We can, therefore, consider that the system achieves a quasi-stationary regime that can be represented by its average properties. In Section 2.5, we show that these properties depend on the initial parameters of the system, can be predicted by analytical expressions, and can be used to describe the coupling of the plasmas.

2.1.3 Magnetic and current density diagnostics and coupling parameters

To comprehend the dynamics of these systems, it is important to investigate the evolution of B_z since it describes the motion of the particles and the electric fields. Additionally, from Ampère's law, the y component of the current density is given by $J_y \approx -(c/4\pi) \cdot \partial B_z/\partial x$, and so we can use J_y to investigate the changes in the magnetic field.

To illustrate these two important quantities, we show in Figure 2.2 the temporal evolution of a) the variation of the magnetic $\Delta B_z = B_z - B_{z,\text{ini}}$, where $B_{z,\text{ini}}$ is the initial magnetic field, and b) the current density J_y. These are similar diagnostics to the ones shown in Figure 1.4 and can be replicated in experiments. To understand how the system depends on the initial parameters, these diagnostics are shown for three driver densities: 1) $n_d/n_0 = 0.5$, 2) $n_d/n_0 = 2$, and 3) $n_d/n_0 = 5$, with $M_A = 1.5$ and $m_{i,d}/m_{i,0} = 1$.

We observe the same main structures for the three driver densities in Figure 2.2. As discussed in Section 2.1.2, while the driver flows against the background, it expels the magnetic field, creating a magnetic cavity with null magnetic field, as observed in Figures 2.2 a1) to a3). This magnetic cavity expands over time, and its maximum distance increases with the driver density. This is expected since the coupling between the driver and background plasmas improves for denser drivers [41], and the

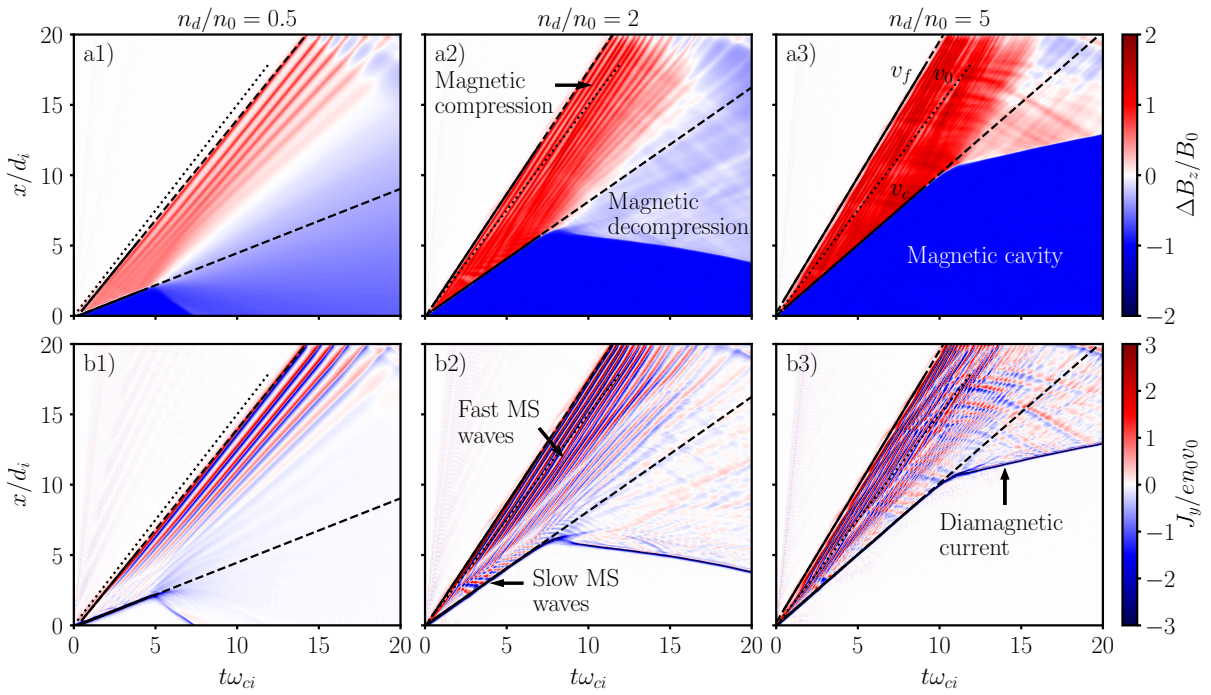

Figure 2.2: Temporal evolution of a) the variation of the magnetic field B_z and b) the current density J_y for three different simulations with 1) $n_d/n_0 = 0.5$, 2) $n_d/n_0 = 2$, and 3) $n_d/n_0 = 5$, with $M_A = 1.5$ and $m_{i,d}/m_{i,0} = 1$. The dotted line has a slope equal to v_0, and the solid and dashed line have slopes equal to the coupling velocity v_c and the front velocity v_f. Frames a2) and b2) correspond to the simulation shown in Figure 2.1. In all frames, we observe the Magnetosonic (MS) waves in the background.

energy and pressure exerted by the driver increases with the driver density. Therefore, for high driver densities, the driver has the capacity to expel more energy from the background region, leading to larger magnetic cavities. The velocity at which the magnetic cavity travels through the background is designated by **coupling velocity**, or cavity velocity, and represented by v_c. This velocity is always lower than v_0 and, as visible in Figure 2.2, it increases with the driver density.

As observed in Figures 2.1 b1) to b3), the driver ions flow with velocity v_0 against the background region and get reflected by the electric field at the interface between the plasmas. As a result, the number of driver ions traveling with velocity v_0 shrinks over time, while the number of ions that end up with the reflected velocity v_1 increases. If the driver does not have enough energy to push the background plasma any further, after all the driver ions end up reflected, then the magnetic cavity will be reflected as well. This occurs for the $n_d/n_0 = 0.5$ and $n_d/n_0 = 2$ cases (at $t\omega_{ci} \approx 5$ and $t\omega_{ci} \approx 8$, respectively). For the $n_d/n_0 = 5$ case, after all the ions with velocity v_0 get slowed down ($t\omega_{ci} \approx 10$), the reflected ions with velocity v_1 still have enough energy to push the background, although at a lower velocity. We consider the **stopping distance** L_{stop} as the distance that the driver ions with velocity v_0 are able to push the magnetic cavity through the background region before being totally reflected.

In Figures 2.2 a1) to a3), we also observe the magnetic compression in the downstream region, where the background is located. While the compressed magnetic field is not constant, its average does not change significantly over time (during the main interaction of the plasmas). The average ratio of compressed to initial magnetic field is designated by **compression ratio**, and it is represented by α. Additionally, the background region of the compressed magnetic field increases over time. The velocity

at which the magnetic compression travels through the unperturbed background plasma is designated by **front velocity**, or compression velocity, and it is represented by v_f. Figure 2.2 shows that v_f also increases with the driver density. After the driver's reflection, some of the compressed plasma continues to move through the unperturbed background.

Figures 2.2 b1) to b3) show the current densities for the three driver densities $n_d/n_0 = 0.5$, 2 and 5. The jump in the magnetic field from the magnetic cavity to the magnetized plasma is described by the diamagnetic current. In the background region, we also observe multiple current structures associated with the waves that form in the background plasmas.

For a homogeneous magnetized plasma, the MHD formalism predicts three characteristic electromagnetic plasma waves: the fast, the slow, and the intermediate modes. The intermediate mode is the traditional Alfvén wave which has a phase velocity of $v_\phi = \omega/\kappa = v_A \cos\theta$, where ω, κ, v_A, and θ are the frequency, wave number, Alfvén velocity, and angle between the magnetic field and the wavenumber, respectively. The other two modes are the branches of the magnetosonic (MS) waves with phase velocities given by

$$v_\phi = \frac{\omega}{\kappa} = \left\{ \frac{1}{2} \left[v_A^2 + c_s^2 \pm \sqrt{(v_A^2 + c_s^2)^2 - 4 v_A^2 c_s^2 \cos^2\theta} \right] \right\}^{\frac{1}{2}} , \tag{2.1}$$

where c_s is the sound speed. Because the magnetic field in these systems is perpendicular to the wave propagation ($\theta = \pi/2$), and because we considered cold plasmas in our simulations, the Alfvén wave cannot form, and $v_A \gg c_s$. Therefore, only the slow and fast magnetosonic waves can develop in these simulations, with $\omega/\kappa \approx 0$ and $\omega/\kappa \approx v_A$, respectively. Both these waves can be seen in Figure 2.2. The phase velocities of these waves in the simulations are close to the expected values.

It is simple to measure the quantities v_c, v_f, α, and $L_{\rm stop}$, that describe the coupling between the plasmas, by only using the magnetic diagnostics shown in Figure 2.2. If we derive analytical expressions for these quantities, then we can estimate the necessary parameters of the system that ensure good/weak coupling, and use that information for future experiments. It is worth noting, however, that although these three quantities tend to remain constant over the main interaction between the plasmas, the same does not always occur in experiments with similar configurations [34, 63]. In the experiments, it is not always possible to create sufficiently large uniform plasmas, and we need to consider 3D effects. However, as we observed in Figure 1.4 a), some experiments still show similar results to Figure 2.2.

2.2 Laminar electric field

To analytically model the simulations, we first look at the electric field that arises in these systems. For the collisionless, magnetic pressure dominated ($\beta_e \equiv 8\pi n_e T_e/B^2 \ll 1$, where n_e and T_e are the electron density and temperature), and low Mach number ($M_A \sim 1$) scenarios considered, neither Coulomb collisions nor instabilities effectively transfer momentum and energy between the driver plasma and the perpendicularly magnetized background plasma. Consequently, for these conditions, the laminar electric field provides the dominant coupling mechanism between the two plasmas [34]. Using a hybrid model [29], where the ion species are considered kinetically, and the electron species as a charge

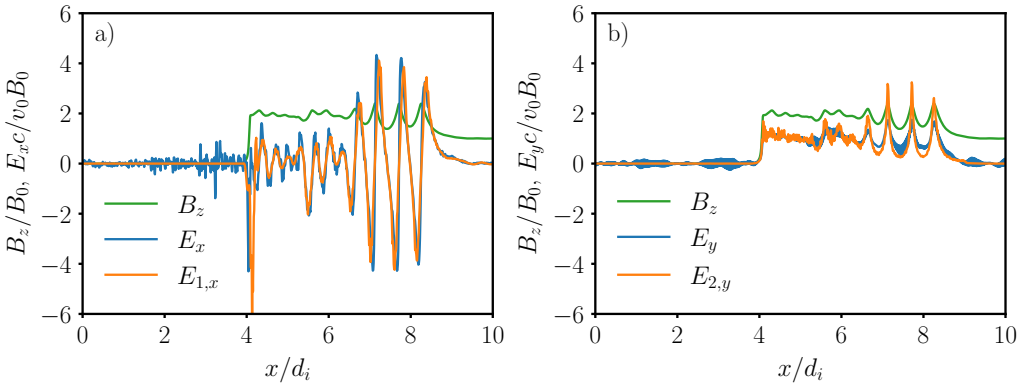

Figure 2.3: Comparison between the main terms of Equation (2.2) and the electric field of the simulation presented in Figure 2.1, for $t\omega_{ci} \approx 5.0$. The x components of the electric field are shown in a) and the y components in b). E_x and E_y refer to the electric field profiles of the simulation (blue), and E_1 and E_2 to the first and second terms of Equation (2.2) (orange). Both frames also show the magnetic field B_z (green).

neutralizing fluid, and considering that the magnetic field is mostly defined in the z direction, then the laminar collisionless electric field of the system, for the regimes discussed, is approximately given by

$$\mathbf{E} \approx -\frac{1}{4\pi e n_e} B_z \nabla_\perp B_z - \frac{1}{e n_e c}(\mathbf{J_0} + \mathbf{J_d}) \times \mathbf{B_z} - \frac{\nabla p_e}{e n_e} \,. \tag{2.2}$$

In Equation (2.2), n_e is the electron density and $\mathbf{J_j} = Z_j n_j \mathbf{v_j}$ the current density of the driver ($j = d$) or of the background ($j = 0$) plasmas. Z_j, n_j and $\mathbf{v_j}$ are the ions charge, density, and velocity, respectively, for the plasma j. Here, $p_e = n_e m_e v_{the}^2$ is the electron pressure. With quasi-neutrality, we have $n_e \approx Z_0 n_0 + Z_d n_d$.

The electric field in Equation (2.2) is composed of three different terms. The first term $\mathbf{E_1} = -B_z \nabla_\perp B_z / 4\pi e n_e$ depends on the gradient of the magnetic field and is more relevant in the regions where B_z changes rapidly, namely, the interfaces between the magnetic cavity and the magnetic compression, and the magnetic compression and the unperturbed plasma. Since turbulence can be neglected, we have $|\partial B/\partial y| \ll |\partial B/\partial x|$, and so $\mathbf{E_1}$ is primarily defined along the x direction.

The second term in Equation (2.2), $\mathbf{E_2} = -(\mathbf{J_b} + \mathbf{J_d}) \times \mathbf{B_z}/e n_e c$, is dependent on the ion currents of the system. Since the ion motions are mostly defined in the x direction, this term is mostly defined in the y direction, and it is approximately given by $\mathbf{E_2} \approx (v_x/c) B_z \, \mathbf{y}$. As a result, this term opposes the Lorentz force term $\mathbf{v} \times \mathbf{B}$ that attempts to gyrate the particles, and the background ions gain flow velocity after interacting with the driver plasma.

Finally, the third term of Equation (2.2), $\mathbf{E_3} = -\nabla p_e / e n_e$, is mostly defined in the x direction. The ratio $|\mathbf{E_3}|/|\mathbf{E_1}|$ scales with β_e. Since we consider cold plasmas in the simulations, this last term can be neglected when compared to the other two terms of Equation (2.2).

To verify if Equation (2.2) correctly describes the electric field of the system, the main terms in Equation (2.2) and the electric field of the simulation previously presented in Figure 2.1 and Figures 2.2 a2) and b2), are compared in Figure 2.3, for $t\omega_{ci} \approx 5.0$.

Figure 2.3 shows that we can use Equation (2.2) to calculate the electric field in these systems. In Figure 2.3 a), we see that the x component of the electric field of the simulations can be predicted from

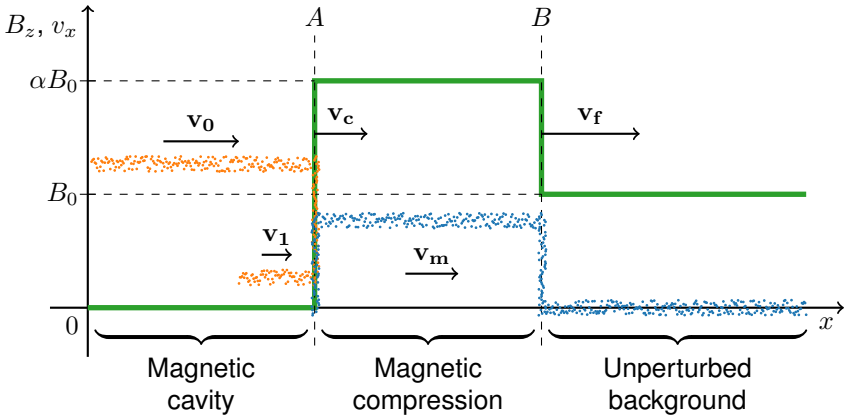

Figure 2.4: Simplified model that describes the main interaction between the driver plasma (orange) with the background plasma (blue) and the magnetic field (green). The dots illustrate the ion particles. This model considers three different regions: the magnetic cavity, the magnetic compression, and the unperturbed background, with two discontinuities, labeled by A and B, where the system properties change suddenly.

the first term of Equation (2.2), which depends on the magnetic field gradient, as we initially expected. Within the interface that separates the magnetic cavity from the compressed magnetic field, we see that there is a significant negative electric field. This electric field is responsible for the reflection of the driver ions back to the upstream region.

Figure 2.3 b) also shows that the y component of the electric field can be described by the second term of Equation (2.2). In the background region, E_y is always positive and is approximately $+v_x B_z$. Although not represented in Figure 2.3, the third term of Equation (2.2) was also calculated, and we confirmed that it is not relevant to describe the electric field in these simulations.

After confirming that Equation (2.2) can be used to calculate the electric field of these systems, we can use it to derive a relation between the different coupling parameters v_c, v_f, and α, as we will see in Section 2.3.2.

2.3 Physics at the boundaries

2.3.1 Simplified model for the system

As discussed in Section 2.1, as the driver pushes the background, and if the two plasmas are long enough, the system reaches a quasi-stationary regime, where some parameters of the system do not change significantly over time. Under this regime, we can consider a few assumptions. With average quantities and the MHD formalism, the system can be separated into different regions with similar properties and described by the model shown in Figure 2.4. We neglect thermal effects, wave formation, instabilities, electron pressure effects, and particle trapping. These simplifications should not affect our description of the coupling for the low Mach number ($M_A \sim 1$), cold plasmas, and uniform density profiles considered in this Chapter.

The model considers three regions characterized by different magnetic and kinetic properties. The first one refers to the magnetic cavity, where $B_z \approx 0$. The driver plasma is located in this upstream region, and the ion motion of the driver can be described by two ion flows with velocity $\mathbf{v_0}$ and $\mathbf{v_1}$. The second

region refers to the magnetic compression, where the average magnetic field is αB_0. In this region, the background ions accelerated by the interaction with the driver plasma have an average velocity of $\mathbf{v_m}$. The third region refers to the background region that remains unperturbed by the interaction of the two plasmas. Here, the magnetic field is B_0 and the background ions have no flow velocity. These three regions are present in Figure 2.2.

These regions are separated by two discontinuities labeled A and B, where the properties change abruptly. Discontinuities A and B move through the simulation box with velocity $\mathbf{v_c}$ and $\mathbf{v_f}$, respectively. From the upstream to the downstream side of the discontinuities, the mass, momentum, and energy flows must be conserved. By considering macroscopic properties, these conservation laws lead to the Rankine-Hugoniot (RH) jump conditions, which relate the parameters of each side of the discontinuities [64].

2.3.2 Electric field at the boundaries

We can also use the the electric field to study the physics at the boundaries. We now focus on the discontinuity A in Figure 2.4 and look at the reflection of the driver ions when facing the background magnetic field. Near this discontinuity, unmagnetized driver ions move with velocity v_0 against the compressed background magnetic field of average value αB_0. This discontinuity moves with velocity v_c, and the driver ions are eventually reflected upstream with velocity v_1.

In Section 2.2, we observed that a strong electric field in discontinuity A is responsible for the reflection of the driver ions. From Equation (2.2), this field is approximately given by

$$E_x \approx -\frac{1}{4\pi e n_e} B_z \left(\frac{\partial B_z}{\partial x}\right) \ . \tag{2.3}$$

For simplicity, we consider that the jump of the magnetic field across discontinuity A is linear and described by $B_z(x') \approx \alpha B_0(x'/\Delta)$, where Δ is the full width of this transition, and $x' \equiv x - x_A$ the position in the transition region, with $0 \leq x' < \Delta$, and x_A the initial position of discontinuity A, which varies in time. The equation of motion of a driver ion passing through boundary A, in the reference frame of this interface, and considering $E_x \gg v_y B_z$, is

$$m_{i,d}\frac{dv'_{i,d,x}}{dt'} = -\frac{1}{4\pi n_e}\left(\frac{\alpha B_0}{\Delta}\right)^2 x' \iff \frac{dv'_{i,d,x}}{dx'} v'_{i,d,x} = -\frac{1}{4\pi m_{i,d} n_e}\left(\frac{\alpha B_0}{\Delta}\right)^2 x' \ , \tag{2.4}$$

where $v'_{i,d,x} \equiv v_{i,d,x} - v_c$ is the driver ion velocity in the reference frame of the barrier. In this frame, the driver ions have initial velocity $v'_{i,d,x} = v_0 - v_c$ and start to be reflected upstream when $v'_{i,d,x} = 0$. Integrating Equation (2.4), we get

$$\int_{v_0 - v_c}^{0} v'_{i,d,x}\, dv'_{i,d,x} = -\frac{1}{4\pi m_{i,d}}\left(\frac{\alpha B_0}{\Delta}\right)^2 \int_0^{\Delta} \frac{x'}{n_e}\, dx' \ . \tag{2.5}$$

After looking through the simulations performed in this Chapter, we consistently observed a peak in

the electron density of $n_e \approx 4\, n_d$. Assuming this value in Equation (2.5), we finally obtain

$$\frac{(v_0 - v_c)^2}{2} = \frac{1}{4\pi m_{i,d}} \left(\frac{\alpha B_0}{\Delta}\right)^2 \frac{\Delta^2}{8 n_d} \iff 2 n_d m_{i,d} (v_0 - v_c)^2 = \frac{(\alpha B_0)^2}{8\pi} \,. \tag{2.6}$$

Equation (2.6) represents a pressure balance in region A. If we consider that the mass flux of driver ions is conserved through discontinuity A, *i.e.*, all the driver ions that reach this interface are reflected upstream, and there are no ions that leak to the background or pile up in this region, then $n_d(v_0 - v_c) = n'_d(v_c - v_1)$, where n'_d is the density of the reflected driver ions. From symmetry arguments, we must also have $v_0 - v_c = v_c - v_1$, and therefore, $n'_d = n_d$. At the reference frame of the discontinuity, the magnetic pressure in the downstream region, $B_z^2/8\pi = (\alpha B_0)^2/8\pi$, balances the pressure exerted by the driver plasma in the upstream region, $n_i m_i v_{i,x}^2 = 2 n_d m_{i,d} (v_0 - v_c)^2$, where a factor of 2 in the density was added to consider both the ions with v_0 and v_1 velocities, leading to the pressure equilibrium in Equation (2.6).

Equation (2.6) shows a relation between the coupling parameters v_c and α and the initial parameters of the system. Besides the electric field that acts on the particles, we can look at the conservation laws that rise from the MHD and Maxwell's equations to study the physics of the discontinuities. These conservation laws are expressed in the Rankine-Hugoniot jump conditions.

2.3.3 Rankine-Hugoniot jump conditions

To relate the parameters of each region represented in Figure 2.4, we first look at the conservation laws for the simple scenario where only one discontinuity exists. We define regions 1 and 2 as the upstream and downstream sides of this discontinuity, respectively, and that each region is described by a different set of parameters. We also assume that the normal to the discontinuity is aligned along the x direction and that the discontinuity is infinite in the y and z directions.

By integrating the MHD and Maxwell's equations over the discontinuity, we can relate the plasma quantities in regions 1 and 2. In the reference frame of the discontinuity, we can drop the time derivatives, and the problem reduces to determining the solution of a stationary system [8, 64]. In this reference frame, the MHD and Maxwell's equations result in the following relations

$$\nabla \cdot (n\mathbf{v}) = 0 \tag{2.7}$$

$$\nabla \cdot (nm\mathbf{v}\mathbf{v}) + \nabla \left(p + \frac{B^2}{8\pi}\right) - \frac{1}{4\pi} \nabla \cdot (\mathbf{B}\mathbf{B}) = 0 \tag{2.8}$$

$$\nabla \cdot \left[nm\mathbf{v}\left(\frac{1}{2}v^2 + \omega\right) + \mathbf{v}\left(p + \frac{B^2}{4\pi}\right) - \frac{\mathbf{B}}{4\pi}(\mathbf{v}\cdot\mathbf{B})\right] = 0 \tag{2.9}$$

$$\nabla \times (\mathbf{v} \times B) = 0 \,. \tag{2.10}$$

In these expressions, n, m, and $\mathbf{v}$ are the average density, mass, and velocity of the plasma, respectively, $\mathbf{B}$ the magnetic field, p the plasma pressure, and $\omega = p/(\gamma - 1)nm$ the plasma enthalpy, with γ the adiabatic index.

For a generic scalar quantity X, the integration of its gradient is equal to

$$\int_1^2 \frac{dX}{dx}\, dx = \int_1^2 dX = X_2 - X_1 \equiv [X]\ . \tag{2.11}$$

For a generic vector $\mathbf{X} = (X_x, X_y, X_z)$, the integrations of its divergence and curl are

$$\int_1^2 \nabla \cdot \mathbf{X}\, dx = \int_1^2 \frac{\partial X_x}{\partial x}\, dx = [X_x] \tag{2.12}$$

$$\int_1^2 \nabla \times \mathbf{X}\, dx = \int_1^2 \left(\frac{\partial X_y}{\partial x}\mathbf{z} - \frac{\partial X_z}{\partial x}\mathbf{y}\right)\, dx = [X_y]\mathbf{z} - [X_z]\mathbf{y}\ . \tag{2.13}$$

For the configurations considered in this work, $\mathbf{B}$ is mostly defined in the z direction and $\mathbf{v}$ in the x direction. If we consider cold plasmas and neglect thermal effects, we have $\omega = 0$ and $p = 0$, and we can simplify the relations further. Integrating Equations (2.7) to (2.10) with Equations (2.11) to (2.13) leads to

$$[nv_x] = 0 \tag{2.14}$$

$$\left[nmv_x^2 + \frac{B_z^2}{8\pi}\right] = 0 \tag{2.15}$$

$$\left[\frac{1}{2}nmv_x^3 + \frac{B^2 v_x}{4\pi}\right] = 0 \tag{2.16}$$

$$[v_x B_z] = 0\ . \tag{2.17}$$

Equations (2.14) to (2.17) are known as the Rankine-Hugoniot (RH) jump conditions and set the relations between the upstream and downstream parameters around a discontinuity. We can use these equations to determine analytical expressions for the coupling parameters. However, some caution must be taken since these equations are deduced for a single boundary, while two boundaries form in the simulations, as represented in Figure 2.4.

2.3.4 Applying the RH equations to the discontinuities

As mentioned in Section 2.3.2, the mass flow of the driver ions must be conserved during the evolution of the system. This law corresponds to the RH Equation (2.14). Applying this Equation to boundary A leads to

$$n_d(v_0 - v_c) + n'_d(v_1 - v_c) = 0\ . \tag{2.18}$$

As previously discussed, due to symmetry arguments, $v_c = (v_0 + v_1)/2$, and as a result, $n_d = n'_d$. From Equation (2.17), and assuming the model of Figure 2.4, we also have for the boundary A

$$(v_m - v_c)\alpha B_0 = 0 \iff v_m = v_c\ , \tag{2.19}$$

as expected. Using these two conservation laws for boundary B, we obtain

$$(v_m - v_f)\alpha B_0 = -v_f B_0 \iff \alpha = \frac{v_f}{v_f - v_c} \tag{2.20}$$

$$(v_m - v_f)n_0' = -v_f n_0 \iff \frac{n_0'}{n_0} = \frac{v_f}{v_f - v_c}\ . \tag{2.21}$$

Equation (2.20) shows a relation between α, v_c, and v_f. As we observed in Figure 2.1, the background plasma gets compressed, and its density increases from n_0 to n_0' in the magnetic compression region. Equation (2.21) shows that the background density increases by the same ratio as the magnetic field, *i.e.*, by a factor of α.

Finally, we look at the conservation of momentum by applying Equation (2.15) to discontinuity A

$$n_d m_{i,d}(v_0 - v_c)^2 + n_d' m_{i,d}(v_1 - v_c)^2 = \frac{(\alpha B_0)^2}{8\pi} + \alpha n_0 m_{i,0}(v_m - v_c)^2 \Leftrightarrow 2n_d m_{i,d}(v_0 - v_c)^2 = \frac{(\alpha B_0)^2}{8\pi}\ . \tag{2.22}$$

Equation (2.15) leads to the same result as Equation (2.6), calculated from the electric field. We now have two different equations, Equations (2.20) and (2.22), that relate the coupling parameters v_c, v_f, and α. A third equation will allow for the derivation of analytical expressions for these quantities. This last equation can be obtained from the conservation of energy.

As previously mentioned, we must be careful when applying these RH equations, derived for a single discontinuity, to systems with two discontinuities moving at different velocities. We cannot use Equation (2.16) as it does not consider the energy flows shared by boundaries A and B. However, we can solve this issue by deriving the different energy variation terms that describe these systems and correcting the energy conservation law.

2.4 Energy conservation of the system

In Section 2.3, we derived Equations (2.20) and (2.22) by looking at the physics at boundaries of the plasmas. If we now consider these equations and the energy conservation law, we can obtain analytical expressions for the coupling parameters v_c, v_f, and α.

Considering ΔE_{dr}, ΔE_0, ΔE_{mag}, and ΔE_{ele} as the energy variations of the system associated with the driver plasma, the background plasma, the magnetic field, and the electric field, respectively, over a time Δt, we must have

$$\Delta E_{\text{d}} + \Delta E_0 + \Delta E_{\text{mag}} + \Delta E_{\text{ele}} = 0\ . \tag{2.23}$$

Figure 2.3 showed that the electric field of the system is of the same order as $v_0 B_0$. This means that the energy term ΔE_{ele} can be neglected when compared to the magnetic energy ΔE_{mag} since $E_{\text{ele}}^2 / E_{\text{mag}}^2 \sim (v_0/c)^2 \ll 1$. To determine the coupling parameters, we need to find the energy terms in Equation (2.23) as a function of v_c, v_f, α, and the initial parameters of the system.

To derive the expressions for these energy terms, we will assume the model in Figure 2.4, which considers a quasi-stationary regime of a system described by averaged magnetic and kinetic parameters without thermal effects or instabilities.

2.4.1 Driver plasma energy variation

Because we are neglecting thermal effects and $m_e \ll m_i$, most of the driver's energy is transferred by the ions instead of the electrons. As discussed in Section 2.3, the mass flux of the driver ions must be constant through the reflection process, and so $n'_d = n_d$ and $v_1 = 2v_c - v_0$.

With these assumptions, the the energy of the driver lost during the interaction between the plasmas, ΔE_{d}, can be calculated by the energy gained by the ion population traveling with velocity v_1 plus the energy lost by the ion population with velocity v_0. The energy variation of each population can be calculated by multiplying the kinetic energy of each ion with the variation of the number of ions within the population. Recalling that the interface between the driver and the background plasmas travels with velocity v_c, then for an area transverse to the plasma flow A_T, and for a time Δt, the energy variation of the driver plasma is given by

$$\Delta E_{\mathsf{d}} = -\frac{1}{2} m_{i,d} v_0^2 n_d (v_0 - v_c) A_T \Delta t + \frac{1}{2} m_{i,d} v_1^2 n'_d (v_c - v_1) A_T \Delta t = -2 n_d m_{i,d} (v_0 - v_c)^2 v_c A_T \Delta t \ . \quad (2.24)$$

With Equation (2.24), we can represent the driver's energy with the initial parameters and v_c.

2.4.2 Background plasma energy variation

In Figure 2.4, the background plasma is located in two different regions. Since the plasma is stationary in the unperturbed background region, the background plasma energy variation ΔE_0 is equal to the increase of energy of the compressed background region.

From Equation (2.19), we saw that $v_m{=}v_c$. The average energy of each background ion is thus $m_{i,0} v_c^2/2$. The density of the compressed background n'_0, in the region of the magnetic compression, can be calculated with Equation (2.21). We also see in Figure 2.4 that the back and front boundaries of the magnetic compression region travel with velocities v_c and v_f, respectively, and thus the length of this region increases at a velocity equal to $v_f - v_c$. The variation of background plasma energy is then described by

$$\Delta E_0 = \frac{1}{2} m_{i,0} v_c^2 n'_0 (v_f - v_c) A_T \Delta t = \frac{1}{2} m_{i,0} v_c^2 n_0 v_f A_T \Delta t \ , \quad (2.25)$$

which depends on v_c, v_f, and the initial parameters of the system.

2.4.3 Magnetic energy variation

Finally, we need an expression for the variation of the magnetic energy ΔE_{mag} to apply Equation (2.23). As the driver pushes the background region, it expels the magnetic field initially located within the magnetic cavity region and compresses the magnetic field in the background. From Figure 2.4, we observe that this interaction leads to the magnetic compression region, with an average magnetic field equal to αB_0 and a length that increases at a velocity $v_f - v_c$, and the unperturbed background region, with a magnetic field B_0 and a length that changes at a velocity $-v_f$.

The magnetic energy variation is then described by

$$\Delta E_{\mathsf{mag}} = \frac{(\alpha B_0)^2}{8\pi} (v_f - v_c) A_T \Delta t - \frac{B_0^2}{8\pi} v_f A_T \Delta t = \frac{B_0^2}{8\pi} \left[\alpha^2 (v_f - v_c) - v_f\right] A_T \Delta t \ . \quad (2.26)$$

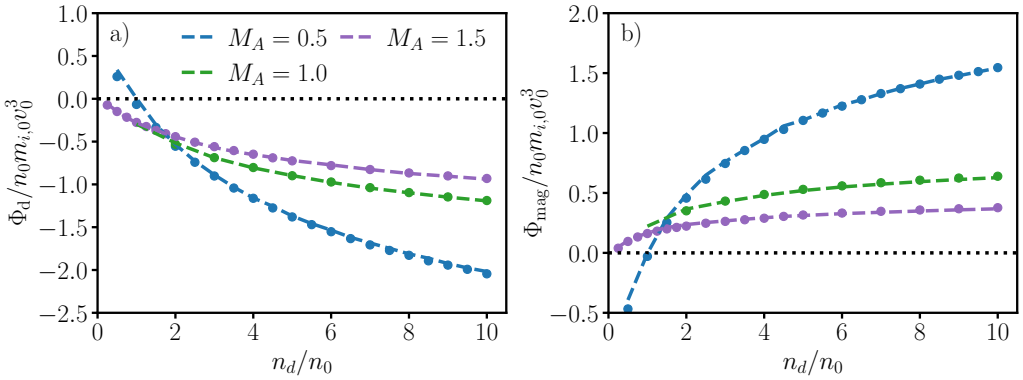

Figure 2.5: Energy flux of a) the driver ions Φ_d and b) the magnetic field Φ_{mag}, for multiple Mach numbers M_A and driver density ratios n_d/n_0. The energy fluxes calculated from the changes in the total energy are represented by scatter points, while the energy fluxes calculated from Equations (2.24) and (2.26), with the coupling parameters measured in each simulation, are connected by dashed lines.

With Equations (2.23) to (2.26), we can finally determine analytical expressions for the coupling parameters that only depend on the initial parameters of the system.

2.4.4 Validation of the energy expressions

Before deriving the analytical expressions for the coupling parameters, we first check the validity of the previous energy variation equations. To achieve this, we performed multiple simulations with a wide range of parameters and compared the energy diagnostics of the simulations with Equations (2.24) to (2.26).

As discussed in Section 2.1.3, we can use the magnetic field data to calculate the coupling parameters v_c, v_f, and α. For each time in the simulations, we detected sudden jumps in the magnetic field data and localized the boundaries A and B. By fitting a linear function to these positions, the coupling and front velocities were determined. These calculations only considered the main interaction between the plasmas, *i.e.*, times before the reflection of the magnetic cavity and the full reflection of the driver plasma. For α, we averaged the magnetic field between these two boundaries for the times considered.

For each simulation, the different kinetic and magnetic energy fluxes $\Phi_j \equiv \Delta E/A_T \Delta t$ were calculated from the variations of the total energies of the system (with $j = \mathrm{d}, 0$, and mag for the driver, background, and magnetic field, respectively). These fluxes were then compared to Equations (2.24) and (2.26), which used the measured coupling parameters of the simulations. Because we ensure that a quasi-stationary regime forms in each case, these fluxes remain constant during the main interaction of the system.

We performed simulations for three different Alfvénic Mach numbers M_A and multiple driver to background density ratios n_d/n_0. We considered $m_{i,d}/m_e = m_{i,0}/m_e = 100$. Figure 2.5 shows the energy fluxes of a) the driver ions Φ_d and b) the magnetic field Φ_{mag} for the simulations performed.

With Figure 2.5, we verify that Equations (2.24) and (2.26) can be used to describe the energy variations associated with the driver plasma and the background magnetic field for the parameters and time scales of interest to this work. In Figure 2.5 a) we see that, as expected, the flux of driver energy decreases with increasing driver density since the driver has larger initial energy. For higher Mach numbers, because the background is less magnetized, the driver is less efficient at transferring energy

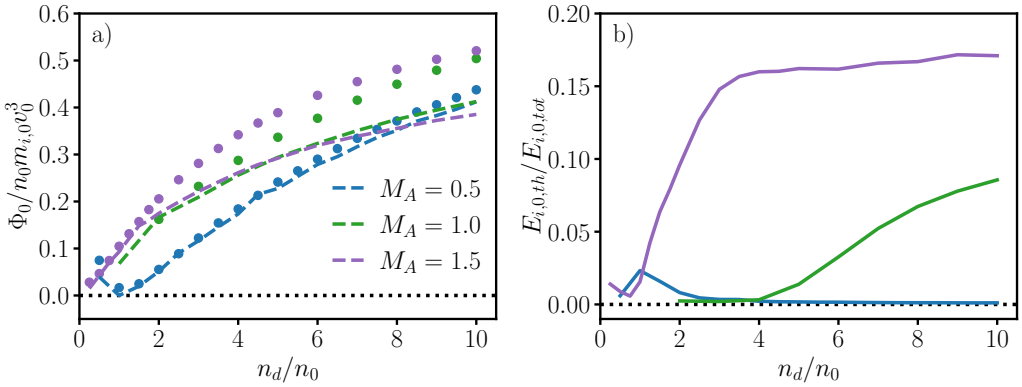

Figure 2.6: a) Energy flux of the background plasma Φ_0. The fluxes calculated from the changes in the total energy are represented by the scatter points, while the energy fluxes calculated from Equation (2.25), with the measured coupling parameters measured, are connected by the dashed lines. b) Fraction of thermal energy to total energy of the background ions, for each simulation, in the final stage of the main interaction.

to the background, and therefore, it loses energy at a lower rate. Similarly, in Figure 2.5 b), we observe that the magnetic energy flux is larger for denser drivers and lower Mach numbers. This means that, for lower Mach numbers, the background magnetic field will receive more energy than the background plasma.

In Figures 2.5 a) and b), we also observe in some simulations ($M_A = 0.5$ and $n_d/n_0 < 1$, for example) that the driver plasma gains energy while the magnetic field loses energy. These scenarios correspond to the cases where the initial magnetic pressure $B_0^2/8\pi$ is larger than the ram pressure of the driver plasma $2n_d m_{i,d} v_0^2$, so the driver is pushed back by the background, leading to negative coupling velocities. From Equation (2.22), we see that the background suffers a decompression instead of a compression, and it is the background magnetic field that transfers energy to the driver plasma.

Although the analytical expressions for the driver and magnetic energies are consistent with the simulations, as seen in Figure 2.5, the same is not verified for the background plasma energy. Figure 2.6 a) shows the energy flux of the background plasma Φ_0, and we can observe that, for the higher Mach numbers and higher driver densities, Equation (2.25) is not a good approximation to describe the energy changes of the background plasma. However, for low Mach numbers, Equation (2.25) seems to be a good description of the background ion energy.

For higher Mach numbers M_A and density ratios n_d/n_0, instabilities form in the background plasma and start to have an important role in the energy partition of the plasma. Since Equation (2.25) does not consider the thermal energy of the background plasma, these instabilities are not incorporated in the equations, so Equation (2.25) underestimates the variation of the background energy, as we observe in Figure 2.6 a). Figure 2.6 b) shows the average ratio of thermal energy of the background ions $E_{i,0,th}$ to the total energy of the background ions $E_{i,0,total}$ near the final stage of the main interaction. These fractions were calculated from the ion density and thermal and flow velocities of the background ions. We observe that for higher Mach numbers and driver densities, a significant percentage of the background ions' energy is thermal energy, which is not included in Equation (2.25). For low Mach numbers, the thermal energy is negligible, and Equation (2.25) describes well the background energy, as seen in

Figure 2.6 a).

In this work, we focus on low Mach numbers and do not attempt to consider instabilities in Equation (2.25). With the confirmation that Equations (2.24) to (2.26) correctly describe the energy of the system for the parameters of interest, we can now obtain analytical expressions for the different coupling parameters.

2.5 Coupling parameters

2.5.1 Derivation of the analytical expressions

In Section 2.4.4, we confirmed that Equations (2.24) to (2.26) can be used to represent the energy variations of the system for most parameters. We can finally derive the analytical expressions for v_c, v_f, and α, with the compressed density and magnetic field ratios of the background (Equation (2.20)), the pressure balance at the boundaries of the plasmas (Equation (2.22)), and the energy conservation equation (Equation (2.23)).

The derivation of the three coupling parameters is presented in Appendix A.1. We show that if we define the Alfvénic Mach number M_A with the initial background plasma parameters

$$M_A = \frac{v_0}{v_A} \ , \ v_A = \frac{B_0}{\sqrt{4\pi n_0 m_{i,0}}} \ , \tag{2.27}$$

and the quantity R_n, which depends on the density and mass ratios between the driver and background plasmas

$$R_n = \frac{1}{2}\left(\frac{n_0}{n_d}\frac{m_{i,0}}{m_{i,d}}\right)^{\frac{1}{2}} \ , \tag{2.28}$$

then the coupling parameters α, v_c, and v_f can be calculated with

$$\alpha = \frac{1+M_A}{1+R_n} \tag{2.29}$$

$$\frac{v_c}{v_0} = \frac{1}{M_A}\frac{M_A - R_n}{1+R_n} \tag{2.30}$$

$$\frac{v_f}{v_0} = \frac{1}{M_A}\frac{M_A + 1}{1+R_n} \ . \tag{2.31}$$

These analytical expressions for the three coupling parameters depend only on the initial parameters, as initially intended. We stress that these three quantities are easily calculated from the magnetic diagnostics of the simulations and of the experiments, and we can use them to evaluate the coupling of the system.

From Equations (2.24) and (2.25), we obtain that the transfer of energy from the driver plasma to the background plasma is

$$\frac{\Delta E_0}{-\Delta E_{\mathsf{d}}} = \frac{M_A - R_n}{M_A + 1} = \frac{v_c}{v_f} \ . \tag{2.32}$$

The ratio between the coupling and front velocities is then a direct tool to evaluate the efficiency of the energy transfer from the driver to the background.

The equations shown here are only valid for the main interaction of the system, *i.e.*, before all the

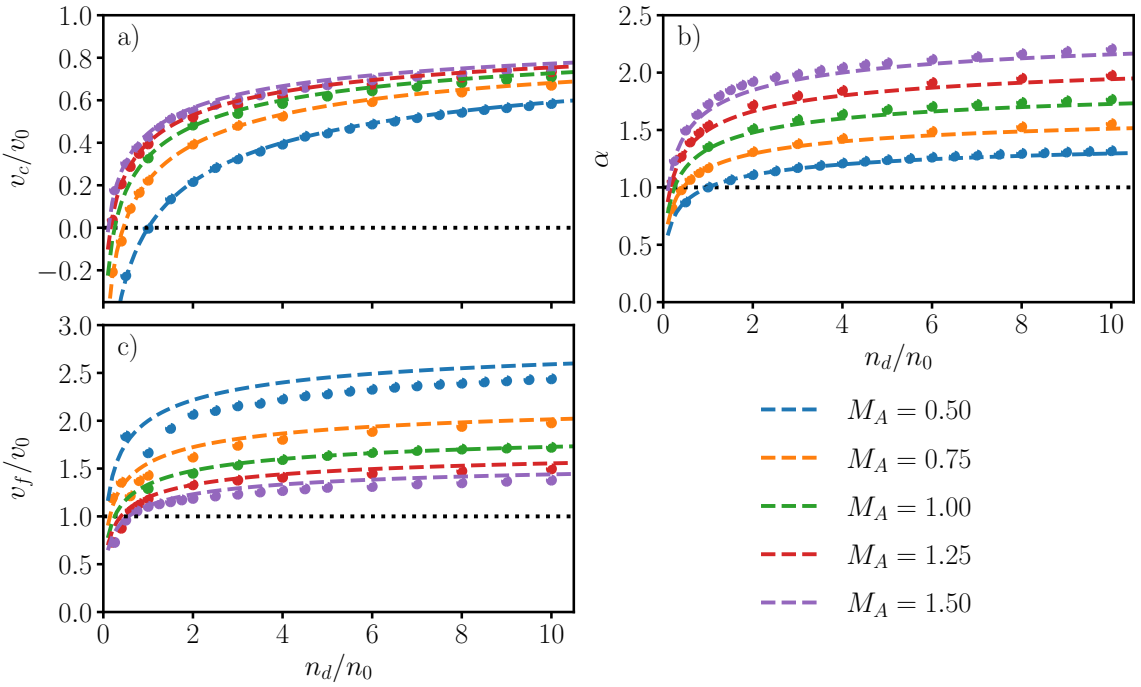

Figure 2.7: Comparison between the coupling parameters measured in the simulations for a) v_c/v_0 with Equation (2.30), b) α with Equation (2.29), and c) v_f/v_0 with Equation (2.31), for different M_A and n_d/n_0 values. These simulations considered $m_{i,d} = m_{i,0}$. The coupling parameters measured in the simulations are represented by dots, and the analytical expressions by dashed lines.

driver ions are reflected and the velocity of the magnetic cavity changes. After the main interaction, the reflected driver ions can still have enough energy to push the background forward, creating a second coupling interaction between the driver and the background.

2.5.2 Dependency on the driver density

We now verify the validity of Equations (2.29) to (2.31). Figure 2.7 shows the measured values for the coupling parameter ratios α, v_c/v_0, and v_f/v_0, for multiple simulations with different Mach numbers M_A and driver densities n_d, with $m_{i,d} = m_{i,0}$. The measured coupling parameters are plotted alongside Equations (2.29) to (2.31). As previously mentioned, these coupling parameters were measured in the simulations by finding the locations of discontinuities A and B (see Figure 2.4).

Figure 2.7 shows that Equations (2.29) to (2.31) can be used to describe the coupling of the system for a wide range of parameters. In Figure 2.7 a) we see that for higher Mach numbers, the coupling velocity increases since the background magnetic field is lower, and offers less resistance to the motion of the driver. Similarly, as the driver density increases, the driver plasma can exert a higher pressure on the background, leading to higher coupling velocities. As previously discussed in Section 2.4.4, some of the simulations performed did not have a sufficiently high driver density and were not able to push the background plasma, leading to negative coupling velocities. These simulations correspond to the scenarios $2n_d m_{i,d} v_0^2 < B_0^2/8\pi$. The measured v_c values are consistent with Equation (2.30), for the parameter ranges considered.

In Figure 2.7 b), the measured α values of the simulations are compared to Equation (2.29). Similarly to the coupling velocity, α increases with the Mach number and the driver density. For the sim-

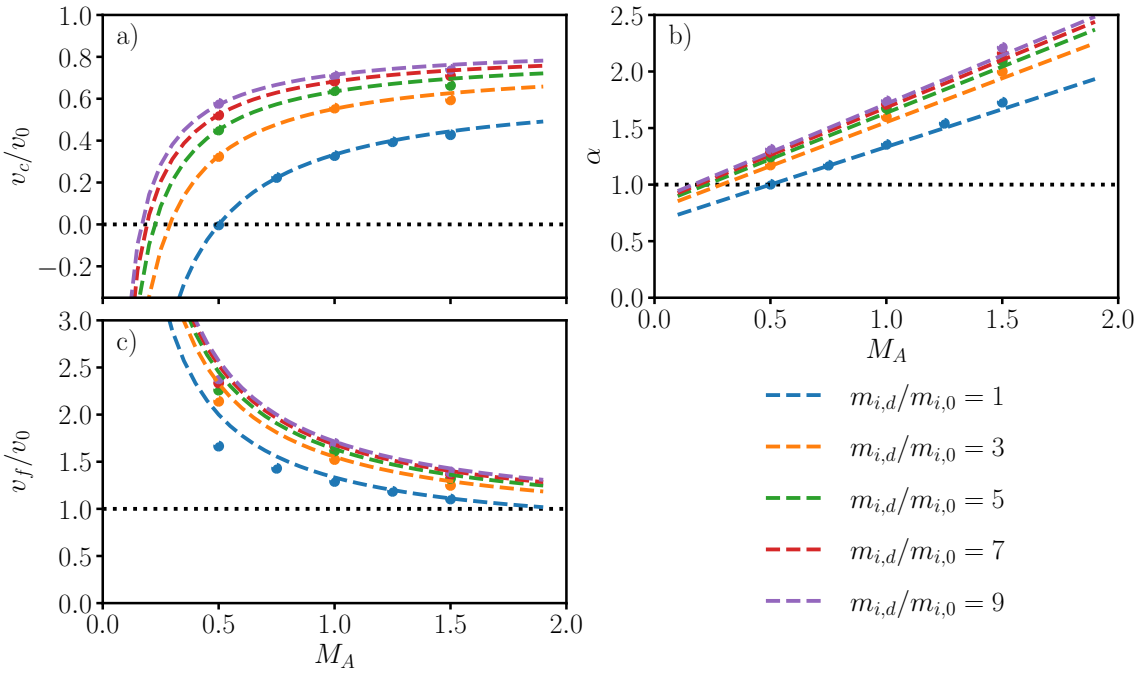

Figure 2.8: Comparison between the coupling parameters measured in the simulations for a) v_c/v_0 with Equation (2.30), b) α with Equation (2.29), and c) v_f/v_0 with Equation (2.31), for different M_A and $m_{i,d}/m_{i,0}$ values. These simulations considered $n_d = n_0$. The coupling parameters measured in the simulations are represented by dots, and the analytical expressions by dashed lines.

ulations with negative coupling velocities, we observe that $\alpha < 1$, which means that the background suffered a magnetic decompression. The α values obtained with the simulations are consistent with Equation (2.29).

Finally, in Figure 2.7 c), we see that the front velocity v_f measured in the simulations is mostly consistent with the values calculated with Equation (2.31). The font velocity increases with the driver density but decreases with the Mach number. For low and high Mach numbers, the small differences between the simulations and the analytical equations are more meaningful than in Figures 2.7 a) and b).

For low Mach numbers, these differences are associated with the difficulty in measuring v_f in the simulations. As we saw in Figure 2.7 b), for low Mach numbers, the compressed magnetic field is almost equal to the initial magnetic field, *i.e.*, $\alpha \approx 1$, and it becomes more challenging to separate the compressed region from the unperturbed background region in the simulations. Additionally, the large width associated with discontinuity B and the waves that form in the background plasma (see Figure 2.1), also lead to difficulties in the measurement of the front velocity in the simulations. For high Mach numbers, Equation (2.25) underestimates the energy of the background since it does not consider instabilities, leading to the differences between the simulations and Equation (2.31), as discussed in Section 2.4.4.

2.5.3 Dependency on the driver ion mass

To fully verify the validity of the deduced coupling equations, we now compare the coupling parameters measured in the simulations with Equations (2.29) to (2.31) for different driver ion masses $m_{i,d}$ and Mach numbers M_A in Figure 2.8. The simulations shown in this Section consider $n_d = n_0$.

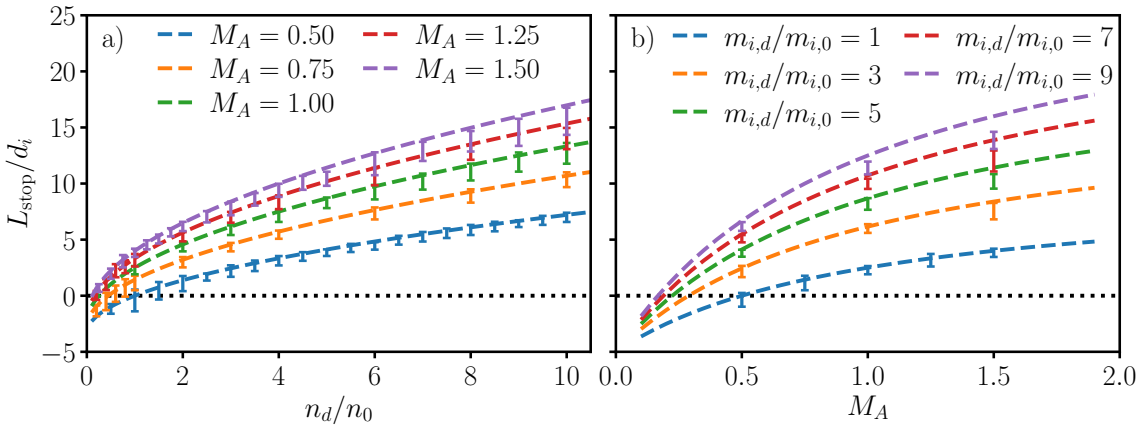

Figure 2.9: Comparison between the stopping distance L_{stop} measured for multiple simulations, with the uncertainty represented by the errorbars, and calculated with Equation (2.33), by the dashed lines. The errorbars account for the non-sharp magnetic cavity reflection in some simulations. a) Scan for different driver densities n_d and Mach numbers M_A, with $m_{i,d} = m_{i,0}$. b) Scan for different Mach numbers M_A and driver ion masses $m_{i,d}$ with $n_d = n_0$.

Similarly to the density scan of Figure 2.7, the results obtained in the simulations are consistent with Equations (2.29) to (2.31). Once again, Equation (2.31) overestimates the front velocities, in particular for low Mach numbers. The results presented in Sections 2.5.2 and 2.5.3 demonstrate that Equations (2.29) to (2.31) successfully describe the coupling between the driver plasma and the background plasma, and now, we can use them to evaluate other characteristics of the system.

2.5.4 Stopping distance

In Sections 2.5.2 and 2.5.3, we showed that we can use the obtained analytical expressions to describe how the system evolves over time for a range of parameters. These equations are also useful to obtain other parameters of the system, such as the stopping distance L_{stop}, *i.e.,* the maximum distance that the magnetic cavity can travel through the background region, during the main interaction of the system.

As previously discussed, the reflection of the magnetic cavity that we observed in Figure 2.2 occurs nearly at the same time as the full reflection of the driver by the background. The magnetic cavity travels a distance L_{stop} through the background region, with velocity v_c, while the driver with a length L_x is reflected by the background with a velocity $v_0 - v_c$. The stopping distance can then be determined by

$$\frac{L_x}{v_0 - v_c} = \frac{L_{\mathrm{stop}}}{v_c} \iff L_{\mathrm{stop}} = L_x \frac{v_c}{v_0 - v_c} = L_x \frac{M_A - R_n}{R_n(1 + M_A)} \,. \tag{2.33}$$

To test Equation (2.33), Figure 2.9 shows the measured stopping distance L_{stop} in the simulations, at the end of the main interaction, and the corresponding values calculated from Equation (2.33). Figure 2.9 a) shows the results for different driver densities n_d and Mach number M_A values, and Figure 2.9 b) for different driver ions masses $m_{i,d}$ and M_A.

Similarly to the coupling parameters, Figure 2.9 shows good agreement between the deduced expression and the distances measured in the simulations, especially for low Mach numbers and low driver ion masses. For high Mach numbers and masses, the stopping distances start to be overestimated by

Equation (2.33). As we observed in Figure 2.7 a) and Figure 2.8 a), the coupling velocity is close to v_0 for these values. Since the stopping distance, calculated by Equation (2.33), is proportional to $v_c/(v_0 - v_c)$, it is very reactive to small variations of v_c, for $v_c \approx v_0$. This means that, although the calculated v_c were consisted with the data measured in the simulations, the small differences between Equation (2.30) and the simulations may lead to big differences in the L_{stop} values, as we see in Figure 2.9.

Finding an analytical expression for the stopping distance can be rather useful because it can give an estimation of the typical scales of the system. Equation (2.33) can be also useful to determine unknown parameters in the experiments.

2.5.5 Applicability to experiments

Through Section 2.5, we observed that we could relate the coupling parameters with the initial parameters of the system by using Equations (2.29) to (2.31). In the experiments with a similar setup to those presented in Section 1.2.1, there is high uncertainty on some parameters of the system, in particular, on the driver and background densities n_d and n_0, and the fluid velocity v_0. We can use Equations (2.29) to (2.31) to estimate these quantities. Rewriting these, we obtain

$$n_0 = \frac{B_0^2(\alpha-1)^2}{4\pi m_{i,0} v_0^2} \qquad\qquad n_d = \frac{\alpha^2 B_0^2}{16\pi m_{i,d}(v_0 - v_c)^2} \; . \tag{2.34}$$

We can use these equations to determine some parameters of the experiments, for the cases $M_A \sim 1$. However, it requires that we know the experimental value of v_0, which normally is uncertain. We also need to be careful for the cases where n_d is much larger that n_0. As we observe in Figure 2.7, for large n_d values, the coupling parameters start to change slowly with n_d. This means that, for these ranges, similar coupling parameters could lead to very different density values.

Finally, we look at possible applications of Equation (2.33). In experiments with similar configurations, the stopping distance L_{stop} is normally used as a benchmark, to estimate some initial parameters of the system. This is normally done by using the equal mass radius R_m for high Mach numbers, which is obtained when we consider that the driver stops when it overruns an equal mass of background plasma

$$n_d m_{i,d} L_x = n_0 m_{i,0} R_m \iff R_m = \frac{n_d m_{i,d}}{n_0 m_{i,0}} L_x \; . \tag{2.35}$$

We consider that the driver expansion is only 1D, as in our simulations. For low Mach numbers, the magnetic stopping radius R_B is used instead, which is obtained when we consider that all the driver energy was used to expel the background magnetic field, leading to

$$\frac{1}{2} n_d m_{i,d} v_0^2 L_x = \frac{B_0^2}{8\pi} R_B \iff R_B = R_m M_A^2 \; . \tag{2.36}$$

If we considered the energy transferred both to the magnetic field and the background plasma, we can also have the Equation (2.37), that should be a better at predicting the stopping distance of the

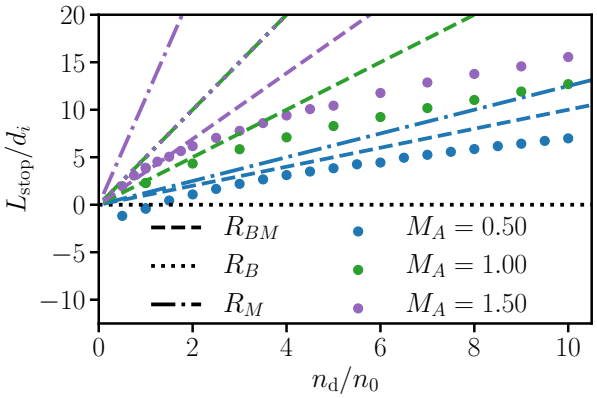

Figure 2.10: Comparison between the stopping distance L_{stop} measured for multiple simulations (dots), and the analytical Equations (2.35) to (2.37) deduced in previous works (lines). The colors represent the different Mach numbers, and the line styles represent the different equations.

magnetic cavity for $M_A \sim 1$

$$\frac{1}{2} n_d m_{i,d} v_0^2 L_x = \frac{1}{2} n_0 m_{i,0} v_0^2 R_{BM} + \frac{B_0^2}{8\pi} R_{BM} \iff R_{BM} = \frac{R_B}{1 + M_A^2} \,. \tag{2.37}$$

As we can see in Figure 2.10, these equations, however, fail for the simulations performed, when compared to Equation (2.33) and Figure 2.9. These happens, because the previous equations consider that the driver transfers all its energy to the background region, and do not account for change in the densities and magnetic fields, nor mixed energy transfers to the background plasma and background magnetic field. Because of this difference between the measured distances and the expressions, previous works tended to use the previous equations as scaling laws or in fitting models, and adjust the models for each laboratory and used for benchmark. Having a better estimate for L_{stop}, such as that in Equation (2.33), for the ranges $M_A \sim 1$, could thus lead to improved benchmarks for future experiments.

Some caution must also be considered when applying these results to the experiments. For most of the experiments performed, that consider a driver plasma expanding to a magnetized background plasma, the driver plasma is not long enough to reach the quasi-stationary regime that we observed in our simulations. This may lead to weak coupling between the driver and the background plasmas in the experiments, invalidating the analytical equations for the coupling, while in the simulations, for the parameters observed, we always observed strong coupling. Furthermore, in the experiments, we may not be able to consider that the driver has a plasma with initial uniform density and uniform velocity profile, like in the simulations. Besides the non homogeneity of the experiments, we must also consider 3D effects, such as the driver expansion, the experiments have higher temperatures than consider in the simulations, and possible multiple ion-species in the plasmas.

2.6 Conclusions

A vast range of space and astrophysical scenarios are driven by the rapid expansion of plasmas through magnetized mediums. To understand the evolution of these systems, these systems are also replicated in laboratory, as it was done in the LAPD experiments showed in Figure 1.4, where a driver plasma flowing against magnetized plasma and a dipole. In this Chapter, we studied an idealized system

of what typically occurs in these experiments and astrophysical scenarios, by considering a uniform unmagnetized driver plasma flowing with constant velocity against a uniform magnetized background plasma, and studied these systems by performing simulations and analytical studies.

As discussed in this Chapter, the jump in the magnetic field from the unmagnetized driver to the magnetized background regions, leads to an electric field that slows down the driver particles that reached near the background. During this process, the energy and momentum lost by the driver plasma is transferred to the magnetized background plasma, leading to a region of compressed magnetic field and density in the background. Due to the large discrepancies between the ion and electron masses, a diamagnetic current forms in the interface driver-background, and the magnetic field is expelled by the driver, leading to the formation of a magnetic cavity.

The driver-background interaction also leads to an acceleration of the initially stationary background plasma particles, and as a result, the driver plasma pushes the background forward, until it has no more energy and momentum. We also observed that this interaction leads to the formation of waves and instabilities in the background plasma. For the configuration considered in our simulations, where the plasma flows are perpendicular to the magnetic field, we detected both slow and fast magnetosonic waves. For sub-Alfvénic Mach numbers $M_A < 1$ (and low driver densities), the fluctuations in the background is mostly described by these two waves, but for super-Alfvénic Mach numbers $M_A > 1$ (and high driver densities), the fluctuations are also driven by instabilities.

As we observed in this Chapter, during the main interaction between these two ideal plasmas considered in our simulations, the driver expels the magnetic field, leading to a magnetic cavity region that travels through the background with constant coupling velocity v_c. As the magnetic field is expelled in the driver region, the averaged magnetic field and density of the background plasma are compressed by a constant ratio α, and this compression travels with constant front velocity v_f. These three quantities (v_c, α, and v_f) describe the coupling between the two plasmas, and increase for higher driver to background density or mass ratios. For higher Mach numbers, the parameters v_c and α increase while v_f decreases. We also observed that, for some parameters, the driver plasma does not have enough momentum and energy to push the background plasma, and instead it is pushed back by the background.

By applying the mass, momentum, and energy conservation laws on the system, similarly to the Rankine-Hugoniot jump conditions, we showed that these three quantities (v_c, α, and v_f) can be calculated accurately from the initial parameters of the system, for Mach numbers $M_A \sim 1$. With the derived analytical expressions, we can determine multiple averaged quantities of the system, such as the distance that the magnetic cavity is able to travel through the background, and understand how the interaction of the plasmas changes their properties. In this Chapter, we also showed that these expressions can be used to estimate some initial parameters of the system that are not very well known in the experiments.

Chapter 3

PIC simulations of laboratory ion-scale magnetospheres

With Chapter 2, we described the interaction of a uniform unmagnetized driver plasma flow with a uniformly magnetized background plasma, for Mach numbers close to one. In general, this interaction results in the transfer of energy from the driver plasma to the background plasma, generating a complex, magnetized plasma flow. If a magnetic obstacle are in the path of this plasma flow, it can be deflected and further compressed, leading to the formation of a magnetosphere. By introducing a dipole in the system, we form a ion-scale magnetosphere. In this Chapter, we investigate the generation of ion-scale magnetospheres with PIC simulations, in the configurations of the LAPD experiments described in Section 1.2.2, and compare the results with the experimental study.

3.1 Setup of the simulations

We have performed 2D PIC simulations with OSIRIS, a massively parallel and fully relativistic PIC code [61, 62], to accurately resolve the plasma kinetic scales characteristic of mini magnetospheres dynamics. These simulations stem from a simplified description of the LAPD experimental setup, represented in Figure 3.1. In these simulations, a driver plasma moves against a background plasma permeated by a uniform magnetic field $\mathbf{B_0}$ and a dipolar magnetic field $\mathbf{B_{dip}}$. $\mathbf{B_0}$ and $\mathbf{B_{dip}}$ are oriented along the z direction and are transverse to the driver plasma flow. Since the most relevant dynamics of the simulations occurs at the ion kinetic scales, all the spatial scales are normalized to the ion skin depth of the background plasma $d_i = c/\omega_{pi} = \sqrt{m_{i,0}c^2/4\pi n_0 e^2}$. In turn, the temporal scales are normalized to $1/\omega_{ci}$, where $\omega_{ci} = eB_0/m_{i,0}c$ is the ion cyclotron frequency of the background. The simulation box is a 12 d_i $\times$ 12 d_i area with open and periodic boundary conditions in the x and y directions, respectively. The flow is in the x direction and the size of the simulation domain in the y direction is large enough to avoid re-circulation of the particles through the whole interaction. The simulations considered 25 particles per cell per species. To resolve the dynamics of the electron kinetic scales, we used 10 grid cells per electron skin depth $d_e = d_i\sqrt{m_e/m_{i,0}}$ in both x and y directions, where m_e is the electron mass.

The driver plasma, shown in region I in Figure 3.1, represents ideally the plasma ablated from the

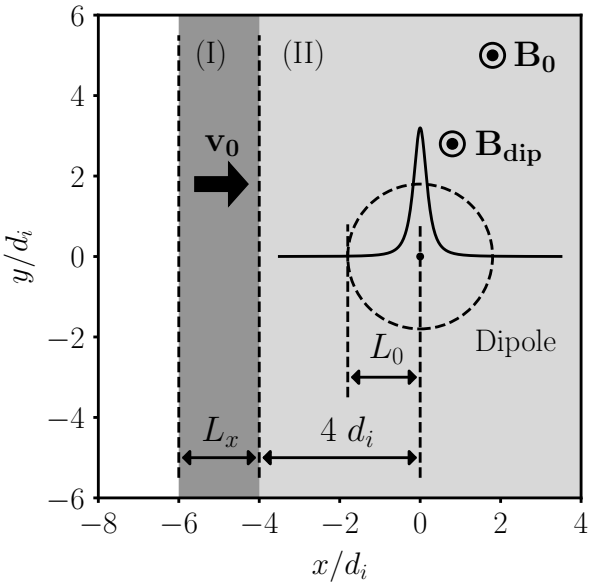

Figure 3.1: Schematic illustration of the initial setup of the 2D PIC simulations performed. The system considers a vacuum region at the left, a driver plasma (I) of density n_d and length L_x, travelling to the right with flow velocity v_0, and a background plasma (II) with constant density n_0 and with an internal magnetic field B_0. A dipole is included at the center of the background region. Both the uniform and the dipolar magnetic fields are oriented in the z direction. An illustration of the effective magnetic obstacle created by the dipole and of the magnetic field profile at $y = 0$ are also shown in a dashed circumference and in a solid black line, respectively.

plastic target in the experiments. We assume that this driver has a length L_x that is typically 2 d_i, and a width L_y that is typically infinite. It has a constant density n_d, and it is initialized moving to the right side with initial flow velocity v_0. The driver is composed of an electron species and a single ion species, with ion mass $m_{i,d}$. Because the driver plasma is reflected during the interaction with the background, an empty region at the left of the driver was added to accommodate the reflecting particles.

The background plasma is represented in region II. It is an 8 d_i length and infinite width plasma and it has uniform density n_0. The initial interface between the driver and background plasma is located at $x_B = -4\ d_i$. Like the driver plasma, it has an electron species and a single ion species, of mass $m_{i,0}$. The background plasma is magnetized with an internal uniform magnetic field $\mathbf{B_0} = B_0\hat{\mathbf{z}}$, and its magnitude is defined such that the Alfvénic Mach number of the flow, $M_A \equiv v_0/v_A = v_0\sqrt{4\pi n_0 m_{i,0}}/B_0$ matches the peak experimental value $M_A = 1.5$, where v_A is the Alfvén velocity.

A dipolar magnetic field is externally imposed in our simulations (*i.e.*, it is added to the plasma self-consistent electromagnetic fields to advance particle momenta but is not included in Maxwell's equations to advance the fields). The dipole is centered at $(x, y) = (0, 0)$ and its associated magnetic field is $\mathbf{B_{dip}} = B_{\rm dip}\hat{\mathbf{z}}$, with $B_{\rm dip} = M/r^3$, where M is the dipolar magnetic moment, $r = \sqrt{x^2 + y^2 + \delta^2}$ is the distance to the origin of the dipole and $\delta = 0.25\ d_i$ is a regularization parameter. For most simulations, the magnetic moment M was chosen such that the expected standoff, obtained from Equation (3.1), is similar to the experimental value $L_0 = 1.8\ d_i$ [39].

$$n_d m_{i,d} v_0^2 = \frac{(B_0 + B_{\rm dip})^2}{8\pi} \tag{3.1}$$

For this particular magnetic moment, the total initial magnetic field $B_0 + B_{\rm dip}$ is $\approx 3.0\ B_0$ at the standoff distance. Near the interface between the driver and background plasmas, the magnetic field of the dipole is relatively small and the initial magnetic field is $\approx 1.2\ B_0$.

In this Thesis, we present simulations with different drivers and magnetic dipole moments. All the simulations presented here, and their respective parameter sets, are listed in Table B.1. Simulation B is used to discuss the overall dynamics of the system, while simulations C, D, and E illustrate the role of the driver length, the density ratio, and the magnetic moment, respectively. Simulations F show the results for more realistic choices of parameters and simulation G for a more realistic driver shape. The physical parameters of the simulations (e.g. M_A, L_0/d_i) were adjusted to be similar to the LAPD experiments, whereas other parameters (e.g. m_i/m_e, v_0, v_{the}) were chosen to make simulations computationally feasible. The experimental and numerical parameters are presented in Table B.2 and compared with lunar mini magnetospheres.

In most simulations, we considered a reduced mass ratio $m_i/m_e = 100$, a flow velocity $v_0/c = 0.1$, and cold plasmas to reduce the required computational resources, allow extended scans over the different parameters of the system, and simplify our analysis. The thermal effects are negligible for the main results, and the chosen ion-to-electron mass ratio is high enough to ensure sufficient separation between electron and ion spatial and temporal scales. We confirm the validity of our assumptions in Section 4.5.

In most of the simulations presented in this and the next Chapter, we have assumed that ions and electrons are initially in thermal equilibrium, and thus used the electron thermal velocities v_{the} shown in Table B.1, to compute the ion thermal velocities v_{thi}. Because we aim to study the role of the hydrogen ions of the experimental driver in the interaction with the background plasma, these simulations considered equal ion masses for the driver and background plasmas, *i.e.*, $m_{i,d} = m_{i,0}$.

3.2 Evolution and formation of a mini magnetosphere

To identify the main magnetospheric and kinetic-scale structures that arise from the initial configuration, simulation B was performed. It considered a driver with length $L_x = 2\ d_i$ and density $n_d = 2\ n_0$ (twice the background density). Figures 3.2 a1-3) represent the total ion density $n_i = n_{i,d} + n_{i,0}$, for three different times, and Figures 3.2 b1-3) show the variation of the z component of the magnetic field, from its initial value, $\Delta B_z = B_z - B_{z,\text{initial}}$.

In Figure 3.2 a1), we see the total ion density for an early time ($t\omega_{ci} = 1.5$). Given the small distance propagated by the driver plasma at this time, the dipolar magnetic field does not significantly affect the interaction between the plasmas. For this reason, we can express the early system as a driver flowing against a uniform magnetized background plasma, like that described in Chapter 2. In Figure 3.2 b1), we observe that this interaction creates a region of compressed magnetic field in the downstream region, where the background plasma is located, and expels the magnetic field in the region of the driver, leading to a magnetic cavity in the upstream region with approximately null magnetic field [29].

In Figures 3.2 a2) and b2), we start to observe the effects of the dipolar magnetic field for a later time ($t\omega_{ci} = 3.0$). As the magnetic pressure exerted against the plasmas increases, a region of compressed

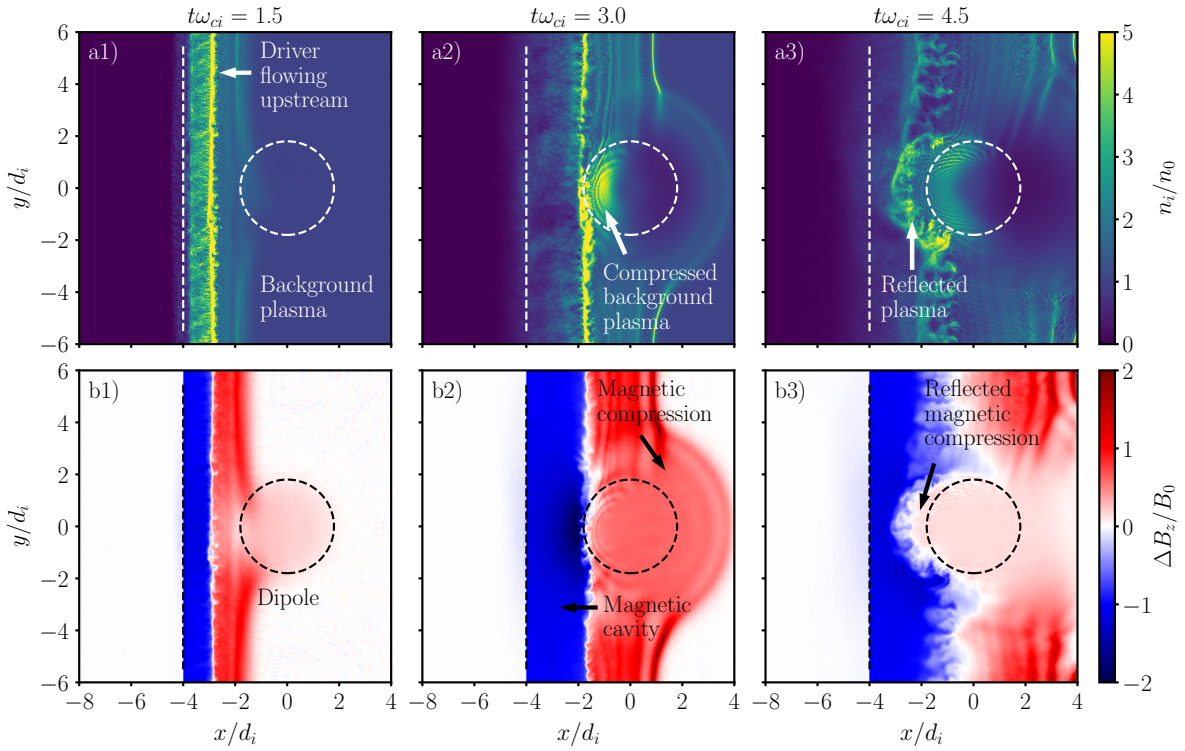

Figure 3.2: Spatiotemporal evolution of a) the total ion density and b) the variation of the z component of the magnetic field in simulation B (see Table B.1 for a list of parameters). Columns 1-3 correspond to three different times in the simulation. The vertical and circular dashed lines mark the initial border between the driver and background plasma and the dipolar magnetic obstacle with radius L_0, respectively.

background plasma forms in front of the dipole, as Figure 3.2 a2) shows. After the interaction between the background and the dipole, the magnetic field pressure becomes large enough to counterbalance the kinetic pressure of the driver, reflecting it upstream. This can be seen in Figure 3.2 a3) for a subsequent time ($t\omega_{ci} = 4.5$). After the reflection, there is no longer a plasma flow pushing the magnetic compression forward or holding the decompression by the left side of the background region, and as a result, the region near the dipole quickly decompresses — see Figure 3.2 b3).

3.3 Magnetic field and current density synthetic diagnostics

To compare the numerical results with the experimental data shown in Figure 1.4, synthetic diagnostics were obtained from the simulations. In Figure 3.3, the variation of the magnetic field ΔB_z and the density current J_y measured at the axis of symmetry $y = 0$ and as a function of time are plotted for simulation B. These diagnostics are important to comprehend the system dynamics, due to the importance of the z direction of the magnetic field in the motion of the particles.

The main features of Figure 3.3 are consistent with the experimental results. In the magnetic field plot of Figure 3.3 a), both the upstream magnetic cavity and the downstream magnetic compression are present. Between $t\omega_{ci} = 0$ and $t\omega_{ci} \approx 1.5$, the system behaves approximately as a driver piston moving against a uniform magnetized plasma. As the driver pushes the background plasma and magnetic field, the discontinuity that separates these two media travels at constant coupling velocity $v_c < v_0$, measured as $v_c \approx 0.49\ v_0$ for this simulation. The leading edge of the compression of the magnetic field travels

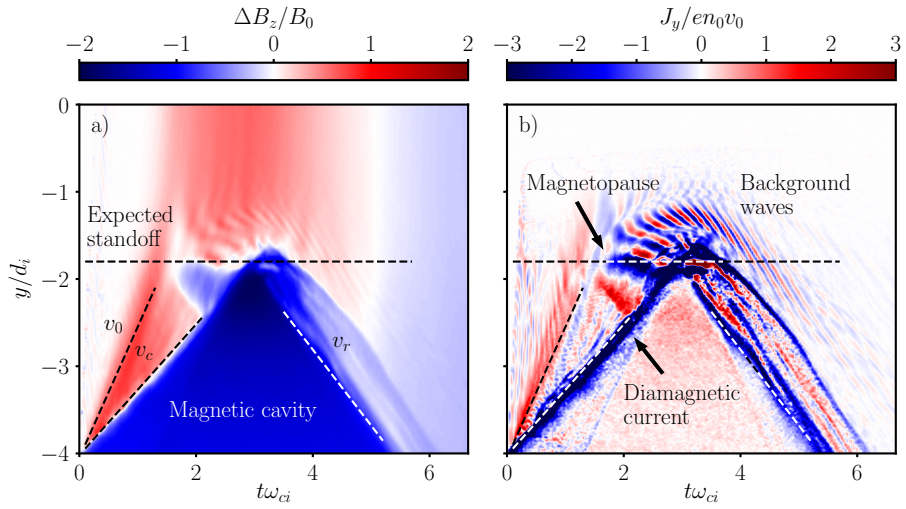

Figure 3.3: Temporal evolution of a) the variation of the magnetic field B_z and b) current density J_y at $y = 0$ for the simulation B. The driver has a 2 d_i length and a density $n_d = 2\ n_0$. The dashed lines have slopes that match the flow velocity v_0, the coupling velocity v_c and the reflection velocity v_r.

with a velocity close to v_0 for the runs considered.

The driver experiences increasingly higher magnetic fields until the magnetic pressure is enough to reflect the driver near the expected standoff $x_0 = -L_0$, at $t\omega_{ci} \approx 3$. The magnetic cavity and magnetic compression are also reflected, and the boundary between these two regions travels with a velocity v_r after reflection. The background magnetic decompression is seen after $t\omega_{ci} = 5$.

In the current density plot of Figure 3.3 b), we can observe the diamagnetic current that supports the magnetic field gradient between the driver and background plasmas and that identifies the leading edge of the magnetic cavity. During the driver reflection, this current branches into multiple components due to the multi-stream velocity distributions developed in the driver and background plasmas. We can also verify that this structure is reflected near the expected standoff $x_0 = -L_0$. Between $t\omega_{ci} \approx 2$ and $t\omega_{ci} \approx 3$, a second current structure is present in the background region. It is associated with the magnetopause of the system and the small decompressed field region that we see in Figure 3.3 a), and it arises from the interaction of the accelerated background ions with the dipole, as we show in Section 4.4. The presence of these two current structures is consistent with the experimental results.

In Figure 3.3 b) we can also see the formation of waves in the background plasma, near the dipole region. These waves are excited in regions of highly non-uniform density and magnetic field, and have periods and wavelengths between the ion and electron kinetic scales. We have also verified that their properties change significantly for different ion thermal velocities. A detailed characterization of these waves and the conditions for their formation is out of the scope of this Thesis, and shall be addressed in a future work. However, our early results suggest that these waves may be slow magnetosonic waves under a dipolar magnetic field.

3.4 Phase spaces and motion of the particles

To better understand the particle motion during the events described in Section 3.2, we show in Figure 3.4 the phase spaces of ions and electrons located near $y = 0$. For the ions, the x component

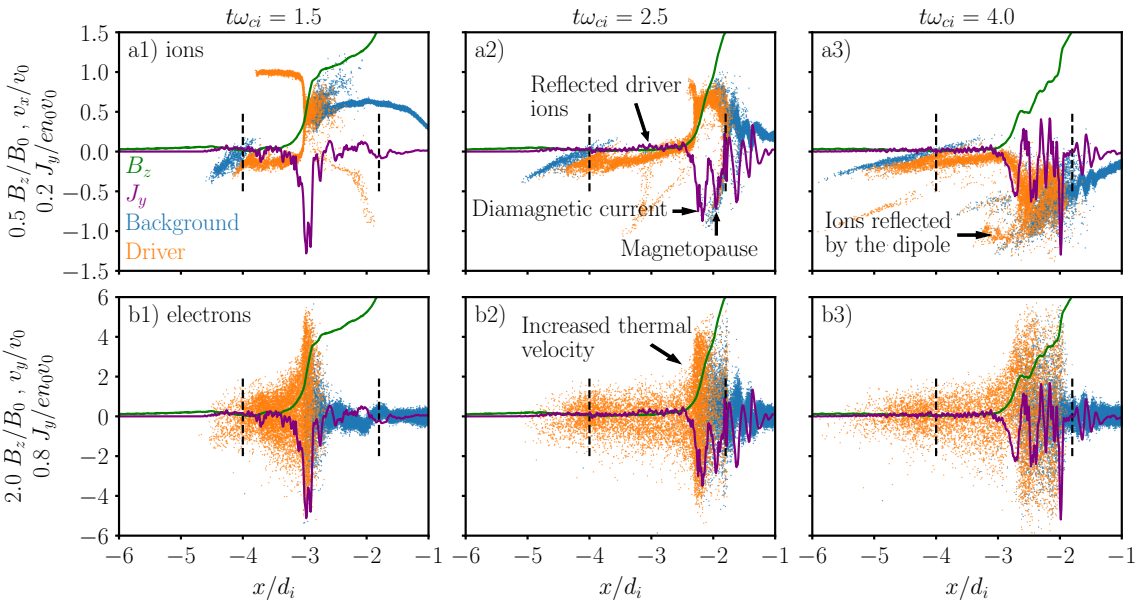

Figure 3.4: Ion (a) and electron (b) phase spaces, and magnetic field B_z and current density J_y profiles at $y = 0$, for simulation B and for three different times (1-3). The particles shown were randomly selected in the region $-0.2\ d_i < y < 0.2\ d_i$. The frames labeled a1) to a3) show the v_x velocity of the ions, while the frames labeled b1) to b3) show the v_y velocity of the electrons. Blue/orange markers correspond to background/driver plasma particles. The green and purple lines correspond to the magnetic field B_z and current density J_y, respectively. The left dashed line marks the initial border between the driver and the background plasmas, and the right dashed line marks the expected standoff $x_0 = -L_0$.

of the velocity of the particles is presented, to illustrate their reflection and accumulation, while for the electrons, the y component is shown instead, to show the formation of the currents. The magnetic field B_z and the current density J_y profiles for $y = 0$ are also represented. Once again, we used the parameter set B of Table B.1.

Figure 3.4 a1) shows the v_x velocity of the ions when the dipole field is still negligible. The ions initially move upstream with velocity v_0 until they interact with the background field. After reaching the background, they are decelerated and reflected by electric field at the interface between the plasmas [29], and end up with a flow velocity that is close to zero for the simulation considered. The reflection occurs near the boundary of the magnetic cavity, which moves with velocity v_c through the background, as mentioned above. During this stage, the background ions accelerate from rest to velocities of average close to v_c.

The driver and the accelerated background ions continue to approach the dipole until they are reflected. This can be seen in Figure 3.4 a2). During this interaction, two main current structures are visible in the J_y profile. The first one (from the left) corresponds to the typical diamagnetic current, while the second one corresponds to the magnetopause. To the right of these two main current structures, we can see the background waves observed in Figure 3.3 b). In Figure 3.4 a3), the driver ions are totally reflected. The ions reflected by the dipole obtain a velocity close to $-v_0$, while the magnetic cavity moves back with velocity v_r.

Because the simulation considers a cold plasma approximation, the ion thermal velocities remain small everywhere and for most of the time, except at the boundary between the two plasmas, where

the velocity of the ions changes abruptly. The same does not occur for the electrons. We can see in the v_y velocity of the electrons, represented in Figures 3.4 b1) to b3) that, although the electron thermal velocities are initially small, they rapidly increase considerably. At the boundary, the electrons can reach thermal velocities of $6\ v_0$, much higher than the ion velocities. Because the electron and ion density profiles are very similar during the entire evolution of the system, the current density $J_y = e(n_i v_{iy} - n_e v_{ey})$ is then mainly transported by the electrons, where n_j is the density and v_{jy} the y component of the velocity of the ions and electrons ($j = i, e$, respectively). This is also consistent with the observed spatial distribution of electrons during the reflection, which shows an excess of fast electrons around the standoff position.

3.5 Pressure balances and formation of the magnetopause

To identify the pressure balances associated with the two observed standoffs, and because the magnetic and kinetic pressures vary over time, we studied the temporal evolution of the different plasma and magnetic pressure components of the system. In particular, we calculated the spatial profiles of the magnetic pressure $B^2/8\pi$, the ram pressure $n_j m_j v_{flj}^2$ and the thermal pressure $n_j m_j v_{thj}^2$ as functions of time for $y = 0$. In these expressions, n_j, m_j, v_{flj} and v_{thj} refer to the density, mass and flow and thermal velocities, respectively, of the ions ($j = i$) and electrons ($j = e$). The magnetic pressure was calculated from the magnetic field measured in each PIC grid cell located at $y = 0$. The flow and thermal pressures were calculated from averaged particle data. To ensure that the calculation of each kinetic pressure considered a sufficiently large number of particles, all the particles between $-0.1\ d_i < y < 0.1\ d_i$ were binned into equal-sized bins of width $0.05\ d_i$ over the x direction. For each bin we computed: i) the average density of each species, ii) the flow velocity, corresponding to the average of the velocity of the particles, and iii) the thermal velocity, corresponding to the standard deviation of the velocity of the particles [65]. With these averaged quantities, the ram and thermal pressures were calculated in each bin for each species of ions and electrons and each component of the velocity x, y, and z. The y and z velocity components, however, are negligible for the pressure calculation.

These pressure profiles were obtained and are plotted in Figure 3.5 for times where a) the magnetopause and b) the diamagnetic current standoff can be observed. The kinetic pressures represented were calculated by adding all the components of the ram and thermal pressures of the ions and electrons for the background (P_0) and the driver (P_d) plasmas. In Figure 3.5 a) and b), we represent also the total and relative magnetic field pressures, defined as $P_\mathrm{mag} = B_z^2/8\pi$ and $P_\mathrm{rel} = P_\mathrm{mag} - B_0^2/8\pi$, respectively. The pressures were normalized to the initial ram pressure of the driver ions.

Figure 3.5 a) shows the magnetic and kinetic pressures at time $t\omega_{ci} \approx 2.33$ where we observed the magnetopause in Figure 4.4 b3). When the driver starts pushing the background, the pressure of the driver at the interface between the plasmas increases because the driver density and thermal velocities also increase. During the interaction, the driver transfers energy and momentum to the background plasma, and as a result, the background develops a strong kinetic pressure. At the time represented in Figure 3.5 a), the background plasma pressure equals the total and the dipolar magnetic pressures in $x \approx -1.4\ d_i$, near the location of the magnetopause current of Figure 4.4 b3). This observation sup-

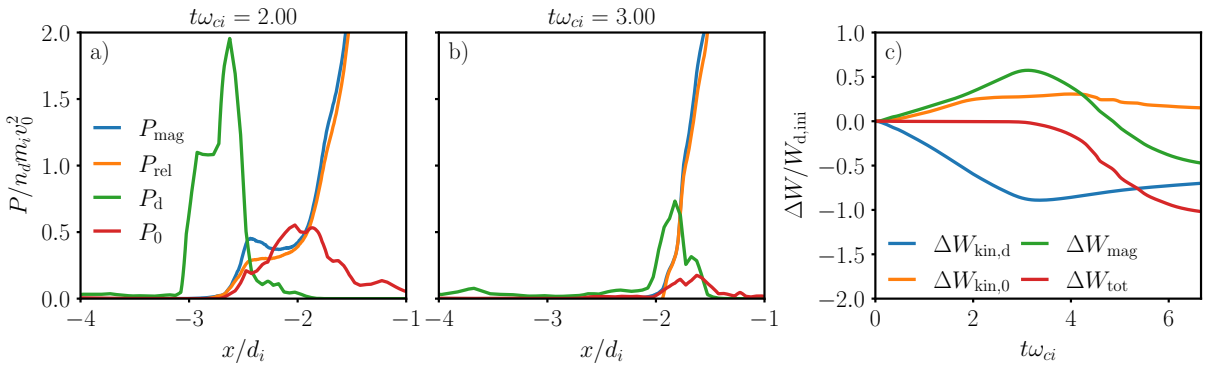

Figure 3.5: Pressures profiles calculated for simulation E3 with a magnetic moment $M = M_0/2$ (shown in Figure 4.4 c)), during the occurrence of a) the magnetopause and b) the standoff of the diamagnetic current. The magnetic pressures are $P_{\rm mag} = B_z^2/8\pi$ and $P_{\rm rel} = P_{\rm mag} - B_0^2/8\pi$. The kinetic pressures $P_{\rm d}$ and P_0, corresponding to the driver and background plasmas, respectively, consider both the ions and electrons and the flow and thermal components of the velocity. c) Temporal evolution of the variation of the total kinetic energies of the driver $\Delta W_{\rm kin,d}$ and background $\Delta W_{\rm kin,0}$ plasmas, the magnetic energy $\Delta W_{\rm mag}$, and the total energy of the simulation box $\Delta W_{\rm tot}$. The total energy is calculated by adding all the kinetic energies and the electric and magnetic energies. Since the background plasma is magnetized, the electric energy term is many orders of magnitude smaller than the magnetic energy term. The energies were normalized to the initial total energy of the driver ions $W_{\rm d,ini}$. The loss of energy conservation near $t\omega_{ci} \approx 4$ is caused by the escape of background plasma particles and magnetic field through the right hand side of the simulation box.

ports the hypothesis that this current emerges from the standoff between the background and magnetic pressures. Figure 3.5 b) shows the pressures for $t\omega_{ci} = 3$ where we see the beginning of the reflection of the driver. The driver pressure equals the magnetic and dipolar pressures near $x_0 = -L_0 \approx -1.4\ d_i$. After this time, the driver is incapable of moving any further into the background because the magnetic pressure exceeds its kinetic pressure.

The energy variations integrated over the entire simulation domain can also help us understand the system dynamics. Figure 3.5 c) shows the variation of the total driver and background kinetic energies, $\Delta W_{\rm kin,d}$ and $\Delta W_{\rm kin,0}$, respectively, as well as the variation of the magnetic energy $\Delta W_{\rm mag}$, and of the total energy $\Delta W_{\rm tot}$. The kinetic energies of the background and driver plasmas consider all ions and electrons, and not only those around $y = 0$, as previously considered. In early times $t\omega_{ci} < 3$, as the driver and background plasmas interact, the driver transfers its energy to the background plasma and the magnetic field. The total energy, given by the sum of the electromagnetic energy and kinetic energies, remains constant during this period. After the driver is fully reflected by the dipole for $t\omega_{ci} > 3$, the magnetic field loses most of its energy to the background and driver plasmas, leading to a drop of the magnetic energy. After $t\omega_{ci} \approx 4$, the background ions start to leave the simulation box, and the total energy is no longer conserved. The background kinetic energy remains approximately constant because the background plasma loses energy to the sink at the right boundary of the simulation but gains energy from the magnetic field. For both driver and background plasmas, the ions carry most of the energy.

From Figure 3.5, we can identify the positions where multiple pressure balances occur, and therefore, develop an insight into the pressure equilibria that are behind the structures of the current density synthetic diagnostics. Using the previously calculated pressures, we obtained the equilibrium positions where certain pressure balances manifested and plotted them in Figure 3.6 alongside J_y.

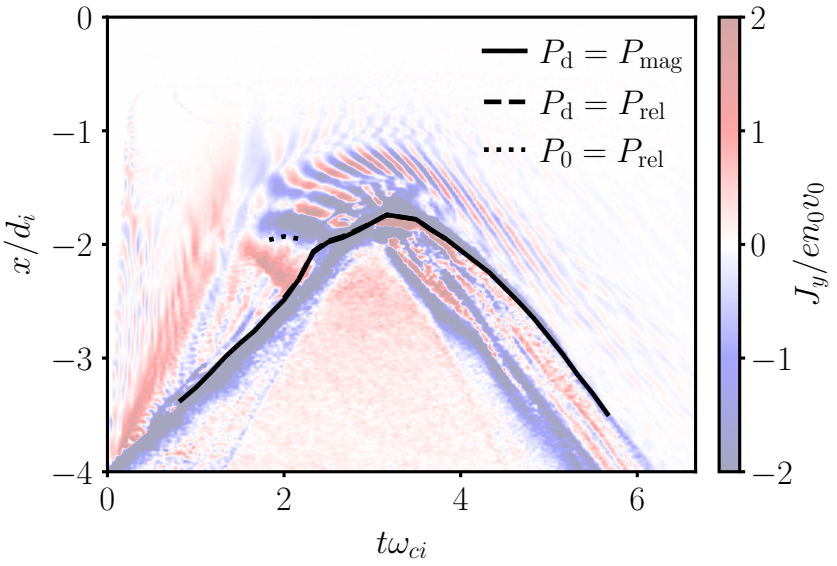

Figure 3.6: Temporal evolution of J_y at $y = 0$, with the closest locations to the dipole of different pressure balances for multiple times. The represented locations of pressure balances are the equilibria between the driver kinetic pressure $P_{\rm d}$ with the total magnetic field pressure $P_{\rm mag} = B_z^2/8\pi$, represented by the solid line; the background kinetic pressure P_0 with the pressure exerted by the relative magnetic field $P_{\rm rel} = P_{\rm mag} - B_0^2/8\pi$, by the dotted line, and $P_{\rm d} = P_{\rm rel}$, by the dashed line. The results correspond to simulation E3 (see Table B.1).

This analysis shows that the system has, in general, two magnetopause structures: one driven by the background, and one by the driver plasma. The former structure is defined by the balance $P_0 = P_{\rm rel}$. For the latter structure to form, the driver needs to have enough energy to push the diamagnetic current up to the magnetopause, defined by Equation (3.1). This is illustrated in Figure 3.6, where we show the location of the pressure equilibrium between the driver kinetic pressure and the total magnetic pressure, $P_{\rm d} = P_{\rm mag}$.

As shown in Figure 3.5, the current associated with the background magnetopause seems to overlap with the region of background and magnetic pressure balance. Unlike the driver, the background plasma is magnetized. If we neglect the compression of the magnetic field in the downstream region, the pressure balance that describes this magnetopause can then be estimated by the equilibrium of the kinetic pressure of the background plasma with the relative magnetic pressure, $P_0 = P_{\rm rel}$. In Figure 3.6, we show that this pressure balance, represented by the dotted line, describes well the position of the current feature identified as the magnetopause between times $t\omega_{ci} \approx 2$ and $t\omega_{ci} \approx 3$.

After $t\omega_{ci} \approx 3$, the magnetopause current is well described by the pressure balance $P_{\rm d} = P_{\rm rel}$, as illustrated by the dashed line in Figure 3.6. In fact, after inspecting the phase spaces in Figures 3.4 a3) and b3), we can observe that a combination of driver plasma particles (separated from the bulk distribution) and background ions pushes the dipolar field and sets the position of the magnetopause.

We stress that, because we are determining equilibria via MHD pressure balances but are checking the intersection between pressure curves with kinetic resolution, some caution must be made to ensure that we are observing the equilibrium between pressures and not merely the interface between the different regions of interest. To ensure that the pressure equilibria were correctly obtained, the corresponding

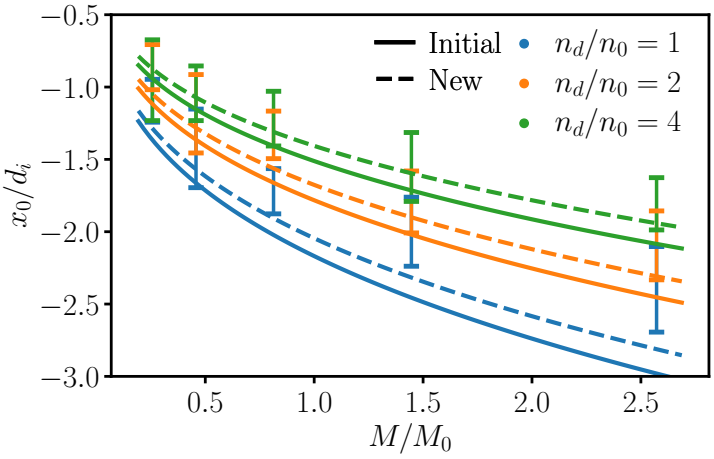

Figure 3.7: Comparison between the standoff distance $x_0 = -L_0$ calculated from Equation (3.1) (line - Initial), Equation (3.2) (line - New), and the measured standoff positions in the simulations (error bars). M_0 represents the magnetic moment that leads to $L_0 = 1.8\ d_i$ from Equation (3.1).

pressure profiles were always carefully inspected with additional diagnostics.

3.6 Applying the coupling study to the pressure equations

For our simulations with ion-scale magnetospheres, we considered a driver plasma flowing against a uniform magnetized background plasma, and a dipole located at its center. To estimate the standoff position of the driver plasma $x_0 = -L_0$, we used Equation (3.1), which represents the initial pressure balance between the driver ram pressure the magnetic field pressure. However, as discussed in Chapter 2, the characteristics of the plasmas change from the initial parameters considered in Equation (3.1), with the interaction driver-background, before reaching the dipolar obstacle. More specifically, the magnetic field increases in the downstream region and the driver density increases by a factor of two, since we must also consider the driver plasma reflected by the dipole. The correct pressure balance for the driver standoff should then be

$$2n_d m_{i,d} v_0^2 = \frac{(\alpha B_0 + B_{dip})^2}{8\pi} \ . \tag{3.2}$$

To compare Equation (3.2) to Equation (3.1), we performed a small scan of the driver density and of the magnetic moment. The positions of the diamagnetic current were measured for each simulation and are compared to the expression in Figure 3.7. In the simulations, we ensured that the length of the driver was high enough to measure these positions. Due to small fluctuations of the current positions, these values are show with uncertainties.

As we can observe, for the Mach number $M_A = 1.5$, both Equations (3.1) and (3.2) are able to predict the measured standoff distances, however, the new expression is slightly better. For Figure 3.7, we used Equation (2.29) to calculate the α parameter in Equation (3.2), but as discussed in Section 3.2, the background will start to decompress after the driver reaches the dipole. Therefore, the compression ratio α will decreases over time, and it will be lower than the value calculated from Equation (3.2). We observed that, if we use a lower value for α in Equation (3.2), the measured distances will be even more

consistent with the calculated values.

From the pressure study done in Section 3.5, we also obtained pressure balances that describes the different magnetopauses of the system. Using the coupling expressions deduced in Chapter (2.5), we can also determine analytical expressions for the correspondent pressure balances, that only depend on the initial parameters of the system. The magnetic field on the upstream side of the magnetopause, can be approximated again by αB_0. On the downstream side, the magnetic field is given by $\alpha B_0 + B_{\text{dip}}$. Since αB_0 is present on both sides, to predict the position of the magnetopause, we can make a rough approximation and remove it entirely from the pressure balance. The density of the accelerated background plasma ions increases to a near-constant value during the initial flow, as they move alongside with the magnetic field compression. By looking at Figure 3.3, we can consider that the head of the accelerated background plasma moves with a velocity close to v_0 while the tail with v_c. From Equation (2.21), in Chapter 2, we observed that the density of the accelerated background plasma increases, by a factor of $\alpha = v_f/(v_f - v_c)$. The pressure balance associated with the magnetopause can then be estimated with

$$\frac{n_0}{1 - v_c/v_f} m_{i,0} v_c^2 \approx \frac{B_{\text{dip}}^2}{8\pi} \ . \tag{3.3}$$

In the simulation scan performed, the position of the magnetopauses varied over time for some of the simulations, due to the formations of waves in the background region that changed the parameters of the background. A similar study to Figure 3.7 was done for Equation (3.3), for the magnetopause locations, in an attempt to validate the model, but due to these fluctuations, this study was inconclusive.

3.7 Conclusions

In this Chapter, we showed the results of PIC simulations of mini magnetospheres in the interaction between a plasma flow and a magnetized background, in a super-Alfvénic regime. We have successfully reproduced the results from recent experiments performed at the LAPD, validating the experimental results and the platform used to study mini magnetospheres in the laboratory.

In the simulations considered, a driver plasma flows against the background plasma magnetized by an internal uniform magnetic field and by a dipole, located in the center of the background. In the early times of the simulations, the effect of dipolar field is small and can neglected, and so, the system behaves similarly to the simulations described in Chapter 2. As previously observed, and during this time, a magnetic cavity with null magnetic field forms in the upstream region, as the driver flows against the background, and as a result, the magnetic field in the background is compressed in the downstream region.

The driver plasma travels through the background until the magnetic field pressure is large enough to counterbalance the driver plasma pressure. When this happen, the driver and part of background plasmas are reflected back upstream. These reflections leads to a quick decompression of the background magnetic field, leading to a reflection of the background magnetic compression.

The interaction of the two plasmas with the dipole results in two different magnetopauses. The first corresponds to the interaction background-dipole, and describes the balance between the kinetic pressure of the propelled background plasma plus the pressure of the plasma internal magnetic field,

and the total magnetic pressure. The second corresponds to the interaction driver-dipole, and describes approximately the balance between the kinetic pressure of the driver plasma separated from the bulk distribution and the relative magnetic pressure. Using the coupling study in Chapter 2, we can calculate these pressure terms, and estimate the positions of the different magnetopauses and standoffs from the pressure balance equations.

We also observed the formation of waves in the background plasma region, where the magnetic field gradient was significant. These waves were not observed in the experiments, and are out of the scope of this Thesis, however, a basic study on these waves suggested that they may be the result slow magnetosonic waves under a dipolar magnetic field.

Chapter 4

Variation of the magnetospheric features with the system parameters

The parameters used for the simulation of the previous chapter were successful in recreating the main features of the experiment, more specifically, the reflection of the magnetic compression and the observation of a magnetopause current structure. In order to identify the ideal conditions for the observation of these features, and to understand the role of the kinetic and magnetic parameters of the system in the results, multiple parameter scans were performed. In this Chapter, the results of these scans are presented.

In Sections 4.1 to 4.3 we discuss how properties of the system, such as the reflection of the magnetic compression and the formation of a magnetopause, vary with the driver parameters, namely its length, density and ion mass. In Section 4.4, the magnetic moment is varied. In Section 4.5, the results for realistic ion mass ratios and thermal velocities are shown to confirm that the simplifications adopted in most simulations, due to computation limitations, do not change the main results. Finally, in Section 4.6, possible effects caused by the finite width and irregular shape of the experimental driver are discussed.

The list of simulations presented in this Chapter are their corresponding parameters are presented in Table B.1 (Appendix B.1).

4.1 Driver length

To find the driver length that best reproduces the experimental results shown in Figure 1.4 and to understand its role on the magnetic field and current density structures, simulations B1 to B3 (see Table B.1 in Appendix B.1) were performed with varying driver length L_x. In Figure 4.1, we show ΔB_z and J_y at $y = 0$, for $L_x = 1\ d_i$ (B1), $L_x = 4\ d_i$ (B2) and for an infinite driver (B3). For these simulations, the properties of the background plasma and the width of the driver L_y were kept unchanged. The density of the driver was $n_d = 2\ n_0$.

In Figures 4.1 a1) and b1), we see the magnetic field and current density plots for the short driver length $L_x = 1\ d_i$. We observe most of the features of Figure 3.3, namely the reflection of the compressed magnetic field in a1) and the diamagnetic and magnetopause currents in b1). For this length, however,

the driver never fully interacts with the dipole. The closest that the diamagnetic current structure gets to the dipole is $x_r \approx -3.0\ d_i$, *i.e.*, much farther than the expected standoff $x_0 = -L_0 = -1.8\ d_i$. To replicate the experimental results and ensure that the driver can reach the dipole, we should thus use a sufficiently long driver such that $x_r > x_0$. Additionally, short drivers risk entering in a decoupling regime between the two plasmas [41], which can compromise the observation of a magnetopause. The coupling effects on the results are discussed in detail in Section 4.2.

The position where the driver is fully reflected by the background can be estimated as $x_r \approx x_B + L_x v_c/(v_0 - v_c)$, where x_B is the initial boundary position between the two plasmas. This estimate is obtained by computing the volume of the background plasma required for the driver plasma to deposit its kinetic energy, *i.e.*, $x_r - x_B$ corresponds to the magnetic stopping radius L_{stop} of the system [66], defined in Chapter 2.

In the simulation with $L_x = 4\ d_i$, represented in Figures 4.1 a2) and b2), we observe once more the main features identified in Figure 3.3, but unlike the $L_x = 1\ d_i$ case, the driver is long enough and ends up reflected by the dipole. We observe that the diamagnetic current reaches the expected standoff and has enough plasma to maintain it near the dipole for a time period ($t\omega_{ci} \approx 3$ to $t\omega_{ci} \approx 5$) longer than the $2\ d_i$ case shown in Figure 3.3. As a result, the magnetic decompression in the background region is delayed for longer drivers. However, because the full driver reflection also occurs later, longer drivers will result in short-lived reflections of the compression of the magnetic field.

In Figures 4.1 a3) and b3), we show the results for a driver with infinite length ($L_x = +\infty$). In this simulation, the driver plasma is only partially initialized inside the simulation domain, and a flow is continuously injected from the lower x boundary. An infinite driver configuration allows us to understand the dynamics of the system in an asymptotic regime in which the driver plasma stays close to the dipole. As expected, until $t\omega_{ci} = 3$, the features observed are very similar to $L_x = 2\ d_i$ and $L_x = 4\ d_i$. After this time, the magnetic and the driver kinetic pressures balance each other near x_0, so the diamagnetic current remains stationary. Because the driver can hold for longer near the dipole, the decompression in the background region is much slower and is not visible for the time range of the plot. We can also observe that the background waves are only visible during a transient.

In all the three simulations C1-3, the coupling velocity measured was always $v_c \approx 0.49\ v_0$. Given the results shown in Figure 4.1, we chose a driver length of $2\ d_i$ to reproduce the experimental results. This driven length is large enough to ensure that the driver arrives at the dipole and small enough to observe a significant reflection of the compression of the magnetic field as we see in the experiments.

4.2 Driver density

As expected from previous works and from the results presented in Chapter 2, increasing the ratio between the driver and background plasma densities should improve the coupling between the two plasmas [29, 41], meaning that, for denser drivers, the transfer of momentum and energy from the driver to the background plasma is more efficient. To better understand the role of the coupling mechanism, we performed simulations with different values of the driver density, namely $n_d = n_0$ (D1), $n_d = 2\,n_0$ (D2) and $n_d = 4\,n_0$ (D3), while keeping a constant background density n_0 and a driver length $L_x = 2\ d_i$. For each

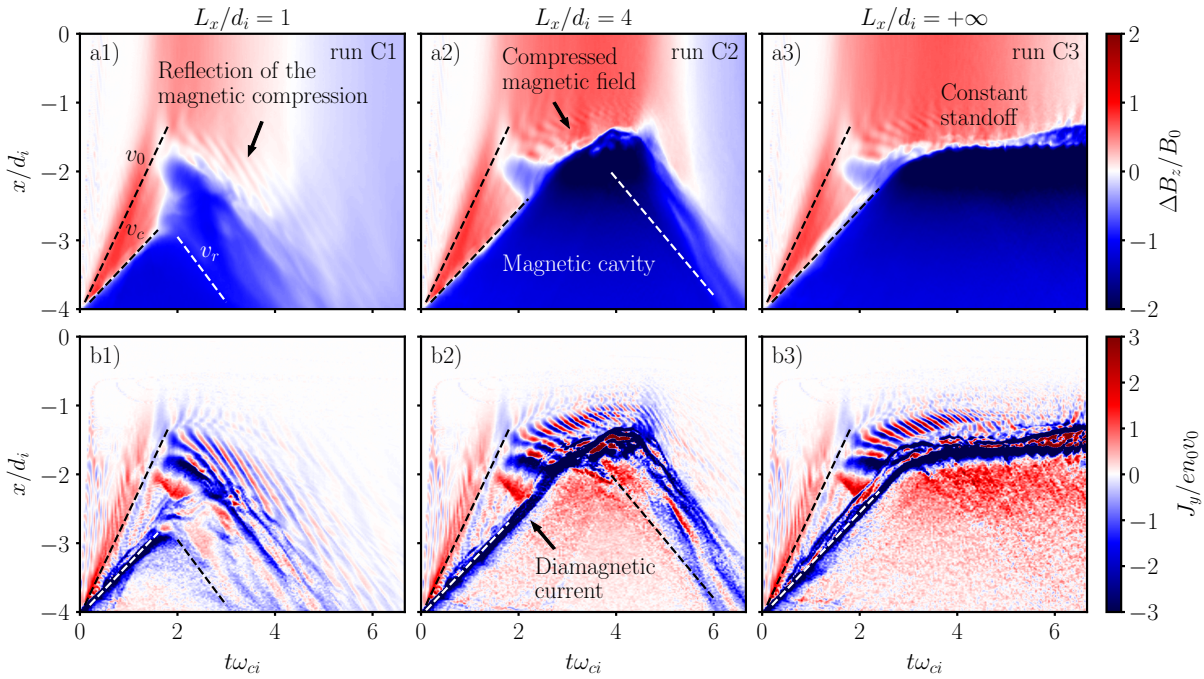

Figure 4.1: Temporal evolution of ΔB_z and J_y at $y = 0$, for driver lengths of a) 1 d_i, b) 4 d_i and for c) an infinite driver length (see Table B.1 for a full list of the parameters). The dashed lines represent the slopes of the flow velocity v_0, the coupling velocity v_c, and the reflection velocity v_r.

run, the magnetic moment was chosen such that the expected standoff obtained from Equation (3.1) was always $L_0 = 1.8\ d_i$. The synthetic magnetic field and current density diagnostics were obtained for these simulations and are shown in Figure 4.2.

In Figures. 4.2 a1) and b1) we can see ΔB_z and J_y for the lowest driver density considered, $n_d = n_0$ (*i.e.*, background and driver with the same initial density). In this regime, the coupling is less efficient and, as a result, the coupling velocity $v_c \approx 0.38\ v_0$ is lower than obtained in the higher densities cases represented in Figures 4.2 b) and c). Due to the low coupling velocity, the driver plasma is reflected more quickly by the background than for denser drivers, and the expected position x_r for the total reflection on the background is farther from the dipole than the expected standoff x_0, meaning $x_r < x_0$. As a result, Figure 4.2 a) shows similarities with the short driver length represented in Figure 4.1 a), because, in both simulations, the driver parameters do not ensure that the driver arrives near the dipole.

In Figures. 4.2 a2) and b2), we show the results for $n_d = 2\ n_0$, which is the same run represented in Figure 3.3. For this density, the coupling velocity, measured as $v_c \approx 0.49\ v_0$, is high enough to ensure a reflection of the driver by the dipole, as we observe at $t\omega_{ci} \approx 3$. In Figures 4.2 a3) and b3) we show the case with the highest driver density $n_d = 4\ n_0$, where the measured coupling velocity was $v_c \approx 0.56\ v_0$, *i.e.*, only slightly larger than the v_c measured for $n_d = 2\ n_0$. In the high density case, we also see that the current density structures during the plasma reflection are filamented, due to analogous multi-stream velocity distributions discussed in Section 4.1 (and shown in Figure 4.1).

To guarantee that the driver reaches the expected standoff, we should thus require that $x_r > x_0$, as argued in Section 4.1. In fact, the position where the driver is reflected x_r, for no dipole cases, increases with the driver length L_x and the velocity ratio v_c/v_0, and thus, both quantities must be large enough to

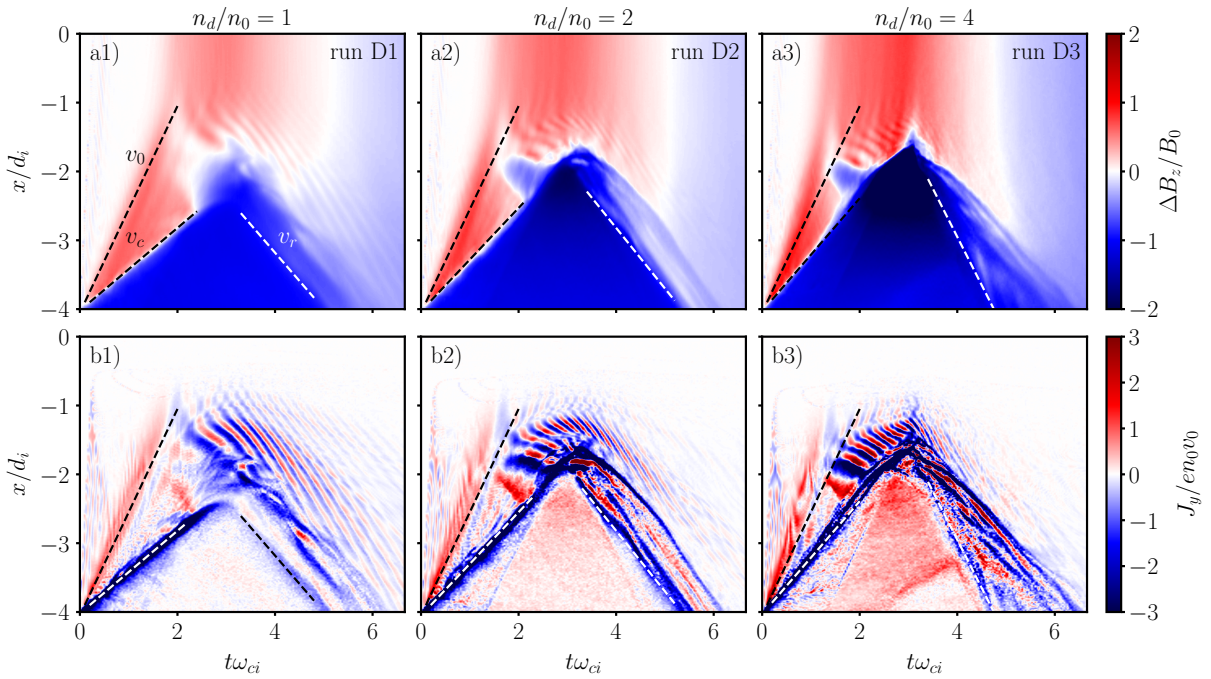

Figure 4.2: Temporal evolution of ΔB_z and J_y at $y = 0$, for different ratios between the driver and background densities n_d/n_0. The magnetic moment was chosen so that the expected standoff distance L_0, calculated from Equation (3.1), was kept as 1.8 d_i for all the simulations. Panels a-c) show results for $n_d = n_0$, $n_d = 2\ n_0$ and $n_d = 4\ n_0$, respectively.

guarantee that $x_r > x_0$. In turn, the ratio v_c/v_0 increases with increasing driver density ratio n_d/n_0 (see Section 2.5 for details), and so, the driver should be sufficiently long and dense to effectively couple to the background plasma. Our results (in particular Section 3.2) show that a driver with $L_x = 2\ d_i$ and $n_d = 2\ n_0$ qualitatively reproduces the experimental results.

4.3 Mass of the driver ions

Motivated by the presence of carbon ions on the experimental drivers, an additional run with heavier driver ions was considered to study how the relative mass ratio between the driver and background ions could change the results. The synthetic magnetic and current diagnostics obtained for the driver ion scan are represented in Figure 4.3. The mass ratios of a) $m_{i,d}/m_{i,0} = 1$, b) $m_{i,d}/m_{i,0} = 3$, and c) $m_{i,d}/m_{i,0} = 5$ were considered. The magnetic moment was adjusted to ensure $L_0 = 1.8\ d_i$.

The typical structures observed in Figure 3.3 can also be observed for the heavier ions simulation, as expected. Figure 3.3 also shows that the reflection of the magnetic compression occurs earlier for the heavier driver ions simulations. These results were also observed in simulations with driver densities larger than those shown in Figure 4.2.

As discussed in Chapter 2, both the velocity of the magnetic compression v_f and the compression ratio α increase with the density and ion mass of the driver. The background decompression occurs earlier for higher v_f and lower α. Because the decompression time is a nonlinear function of the driver mass and density, the reflection of the magnetic compression occurs earlier for some range of values, and then later for higher values. Additionally, we observe in Figures 4.2 and 4.3 that v_r decreases with

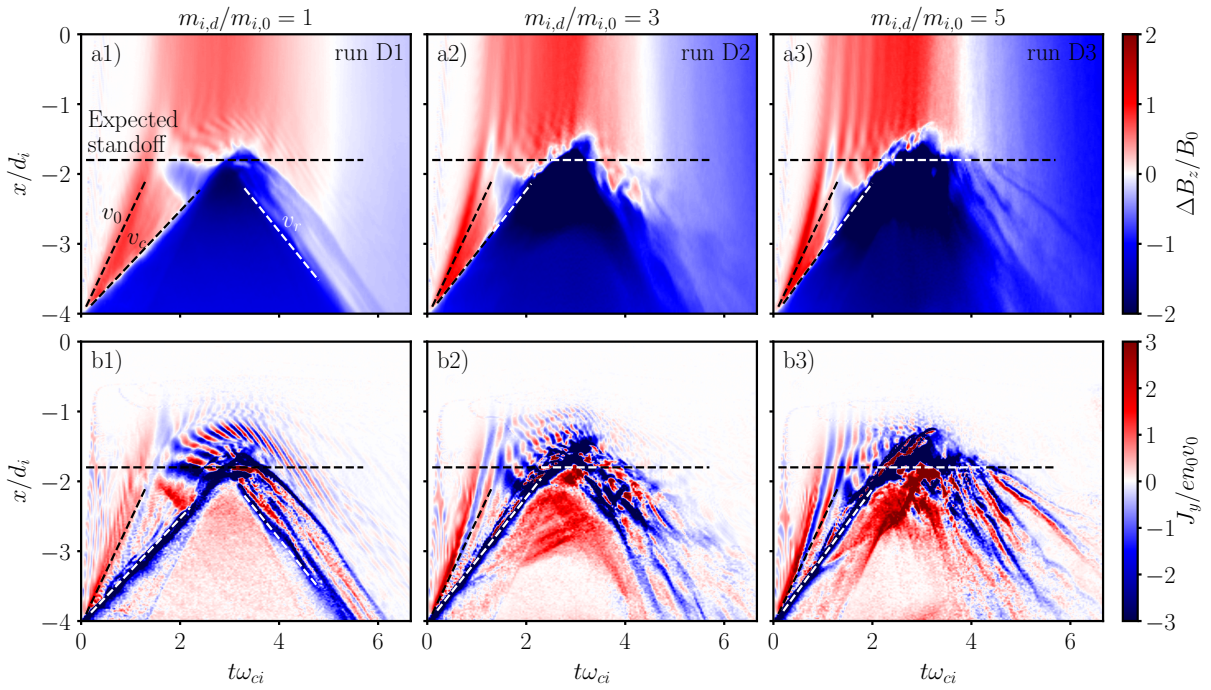

Figure 4.3: Temporal evolution of ΔB_z and J_y at $y = 0$, for different ratios between the driver and background ion masses $m_{i,d}/m_{i,0}$. The magnetic moment was chosen so that the expected standoff distance L_0, calculated from Equation (3.1), was kept as 1.8 d_i for all the simulations. Panels a-c) show results for $m_{i,d} = m_{i,0}$, $m_{i,d} = 3\ m_{i,0}$ and $m_{i,d} = 5\ m_{i,0}$, respectively.

the increase of the density and mass of the driver, leading to faster magnetic decompression.

With these results, we show that the driver length, density and ion masses all affect the observations of the reflection of the magnetic compression feature. However, the driver length is the most relevant parameter, for the simulations considered in this Thesis.

4.4 Magnetic moment of the dipole

To confirm that the features previously associated with the magnetopause location change according with its expected position, we performed simulations with a 2 d_i long driver with density $n_d = 2\ n_0$ for three different magnetic moments. Considering the magnetic moment that results in the expected standoff $L_0 = 1.8\ d_i$ as M_0, simulations with the magnetic moments $2\ M_0$ (E1) and $M_0/2$ (E3) were also performed, corresponding respectively to the expected standoffs $L_0 \approx 2.3\ d_i$ and $L_0 \approx 1.4\ d_i$. Figure 4.4 shows the ΔB_z and J_y synthetic diagnostics at $y = 0$ for the three simulations.

Figures. 4.4 a1) and b1) show the results for the highest magnetic moment $M = 2\ M_0$. We see that the current structures associated with the magnetopause and the background waves are less evident than for the lower magnetic moments, as they are formed farther from the dipole. Figures 4.4 a2) and b2) correspond to the magnetic moment M_0 that leads to $L_0 = 1.8\ d_i$ and are the same results shown in Figure 3.3. As previously mentioned, there are two main observable current structure standoffs. The first one is associated to the diamagnetic current, which is reflected around $t\omega_{ci} \approx 3$ near the expected value $x_0 = -L_0 = -1.8\ d_i$. This standoff is related to the interaction between the driver ions and the dipole. The second standoff occurs between $t\omega_{ci} \approx 2$ and $t\omega_{ci} \approx 3$ and it is located in the background

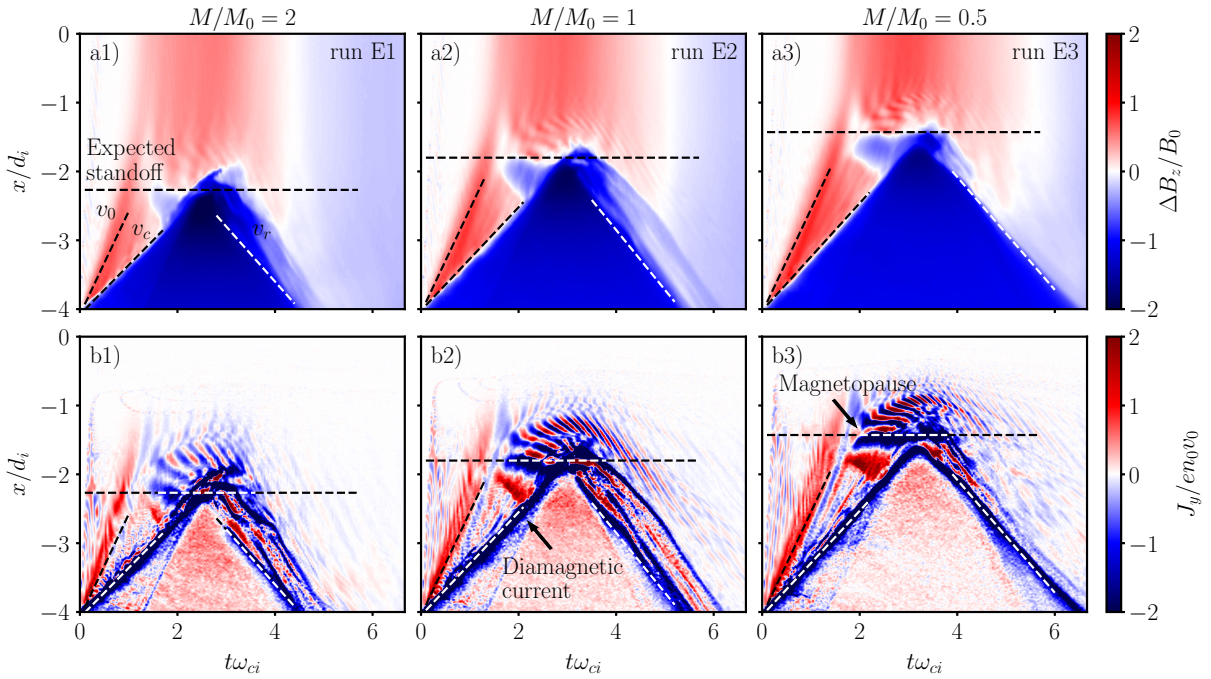

Figure 4.4: Temporal evolution of ΔB_z and J_y at $y = 0$, for three different magnetic moments. The magnetic moments M considered were a) $M = 2\ M_0$, b) $M = M_0$ and c) $M = M_0/2$, where M_0 represents the magnetic moment that corresponds to $L_0 = 1.8\ d_i$ for $n_d = 2\ n_0$. The corresponding standoffs for these simulations are a) $L_0 \approx 2.3\ d_i$, b) $L_0 = 1.8\ d_i$ and c) $L_0 \approx 1.4\ d_i$.

plasma region. This standoff also occurs near $x = -1.8\ d_i$.

In Figures 4.4 a3) and b3), we show the results obtained for the half magnetic moment $M = M_0/2$. In this case, the magnetic pressure exerted by the dipole is lower, leading to a smaller L_0, and consequently, the diamagnetic current feature visible in b3) is closer to the dipole than in Figures 4.4 b1) and b2). The main changes, however, occur in the magnetopause current. Unlike what we observe for the other magnetic moments, the magnetopause current, pinpointed in the current density plot, lasts for a longer time (until $t\omega_{ci} \approx 4$). This current is also more separated from the diamagnetic current standoff and is easier to identify. This is consistent with the experimental observations.

4.5 Realistic parameters

Due to the need for more extensive scans (and thus using physically equivalent but computationally feasible parameters), the simulations shown so far considered reduced ion mass ratios, cold plasmas, and higher velocities than the ones used in the LAPD experiments - see Table B.2. To ensure that the main results presented in the previous sections are also valid with realistic parameters, we have performed a set of simulations with parameters similar to those expected experimentally.

Three simulations were performed, labeled as runs F1 to F3. Run F1 employs realistic mass ratios $m_{i,d}/m_e = m_{i,0}/m_e = 1836$. Additionally, run F2 also considers a ratio between the electron thermal and flow velocities close to the ones expected for the LAPD experiments, namely $v_{the,x}/v_0 = 2.5$ and $v_{thi,x}/v_0 = 0.033$, leading to higher temperatures than in the previous simulations, and thus allowing possible thermal effects on the system. Finally, run F3 considers the same electron thermal velocity

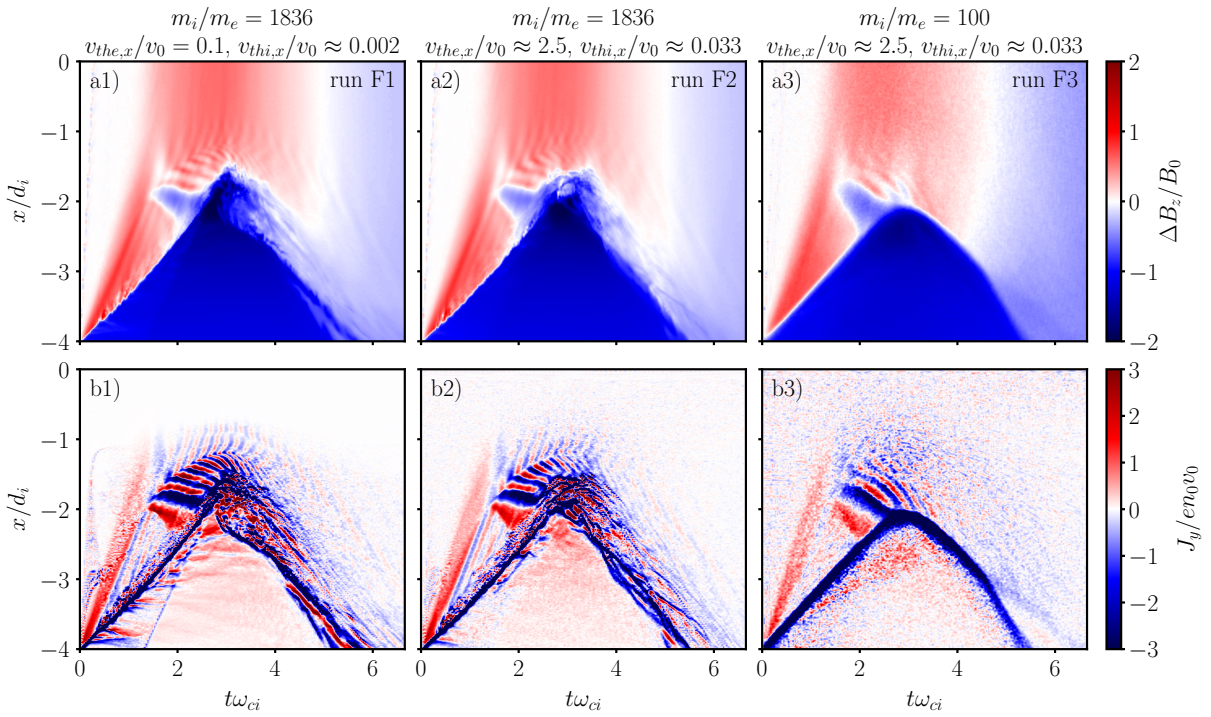

Figure 4.5: Temporal evolution of a) ΔB_z and b) J_y at $y = 0$, for the simulations with similar parameters to the experiments. Run F1 considers realistic mass ratios for the driver and background plasmas and low ratios between the thermal and flow velocities; run F2 uses realistic mass ratios and thermal velocity ratios close to the ones expected in the experiments; run F3 uses the realistic thermal velocity ratios but reduced mass ratios.

ratios of F2 but the standard reduced mass ratios.

The ΔB_z and J_y plots for these simulations are shown in Figure 4.5. Note that, due to changes in m_i/m_e, the spatial and temporal scales were recalculated for the new parameters. Once again, the magnetic dipole moment for the three simulations was adjusted to ensure that $L_0 = 1.8\ d_i$.

As expected, these simulations show the same main structures discussed in the previous sections. We observe the typical reflection of the compression of the magnetic field and the current structures of the magnetopause and diamagnetic cavity. However, some differences are also visible. In Figures 4.5 a1) and b1), *i.e.*, for the realistic mass ratios but cold plasmas simulation, we observe a stronger filamentation of the plasma flow reflected off the dipole and a thinner diamagnetic current. This is because d_e is the characteristic length scale of the current layer and we have lower d_e/d_i values for larger m_i/m_e. Figures 4.5 a2) and b2), for the simulation with higher temperatures, show no major differences with Figures 4.5 a1) and b1), even though there is a significant increase in the thermal velocities.

In Figures 4.5 a3) and b3), however, we observe significant differences for reduced mass ratios with realistic thermal velocity ratios. In particular, we observe in the current density plot smoother magnetic and current structures and less defined background waves between the magnetopause and the dipole. This is expected, since the characteristic plasma scales, e.g. the ion and electron gyroradii, change with the ion to electron thermal velocities and the mass ratios. We also observed for increased ion thermal velocities, for example, $v_{thi}/v_0 \approx 0.25$, that the background waves are no longer visible.

Additionally, other simulations were performed to look for possible changes with realistic parameters.

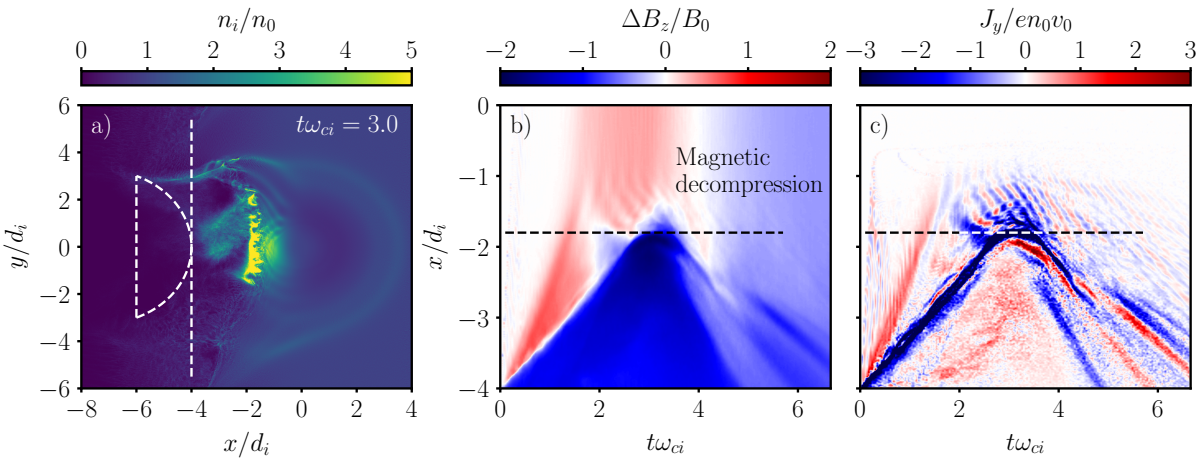

Figure 4.6: a) Total ion density at time $t\omega_{ci} = 3.0$, and temporal evolution of b) ΔB_z and c) J_y at $y = 0$, for simulation G with a finite width driver with a circular segment shape. The dashed lines at a) represent the initial position of the driver and the left border of the background plasma.

A simulation with a lower flow velocity $v_0 = 0.01\ c$ and realistic thermal velocity ratios lead to no significant features observed, and the obtained synthetic diagnostics were very similar to the ones in Figures 4.5 a3) and b3), meaning that the system scales well with v_0. Another simulation was performed to observe if the shape of the initial density profiles of the plasmas would affect the main results. Namely, the constant density profiles used on both the driver and background plasmas were replaced by Gaussian density profiles with a typical gradient scale $\sigma = 1\ d_i$ on the edges of the plasmas. This simulation did not show meaningful differences, in agreement with previous plasma coupling works, which observed that the leading edge of the plasmas evolves similarly for different initial density profiles [67].

4.6 Realistic driver shape

For simplicity, and because we were more interested in studying the system along the axis of symmetry $y = 0$, the previous simulations only considered a driver with infinite width L_y and a length of $L_x = 2\ d_i$. In the experiments, however, the drivers had a width comparable to their lengths and did not have the sharp boundaries used in the simulations. To investigate if and how our results are modified with a more complex-shaped driver, we performed a simulation with a finite width, semi-circular-shaped driver plasma. This driver is initially defined with the conditions $(x + 7.25\ d_i)^2 + y^2 < (3.25\ d_i)^2$ and $x > -6\ d_i$ and has length $L_x = 2\ d_i$ and width $L_y = 6\ d_i$. Figure 4.6 shows the results of this simulation and includes the initial shape of the driver in Figure 4.6 a).

Due to the finite width of the new driver and its particular shape, we should expect to see significant differences in the regions of the simulation plane far from $y = 0$. In the total ion density plot of Figure 4.6 a) for a time $t\omega_{ci} = 3$, when there is a strong interaction of the driver with the dipolar magnetic field, we observe the propagation of waves at the lower and upper sides of the dipole caused by the finite width of the driver, that was not present for infinite width drivers.

In Figures 4.6 b) and c), we see the usual magnetic and current density plots at $y = 0$ for this simulation. By shortening the driver plasma width, the background particles escape from the bottom and top regions of the simulation box, and the driver has more difficulty holding the magnetic decompression

in the background region. The decompression, therefore, occurs quicker for finite drivers, as seen in Figure 4.6 b), leading to short reflections of the magnetic compression.

Although this complex-shaped driver gets us closer to the experimental configuration, the simulations did not include all the properties of the experimental driver, as for example, the non-uniform density, velocity profiles of the plasmas and the flow divergence. Additionally, 3D effects should also be considered. Future simulations are planned to study the effect of these properties in the results. However, we expect that these features will not change the main results of the simulations.

4.7 Conclusions

By performing multiple simulations scans of mini magnetospheres, under different parameters, we were able to understand the necessary conditions for the formation of the structures observed in the LAPD experiments, and understand how the main properties of this system changes with the different parameters.

In most simulations shown in this Chapter, some features are always visible under the different parameter regimes. The formation of a magnetic cavity and the compression of the background magnetic field are also present, and after the reflection of the driver plasma, a fast decompression of the background magnetic field follows. If this background decompression occurs after the total reflection of the driver plasma, located near the dipole, then we also observe the reflection of the compression of the magnetic field.

To ensure that the driver plasma is able to reach the dipolar obstacle, it must have sufficient energy and momentum to push the background close to it. This can be ensured if the driver starts at a distance from the dipole shorter than the magnetic stopping distance, calculated in Chapter 2. Our simulations scans also showed that, if the driver plasma is long enough to ensure that it is able approach the dipole, but short enough to anticipate the driver reflection relative to the background decompression, then a reflection of the magnetic compression in the background region can be observed.

Using simulations with different dipole moments, we have shown that, for lower magnetic moments, the driver and background standoffs are closer to the center of the dipole, and the magnetopause current is more clearly identified than for higher magnetic moments. Furthermore, it is also easier to separate the magnetopause and diamagnetic currents for lower magnetic moments, consistently with experimental observations.

Most of the simulations presented in this work were performed in idealized configurations. In particular, we used reduced ion-to-electron mass ratios, unrealistically high flow velocities, a simple flat-top driver density profile, and neglected thermal effects. In Section. 4.5 and 4.6, we presented simulations that drop some of these simplifications, to test the validity of our simulations. Replacing reduced ion mass ratios with realistic ones and considering high thermal velocities ratios close to the obtained in the experiments did not lead to significant changes in the results. The same occurred when considering smoothed density profiles. It was also possible to conclude that the main features of the system scaled as expected with the absolute value of the driver flow velocity.

Finally, we also presented a simulation to study possible effects associated with the complexity of

the experimental laser-ablated driver. A simple circular segment-shaped driver was considered and led to similar results in the axis of symmetry as the infinite width driver simulations. However, wave-like structures were observed on both the bottom and upper sides of the dipole. For future experiments probing the regions outside the axis of symmetry, a more complex driver shape must be considered in the simulations.

Chapter 5

Conclusions and Future Work

With both numerical and analytical studies, we were able to derive analytical expressions that describe the coupling between a driven-plasma and a magnetized background plasma. We also performed PIC simulations of mini magnetospheres in the interaction between the driven and the magnetized plasmas, and a dipole, in a super-Alfvénic regime. In particular, we have successfully reproduced results from recent experiments performed at the LAPD, validating the experimental platform to study mini magnetospheres in the laboratory. We have also explored an extensive parameter space defining the interaction, allowing us to i) determine how the main properties of the system change with the parameters and ii) identify the required conditions for the magnetospheric features observed the experiments.

Our simulations have shown that some system features are present across multiple regimes. The initial flow of the driver expels the magnetic field in the upstream region, leading to a magnetic cavity, and compresses the downstream magnetic field. We have studied this interaction analytically and numerically, resorting to PIC simulations. For Mach numbers close to unity, we calculated the velocities of the magnetic cavity and magnetic compression, and the magnetic field compression ratio. For higher Mach numbers, instabilities are triggered during the interaction, which change the system energy partition, invalidating our model.

For the flows considered, the driver particles are reflected upstream during the interaction with the background plasma and the magnetic field, by an electric field. This reflection continues until the driver plasma is totally reflected. We have derived coupling equations that allow us to determine the maximum distance that the magnetic cavity can travel through the background. The equations were were consistent with numerical results. During the reflection, the background ions are accelerated and pushed forward, leading to the formation of the slow and fast magnetosonic waves and other instabilities in the plasmas.

When a magnetic dipole is placed in front of the flow, the driver travels through the background until the magnetic pressure is large enough to counterbalance the driver kinetic pressure, leading to the formation of mini magnetospheres. A fast decompression of the background magnetic field then follows. If the background decompression occurs after the total reflection of the driver plasma, then we can observe the reflection of the magnetic field compression. Resorting to simulations across a wide range

of parameters, we have shown that, in order to see this feature, the driver needs to be short enough to anticipate the driver reflection relative to the decompression but sufficiently long to ensure that it can get close to the dipole.

The interaction of the plasmas with the dipole results in two magnetopauses. The first occurs where there is a balance between the kinetic pressure of the propelled background plasma plus the pressure of the plasma internal magnetic field and the total magnetic pressure. The second occurs where there is a balance between the kinetic pressure of the driver plasma separated from the bulk distribution and the relative magnetic pressure. Using simulations with different dipole moments, we have shown that the magnetopause current is more clearly identified and easier to separate from the diamagnetic current, for lower magnetic moments, consistent with experimental observations.

In these simulations, we also observed the formation of waves in the background plasma region, between the magnetopause and the center of the dipole, where the magnetic field gradient was significant. These waves result from the excitation that always followed the formation of the magnetopause and were only observed for background plasmas with relative low ion thermal velocities. These waves are out of the scope of the Thesis, but a preliminary study suggested that they are the result of magnetosonic waves under a dipolar magnetic field.

Most simulations presented in the coupling and mini magnetospheres studies were performed in idealized configurations of the laboratory system. In particular, we used reduced ion-to-electron mass ratios, unrealistically high flow velocities, a simple flat-top driver density profile, and neglected thermal effects. With more realistic simulations, we showed that these simplifications do not lead to significant changes in the results, and we can use these simplifications to model the laboratory systems.

In conclusion, the simulations were consistent with the LAPD experimental results, and the multiple parameter scans performed dictated the formation conditions of the main features of mini magnetospheres. Analytical expressions derived for the energy and momentum transfers between the driven-plasma and the magnetized plasma were also successful in describing the evolution of these systems for certain ranges of parameters.

In the future, we plan to reform the coupling expressions for high Mach numbers, by considering instabilities into the energy terms, and explore other regimes and configurations, such as higher ion and electron temperatures, and different driver ion charges. This would extend the range of scenarios that the coupling study would cover, and assist in the design of future experiments with driven-plasmas and magnetized backgrounds. For the mini magnetosphere project, we intend to exploit sub-Alfvénic mini magnetospheres simulations, exploit anti-parallel magnetic field configurations, perform 3D simulations, study the formation of bow shocks in laboratory, and consider even more realistic properties of the driver. These studies would help us better understand laboratory mini magnetospheres and explore important phenomena, such as reconnection and the formation of a bow shock.

Bibliography

[1] L. F. Burlaga, R. M. Skoug, C. W. Smith, D. F. Webb, T. H. Zurbuchen, and A. Reinard. Fast ejecta during the ascending phase of solar cycle 23: ACE observations, 1998-1999. *Journal of Geophysical Research: Space Physics*, 106(A10):20957–20977, 2001.

[2] D. S. Spicer, R. W. Clark, S. P. Maran, and R. W. Clark. A Model of the Pre-Sedov Expansion Phase of Supernova Remnant–Ambient Plasma Coupling and X-Ray Emission from SN 1987A. *Astrophysical Journal; (USA)*, 356:549, 1990.

[3] S. M. Krimigis, G. Haerendel, R. W. McEntire, G. Paschmann, and D. A. Bryant. The active magnetospheric particle tracer explorers (AMPTE) program. *Eos, Transactions American Geophysical Union*, 63(45):843–850, 1982.

[4] C. Russell. The Magnetosphere. *Annual Review of Earth and Planetary Sciences*, 19(1):169–182, 1991.

[5] C. P. Escoubet, A. Pedersen, R. Schmidt, and P. A. Lindqvist. Density in the magnetosphere inferred from isee 1 spacecraft potential. *Journal of Geophysical Research: Space Physics*, 102 (A8):17595–17609, 1997. doi: https://doi.org/10.1029/97JA00290.

[6] P. Brady, T. Ditmire, W. Horton, M. L. Mays, and Y. Zakharov. Laboratory experiments simulating solar wind driven magnetospheres. *Physics of Plasmas*, 16(4), 2009.

[7] C. C. Finlay, S. Maus, C. D. Beggan, T. N. Bondar, A. Chambodut, T. A. Chernova, A. Chulliat, V. P. Golovkov, B. Hamilton, M. Hamoudi, R. Holme, G. Hulot, W. Kuang, B. Langlais, V. Lesur, F. J. Lowes, H. Lühr, S. MacMillan, M. Mandea, S. McLean, C. Manoj, M. Menvielle, I. Michaelis, N. Olsen, J. Rauberg, M. Rother, T. J. Sabaka, A. Tangborn, L. Tøffner-Clausen, E. Thébault, A. W. P. Thomson, I. Wardinski, Z. Wei, and T. I. Zvereva. International Geomagnetic Reference Field: the eleventh generation. *Geophysical Journal International*, 183(3):1216–1230, 2010.

[8] F. Cruz. Collisionless shocks in mini magnetospheres in the laboratory and in astrophysics. Master's thesis, Instituto Superior Técnico, 2015.

[9] R. P. Lin, D. L. Mitchell, D. W. Curtis, K. A. Anderson, C. W. Carlson, J. McFadden, M. H. Acuña, L. L. Hood, and A. Binder. Lunar surface magnetic fields and their interaction with the solar wind: Results from lunar prospector. *Science*, 281(5382):1480–1484, 1998.

[10] J. S. Halekas, G. T. Delory, D. A. Brain, R. P. Lin, and D. L. Mitchell. Density cavity observed over a strong lunar crustal magnetic anomaly in the solar wind: A mini-magnetosphere? *Planetary and Space Science*, 56(7):941–946, 2008.

[11] M. Kato, S. Sasaki, and Y. Takizawa. The Kaguya Mission Overview. *Space Sci Rev*, 154:3–19, 2010.

[12] M. Wieser, S. Barabash, Y. Futaana, M. Holmström, A. Bhardwaj, R. Sridharan, M. B. Dhanya, A. Schaufelberger, P. Wurz, and K. Asamura. First observation of a mini-magnetosphere above a lunar magnetic anomaly using energetic neutral atoms. *Geophysical Research Letters*, 37(5):1–4, 2010.

[13] G. Kramer, J. Deca, S. Shukla, T. Kohout, X. Wang, and R. Watkins. The Plethora of Science Afforded by a Lunar Swirl. *Bulletin of the AAS*, 53, 2021.

[14] R. A. Bamford, B. Kellett, W. J. Bradford, C. Norberg, A. Thornton, K. J. Gibson, I. A. Crawford, L. Silva, L. Gargaté, and R. Bingham. Minimagnetospheres above the Lunar Surface and the Formation of Lunar Swirls. *Physical Review Letters*, 109(8):081101, 2012.

[15] R. J. Lillis, S. Robbins, M. Manga, J. S. Halekas, and H. V. Frey. Time history of the Martian dynamo from crater magnetic field analysis. *Journal of Geophysical Research E: Planets*, 118(7): 1488–1511, 2013.

[16] B. J. Anderson, C. L. Johnson, H. Korth, M. E. Purucker, R. M. Winslow, J. A. Slavin, S. C. Solomon, R. L. McNutt, J. M. Raines, and T. H. Zurbuchen. The Global Magnetic Field of Mercury from MESSENGER Orbital Observations. *Science*, 333(6051):1859–1862, 2011.

[17] M. G. Kivelson, K. K. Khurana, F. V. Coroniti, S. Joy, C. T. Russell, R. J. Walker, J. Warnecke, L. Bennett, and C. Polanskey. The magnetic field and magnetosphere of Ganymede. *Geophysical Research Letters*, 24(17):2155–2158, 1997.

[18] C. T. Russell, J. L. Phillips, M. R. Arghavani, J. D. Mihalov, W. C. Knudsen, and K. Miller. A possible observation of a cometary bow shock. *Geophysical Research Letters*, 11(10):1022–1025, 1984.

[19] R. A. Bamford, B. Kellett, J. Bradford, T. N. Todd, M. G. Benton, R. Stafford-Allen, E. P. Alves, L. Silva, C. Collingwood, I. A. Crawford, and R. Bingham. An exploration of the effectiveness of artificial mini-magnetospheres as a potential solar storm shelter for long term human space missions. *Acta Astronautica*, 105(2):385–394, 2014.

[20] J. Adams Jr, D. Hathaway, R. Grugel, J. Watts, T. Parnell, J. Gregory, and R. Winglee. Revolutionary concepts of radiation shielding for human exploration of space. Technical report, 2005.

[21] R. M. Winglee, J. Slough, T. Ziemba, and A. Goodson. Mini-magnetospheric plasma propulsion: Tapping the energy of the solar wind for spacecraft propulsion. *Journal of Geophysical Research: Space Physics*, 105(A9):21067–21077, 2000.

[22] R. Bamford, K. J. Gibson, A. J. Thornton, J. Bradford, R. Bingham, L. Gargate, L. O. Silva, R. A. Fonseca, M. Hapgood, C. Norberg, T. Todd, and R. Stamper. The interaction of a flowing plasma with a dipole magnetic field: Measurements and modelling of a diamagnetic cavity relevant to spacecraft protection. *Plasma Physics and Controlled Fusion*, 50(12), 2008.

[23] D. B. Schaeffer, D. Winske, D. J. Larson, M. M. Cowee, C. G. Constantin, A. S. Bondarenko, S. E. Clark, and C. Niemann. On the generation of magnetized collisionless shocks in the large plasma device. *Physics of Plasmas*, 24(4):041405, 2017. doi: 10.1063/1.4978882.

[24] A. Rigby, F. Cruz, B. Albertazzi, R. Bamford, A. R. Bell, J. E. Cross, F. Fraschetti, P. Graham, Y. Hara, P. M. Kozlowski, Y. Kuramitsu, D. Q. Lamb, S. Lebedev, J. R. Marques, F. Miniati, T. Morita, M. Oliver, B. Reville, Y. Sakawa, S. Sarkar, C. Spindloe, R. Trines, P. Tzeferacos, L. O. Silva, R. Bingham, M. Koenig, and G. Gregori. Electron acceleration by wave turbulence in a magnetized plasma. *Nature Physics*, 14(5):475–479, 2018.

[25] E. T. Kennedy. Plasmas and intense laser light. *Contemporary Physics*, 25(1):31–58, 1984.

[26] S. Amoruso, R. Bruzzese, N. Spinelli, and R. Velotta. Characterization of laser-ablation plasmas. *Journal of Physics B: Atomic, Molecular and Optical Physics*, 32:R131, 1999.

[27] D. B. Schaeffer, A. S. Bondarenko, E. T. Everson, S. E. Clark, C. G. Constantin, and C. Niemann. Characterization of laser-produced carbon plasmas relevant to laboratory astrophysics. *Journal of Applied Physics*, 120(4):043301, 2016. doi: 10.1063/1.4959148.

[28] C. Niemann, W. Gekelman, C. G. Constantin, E. T. Everson, D. B. Schaeffer, A. S. Bondarenko, S. E. Clark, D. Winske, S. Vincena, B. Van Compernolle, and P. Pribyl. Observation of collisionless shocks in a large current-free laboratory plasma. *Geophysical Research Letters*, 41(21):7413–7418, 2014.

[29] A. S. Bondarenko, D. B. Schaeffer, E. T. Everson, S. E. Clark, B. R. Lee, C. G. Constantin, S. Vincena, B. Van Compernolle, S. K. Tripathi, D. Winske, and C. Niemann. Collisionless momentum transfer in space and astrophysical explosions. *Nature Physics*, 13(6):573–576, 2017.

[30] A. Bondarenko. *Collision-less Coupling between Explosive Debris Plasma and Magnetized Ambient Plasma*. PhD thesis, University of California, Los Angeles, 2015.

[31] B. H. Ripin, J. D. Huba, E. A. McLean, C. K. Manka, T. Peyser, H. R. Burris, and J. Grun. Sub-alfvénic plasma expansion. *Physics of Fluids B: Plasma Physics*, 5(10):3491–3506, 1993. doi: 10.1063/1.860825.

[32] D. B. Schaeffer, E. T. Everson, A. S. Bondarenko, S. E. Clark, C. G. Constantin, D. Winske, W. Gekelman, and C. Niemann. Experimental study of subcritical laboratory magnetized collisionless shocks using a laser-driven magnetic piston. *Physics of Plasmas*, 22(11):113101, 2015. doi: 10.1063/1.4934983.

[33] C. Niemann, W. Gekelman, C. G. Constantin, E. T. Everson, D. B. Schaeffer, S. E. Clark, D. Winske, A. B. Zylstra, P. Pribyl, S. K. P. Tripathi, D. Larson, S. H. Glenzer, and A. S. Bondarenko. Dynamics of exploding plasmas in a large magnetized plasma. *Physics of Plasmas*, 20(1):012108, 2013. doi: 10.1063/1.4773911.

[34] E. T. Everson. *Magnetic Field Characterization of a Diamagnetic Cavity Piston for Generation of Quasi-Perpendicular Collisionless Shocks*. PhD thesis, University of California, Los Angeles, 2016.

[35] J. D. Bonde. *Collisionless Energy and Momentum Coupling of a High-Beta Expansion to an Ambient Plasma*. PhD thesis, University of California, Los Angeles, 2016.

[36] R. M. Winglee, T. Ziemba, P. Euripides, and J. Slough. Magnetic inflation produced by the Mini-Magnetospheric Plasma Propulsion (M2P2) prototype. *AIP Conference Proceedings*, 433(March 2002):433–440, 2007.

[37] I. F. Shaikhislamov, V. M. Antonov, Y. P. Zakharov, E. L. Boyarintsev, A. V. Melekhov, V. G. Posukh, and A. G. Ponomarenko. Mini-magnetosphere: Laboratory experiment, physical model and Hall MHD simulation. *Advances in Space Research*, 52(3):422–436, 2013.

[38] I. F. Shaikhislamov, Y. P. Zakharov, V. G. Posukh, A. V. Melekhov, V. M. Antonov, E. L. Boyarintsev, and A. G. Ponomarenko. Experimental study of a mini-magnetosphere. *Plasma Physics and Controlled Fusion*, 56(2), 2014.

[39] D. B. Schaeffer, F. D. Cruz, R. S. Dorst, F. Cruz, P. V. Heuer, C. G. Constantin, P. Pribyl, C. Niemann, L. O. Silva, and A. Bhattacharjee. Laser-driven, ion-scale magnetospheres in laboratory plasmas. i. experimental platform and first results. *Physics of Plasmas*, 29(4):042901, 2022.

[40] D. D. Ryutov and B. A. Remington. Scaling astrophysical phenomena to high-energy-density laboratory experiments. *Plasma Physics and Controlled Fusion*, 44(12B):B407—-B423, 2002.

[41] D. W. Hewett, S. H. Brecht, and D. J. Larson. The physics of ion decoupling in magnetized plasma expansions. *J. Geophys. Res*, 116:11310, 2011.

[42] D. Winske, J. D. Huba, C. Niemann, and A. Le. Recalling and updating research on diamagnetic cavities: Experiments, theory, simulations. *Frontiers in Astronomy and Space Sciences*, 5, 2019. doi: 10.3389/fspas.2018.00051.

[43] M. VanZeeland and W. Gekelman. Laser-plasma diamagnetism in the presence of an ambient magnetized plasma. *Physics of Plasmas*, 11(1):320–323, 2004. doi: 10.1063/1.1628233.

[44] A. Le, D. Winske, A. Stanier, W. Daughton, M. Cowee, B. Wetherton, and F. Guo. Astrophysical explosions revisited: Collisionless coupling of debris to magnetized plasma. *Journal of Geophysical Research: Space Physics*, 126(9):e2021JA029125, 2021. doi: https://doi.org/10.1029/2021JA029125.

[45] N. Behera, A. Kumar, and R. K. Singh. Cavitation and charge separation in laser-produced copper and carbon plasma in transverse magnetic field. *Plasma Research Express*, 3(2):025011, 2021. doi: 10.1088/2516-1067/ac0580.

[46] S. E. Clark, D. Winske, D. B. Schaeffer, E. T. Everson, A. S. Bondarenko, C. G. Constantin, and C. Niemann. Hybrid simulation of shock formation for super-alfvénic expansion of laser ablated debris through an ambient, magnetized plasma. *Physics of Plasmas*, 20(8):082129, 2013. doi: 10.1063/1.4819251.

[47] S. E. Clark, E. T. Everson, D. B. Schaeffer, A. S. Bondarenko, C. G. Constantin, C. Niemann, and D. Winske. Enhanced collisionless shock formation in a magnetized plasma containing a density gradient. *Phys. Rev. E*, 90:041101, 2014. doi: 10.1103/PhysRevE.90.041101.

[48] F. D. Cruz, D. B. Schaeffer, F. Cruz, and L. O. Silva. Laser-driven, ion-scale magnetospheres in laboratory plasmas. ii. particle-in-cell simulations. *Physics of Plasmas*, 29(3):032902, 2022. doi: 10.1063/5.0084354.

[49] E. M. Harnett and R. Winglee. Two-dimensional MHD simulation of the solar wind interaction with magnetic field anomalies on the surface of the Moon. *Journal of Geophysical Research: Space Physics*, 105(A11):24997–25007, 2000.

[50] E. M. Harnett and R. M. Winglee. 2.5D Particle and MHD simulations of mini-magnetospheres at the Moon. *Journal of Geophysical Research: Space Physics*, 107(A12):1–16, 2002.

[51] X. Blanco-Cano, N. Omidi, and C. T. Russel. How to make a magnetosphere. *Astronomy & Geophysics*, 45(3):3.14–3.17, 2004.

[52] L. Gargaté, R. Bingham, R. A. Fonseca, R. Bamford, A. Thornton, K. Gibson, J. Bradford, and L. O. Silva. Hybrid simulations of mini-magnetospheres in the laboratory. *Plasma Physics and Controlled Fusion*, 50(7):1–12, 2008.

[53] C. K. Birdsall and A. B. Langdon. *Plasma physics via computer simulation*. Series in plasma physics. Taylor & Francis, New York, 2005. ISBN 9780750310251.

[54] J. Deca, A. Divin, G. Lapenta, B. Lembège, S. Markidis, and M. Horányi. Electromagnetic Particle-in-Cell Simulations of the Solar Wind Interaction with Lunar Magnetic Anomalies. *Physical Review Letters*, 112(15):151102, 2014.

[55] J. Deca, A. Divin, B. Lembège, M. Horányi, S. Markidis, and G. Lapenta. General mechanism and dynamics of the solar wind interaction with lunar magnetic anomalies from 3-D particle-in-cell simulations. *Journal of Geophysical Research: Space Physics*, 120(8):6443–6463, 2015.

[56] R. A. Bamford, E. P. Alves, F. Cruz, B. J. Kellett, R. A. Fonseca, L. O. Silva, R. M. G. M. Trines, J. S. Halekas, G. Kramer, E. Harnett, R. A. Cairns, and R. Bingham. 3D Pic Simulations of Collisionless Shocks At Lunar Magnetic Anomalies and Their Role in Forming Lunar Swirls. *The Astrophysical Journal*, 830(2):146, 2016.

[57] E. Kallio, R. Jarvinen, S. Dyadechkin, P. Wurz, S. Barabash, F. Alvarez, V. A. Fernandes, Y. Futaana, A. M. Harri, J. Heilimo, C. Lue, J. Mäkelä, N. Porjo, W. Schmidt, and T. Siili. Kinetic simulations of finite gyroradius effects in the lunar plasma environment on global, meso, and microscales. *Planetary and Space Science*, 74(1):146–155, 2012.

[58] M. I. Zimmerman, W. M. Farrell, and A. R. Poppe. Kinetic simulations of kilometer-scale mini-magnetosphere formation on the Moon. *Journal of Geophysical Research: Planets*, 120(11):1893–1903, 2015.

[59] F. Cruz, E. P. Alves, R. A. Bamford, R. Bingham, R. A. Fonseca, and L. O. Silva. Formation of collisionless shocks in magnetized plasma interaction with kinetic-scale obstacles. *Physics of Plasmas*, 24(2):022901, 2017.

[60] J. Deca, A. R. Poppe, A. Divin, and B. Lembège. The Plasma Environment Surrounding the Reiner Gamma Magnetic Anomaly. *Journal of Geophysical Research: Space Physics*, 126(9): e2021JA029180, 2021.

[61] R. A. Fonseca, L. O. Silva, F. S. Tsung, V. K. Decyk, W. Lu, C. Ren, W. B. Mori, S. Deng, S. Lee, T. Katsouleas, and J. C. Adam. OSIRIS: A three-dimensional, fully relativistic particle in cell code for modeling plasma based accelerators. In *Lecture Notes in Computer Science (including subseries Lecture Notes in Artificial Intelligence and Lecture Notes in Bioinformatics)*, volume 2331 LNCS, pages 342–351. Springer Verlag, 2002.

[62] R. A. Fonseca, J. Vieira, F. Fiuza, A. Davidson, F. S. Tsung, W. B. Mori, and L. O. Silva. Exploiting multi-scale parallelism for large scale numerical modelling of laser wakefield accelerators. *Plasma Physics and Controlled Fusion*, 55(12), 2013.

[63] D. B. Schaeffer, E. T. Everson, A. S. Bondarenko, S. E. Clark, C. G. Constantin, D. Winske, W. Gekelman, and C. Niemann. Experimental study of subcritical laboratory magnetized collisionless shocks using a laser-driven magnetic piston. *Physics of Plasmas*, 22(11):113101, 2015.

[64] A. Balogh and R. A. Treumann. *Physics of collisionless shocks: space plasma shock waves*. Springer Science & Business Media, 2013.

[65] R. L. Liboff. *Kinetic Theory: Classical, Quantum, and Relativistic Descriptions*. Graduate Texts in Contemporary Physics. Springer New York, 2003.

[66] B. H. Ripin, J. D. Huba, E. A. McLean, C. K. Manka, T. Peyser, H. R. Burris, and J. Grun. Sub-alfvénic plasma expansion. *Physics of Fluids B: Plasma Physics*, 5(10):3491–3506, 1993.

[67] R. W. Clark, J. Denavit, and K. Papadopoulos. Laminar interactions in high Mach number plasma flows. *The Physics of Fluids*, 16(7):1097–1101, 1973.

[68] Y. Saito, M. N. Nishino, M. Fujimoto, T. Yamamoto, S. Yokota, H. Tsunakawa, H. Shibuya, M. Matsushima, H. Shimizu, and F. Takahashi. Simultaneous observation of the electron acceleration and

ion deceleration over lunar magnetic anomalies. *Earth, Planets and Space*, 64(2):4, 2012. doi: 10.5047/eps.2011.07.011.

[69] D. B. Schaeffer, A. S. Bondarenko, E. T. Everson, S. E. Clark, C. G. Constantin, and C. Niemann. Characterization of laser-produced carbon plasmas relevant to laboratory astrophysics. *Journal of Applied Physics*, 120(4):043301, 2016. doi: 10.1063/1.4959148.

Appendix A

Derivation of the coupling equations

A.1 Main interaction

Chapter 2 studies the coupling between a driver plasma with density n_d, ion mass $m_{d,i}$, and length L_d, flowing with fluid velocity v_0 against a magnetized background plasma with density n_0, ion mass $m_{0,i}$, and uniform magnetic field B_0. We observed that the system forms a magnetic cavity, of null magnetic field that travels through the background with coupling velocity v_c, while the magnetic background field is compressed by a ratio α that travels with front velocity v_f.

In Chapter 2, we observed that we could relate the coupling parameters v_c, v_f and α with the initial parameters of the system, by the energy conservation equation

$$\Delta E_\mathsf{d} + \Delta E_0 + \Delta E_\mathsf{mag} + \Delta E_\mathsf{ele} = 0 \ , \tag{A.1}$$

where ΔE_d is the energy variation of the driver plasma, ΔE_0 of the background plasma, ΔE_mag of magnetic energy, and ΔE_ele of electric energy. In Section 2.4, we showed that these energies could be estimated for an area transverse to the flow A_T and a time duration Δt by the expressions

$$\Delta E_\mathsf{d} = -2 n_{d,0} m_{i,d} (v_0 - v_c)^2 v_c A_T \Delta t \tag{A.2}$$

$$\Delta E_0 = \frac{1}{2} m_{i,0} v_c^2 n_0 v_f A_T \Delta t \tag{A.3}$$

$$\Delta E_\mathsf{mag} = \frac{B_0^2}{2} \left[\alpha^2 (v_f - v_c) - v_f \right] A_T \Delta t \ . \tag{A.4}$$

The electric energy E_ele can be neglected. Equation (A.1) becomes

$$
\begin{aligned}
& -2n_{d,0}m_{i,d}(v_0-v_c)^2v_c+\frac{1}{2}m_{i,0}v_c^2n_0v_f+\frac{B_0^2}{8\pi}\left[\alpha^2(v_f-v_c)-v_f\right]=0 \\
\iff & \frac{-2n_{d,0}m_{i,d}}{n_0m_{i,0}}\frac{v_c}{v_0}\left(1-\frac{v_c}{v_0}\right)^2+\frac{1}{2}\frac{v_f}{v_0}\left(\frac{v_c}{v_0}\right)^2+\frac{B_0^2}{8\pi n_0m_{i,0}v_0^2}\left[\alpha^2\left(\frac{v_f}{v_0}-\frac{v_c}{v_0}\right)-\frac{v_f}{v_0}\right]=0 \\
\iff & -\frac{1}{R_n^2}\frac{v_c}{v_0}\left(1-\frac{v_c}{v_0}\right)^2+\frac{v_f}{v_0}\left(\frac{v_c}{v_0}\right)^2+\frac{1}{M_A^2}\left[\alpha^2\left(\frac{v_f}{v_0}-\frac{v_c}{v_0}\right)-\frac{v_f}{v_0}\right]=0\,. \qquad \text{(A.5)}
\end{aligned}
$$

where the initial Alfvénic Mach number M_A and the ratio R_n are defined by

$$
M_A\equiv\frac{v_0}{v_A}=\frac{\sqrt{4\pi n_0m_{i,0}v_0^2}}{B_0} \qquad \text{(A.6)}
$$

$$
R_n\equiv\frac{1}{2}\left(\frac{n_0}{n_{d,0}}\frac{m_{i,0}}{m_{i,d}}\right)^{\frac{1}{2}}\,. \qquad \text{(A.7)}
$$

From Section 2.3.4, we also saw that the Rankine-Hugoniot equations lead to

$$
\alpha=\frac{v_f}{v_f-v_c}\iff\frac{v_f}{v_0}=\frac{\alpha}{\alpha-1}\frac{v_c}{v_0}\,. \qquad \text{(A.8)}
$$

By applying Equation (A.8) to replace v_f/v_0 in Equation (A.5), we obtain

$$
\begin{aligned}
& -\frac{1}{R_n^2}\frac{v_c}{v_0}\left(1-\frac{v_c}{v_0}\right)^2+\frac{\alpha}{\alpha-1}\left(\frac{v_c}{v_0}\right)^3+\frac{2}{M_A^2}\frac{v_c}{v_0}\left[\alpha^2\left(\frac{\alpha}{\alpha-1}-1\right)-\frac{\alpha}{\alpha-1}\right]=0 \\
\iff & -\frac{\alpha-1}{R_n^2}\left(1-\frac{v_c}{v_0}\right)^2+\alpha\left(\frac{v_c}{v_0}\right)^2+\frac{2\alpha(\alpha-1)}{M_A^2}=0 \\
\iff & -(\alpha-1)M_A^2\left(1-\frac{v_c}{v_0}\right)^2+\alpha M_A^2R_n^2\left(\frac{v_c}{v_0}\right)^2+\alpha(\alpha-1)R_n^2=0\,. \qquad \text{(A.9)}
\end{aligned}
$$

From the pressure balance in the interface between the driver and background plasmas, discussed in Section 2.2, we also observed that

$$
\begin{aligned}
& 2n_dm_{i,d}(v_0-v_c)^2=\frac{(\alpha B_0)^2}{8\pi} \\
\iff & \frac{2n_dm_{i,d}}{n_0m_{i,0}}\left(1-\frac{v_c}{v_0}\right)^2=\frac{(\alpha B_0)^2}{8\pi n_0m_{i,0}v_0^2} \\
\iff & \frac{1}{R_n^2}\left(1-\frac{v_c}{v_0}\right)^2=\frac{\alpha^2}{M_A^2}\,. \qquad \text{(A.10)}
\end{aligned}
$$

Replacing v_c/v_0 in Equation (A.9) with Equation (A.10), and considering that $v_c<v_0$ and $\alpha>0$, we obtain

$$
\begin{aligned}
&-(\alpha-1)\alpha^2 R_n^2 + \alpha M_A^2 R_n^2 \left(1 - \frac{\alpha R_n}{M_A}\right)^2 + \alpha(\alpha-1)R_n^2 = 0 \\
\iff &-(\alpha-1)\alpha R_n^2 + R_n^2 \left(M_A - \alpha R_n\right)^2 + (\alpha-1)R_n^2 = 0 \\
\iff &\alpha^2\left(R_n^2-1\right) + 2\alpha\left(1 - R_n M_A\right) + \left(M_A^2 - 1\right) = 0\,.
\end{aligned}
$$

Equation (A.11) results in two possible solutions for α

$$
\begin{aligned}
\alpha &= \frac{-1 + R_n M_A \pm \sqrt{(1-R_n M_A)^2 - (R_n^2-1)(M_A^2-1)}}{R_n^2 - 1} \\
&= \frac{-1 + R_n M_A \pm (R_n - M_A)}{R_n^2 - 1}\,,
\end{aligned}
$$

which leads to the analytical expressions for the parameter α

$$
\alpha_1 = \frac{1 + M_A}{1 + R_n} \qquad \wedge \qquad \alpha_2 = \frac{M_A - 1}{1 + R_n}\,. \tag{A.11}
$$

With these two solutions, and Equations (A.8) and (A.10), we can also obtain the solutions for v_c and v_f

$$
\left(\frac{v_c}{v_0}\right)_1 = \frac{1}{M_A}\frac{M_A - R_n}{1 + R_n} \qquad \wedge \qquad \left(\frac{v_c}{v_0}\right)_2 = \frac{1}{M_A}\frac{M_A + R_n}{1 + R_n} \tag{A.12}
$$

$$
\left(\frac{v_f}{v_0}\right)_1 = \frac{1}{M_A}\frac{1 + M_A}{1 + R_n} \qquad \wedge \qquad \left(\frac{v_f}{v_0}\right)_2 = \frac{1}{M_A}\frac{M_A + R_n}{M_A - R_n}\frac{M_A - 1}{1 + R_n}\,. \tag{A.13}
$$

Solution 2 leads to $v_c > v_0$ and $\alpha > 0$ for $M_A > 1$ and allows negative values for v_f, and therefore, it is not a valid solution for the system. Solution 1, in the other hand, always ensures $\alpha > 0$, $v_c < v_0$ and $v_f > v_c$. The analytical expressions on Equations (A.11) to (A.13), marked with the label '1' represent then the correct analytical expressions for the coupling parameters of the system, as a function of the initial parameters of the system.

We should note, however, that the coupling equations here presented are only valid for a set of conditions. For high Mach numbers M_A, for example, where instabilities take an important role on the dissipation of energy in the background plasma, these equations are no longer valid. Thermal effects and trapped particles were also neglected, and we assume that the plasmas are long enough to ensure a good coupling and a quasi stationary regime. Additionally, other factors, such as 3D effects, must be consider when attempting to apply these expressions to experiments. These limitations are discussed with more detail on Chapter 2.

Appendix B

Mini magnetosphere parameters

B.1 List of mini magnetosphere simulations performed

Table B.1: List of PIC simulations performed with ion-scale magnetospheres and their correspondent parameters. Run A corresponds to the simulation used for chapter 3, and it was reused for the scans of the driver density, the driver ion mass and the dipolar magnetic moment. All the simulations considered equal initial components of the thermal velocity of the particles for all directions, *i.e.*, $v_{th,x} = v_{th,y} = v_{th,z}$.

Run	v_0/c	$v_{the,x}/v_0$	$v_{thi,x}/v_0$	n_d/n_0	$m_{i,d}/m_e$	$m_{i,0}/m_e$	L_x/d_i	L_y/d_i	L_0/d_i
A/C2/D1/E2	0.1	0.1	0.01	2	100	100	2	$+\infty$	1.8
B1	0.1	0.1	0.01	2	100	100	1	$+\infty$	1.8
B2	0.1	0.1	0.01	2	100	100	4	$+\infty$	1.8
B3	0.1	0.1	0.01	2	100	100	$+\infty$	$+\infty$	1.8
C1	0.1	0.1	0.01	1	100	100	2	$+\infty$	1.8
C3	0.1	0.1	0.01	4	100	100	2	$+\infty$	1.8
D2	0.1	0.1	0.01	2	300	100	2	$+\infty$	1.8
D3	0.1	0.1	0.01	2	500	100	2	$+\infty$	1.8
E1	0.1	0.1	0.01	2	100	100	2	$+\infty$	2.3
E3	0.1	0.1	0.01	2	100	100	2	$+\infty$	1.4
F1	0.1	0.1	0.002	2	1836	1836	2	$+\infty$	1.8
F2	0.1	2.5	0.033	2	1836	1836	2	$+\infty$	1.8
F3	0.1	2.5	0.033	2	100	100	2	$+\infty$	1.8
G	0.1	0.1	0.01	2	100	100	2	6	1.8

B.2 Parameters of lunar mini magnetospheres, the LAPD experiments, and simulations

Table B.2: Typical parameters associated with lunar mini magnetospheres [4, 9, 14, 68], the range of parameters of LAPD [39] and the canonical simulation B. The parameters are written in both physical and normalized units to facilitate the comparison between the space, the laboratory environments and the PIC simulations. The experimental parameters are presented in ranges of values computed with the possible LAPD values for the flow velocity v_0, the density n_0 and the electron and ion temperatures $T_{e,0}$ and $T_{i,0}$, respectfully, of the background plasma. The plasma parameters shown for lunar mini magnetospheres are relative to the solar wind, while for the experiments and the simulations, they are relative to the background plasma. The ion data shown corresponds to only the hydrogen ions. The ion and electron gyroradii and gyroperiods for the experiments and simulations are estimated with the driver velocity v_0 and the magnetic field B_0. The magnetic field B_{std} is calculated at the standoff position, *i.e.*, at a distance L_0 from the center of the obstacle. Some driver parameters for the experiments are not represented because their values are not well known. However, we have an idea for the order of magnitude for some of these parameters [69].

Parameters	Lunar mini magnetospheres		LAPD experiments		PIC simulations
	Physical units	Normalized units	Physical units	Normalized units	Normalized units
Background parameters					
Density, n_0	—	—	$10^{12} - 10^{13}$ cm^{-3}	1 n_0	1 n_0
Mass ratio, $m_{i,0}/m_e$	—	—	—	1836	100
Ion skin depth, d_i	—	—	7−23 cm	1 d_i	1 d_i
Electron skin depth, d_e	—	—	0.2−0.5 cm	0.02 d_i	0.1 d_i
Electron temperature, $T_{e,0}$	—	—	10 eV	—	—
Ion temperature, $T_{i,0}$	—	—	1 eV	—	—
Electron thermal velocity, $v_{the,0}$	—	—	2300 km/s	7.7−11.5 v_0	0.1 v_0
Ion thermal velocity, $v_{thi,0}$	—	—	17 km/s	5.7−8.4×10^{-2} v_0	0.01 v_0
Internal magnetic field, B_0	—	—	300 G	3−9×10^{-2} $m_e c^2/ed_e$	0.67 $m_e c^2/ed_e$
Ion gyroradius, ρ_i	—	—	7−10 cm	0.3−1.5 d_i	1.5 d_i
Electron gyroradius, ρ_e	—	—	4−6×10^{-3} cm	2−8×10^{-4} d_i	0.15 d_i
Ion gyroperiod, ω_{ci}^{-1}	—	—	350 ns	1 ω_{ci}^{-1}	1 ω_{ci}^{-1}
Electron gyroperiod, ω_{ce}^{-1}	—	—	0.2 ns	5.5×10^{-4} ω_{ci}^{-1}	0.01 ω_{ci}^{-1}
Alfvén velocity, v_A	—	—	200−640 km/s	0.7−2.2×10^{-3} c	0.067 c
Driver parameters					
Flow velocity, v_0	400 km/s	10^{-3} c	200−300 km/s	0.7−1.0×10^{-3} c	0.1 c
Density, n_d	5 cm^{-3}	1 n_d	—	—	2 n_0
Mass ratio, $m_{i,d}/m_e$	—	1836	—	1836	100
Ion skin depth, $d_{i,d}$	100 km	1 $d_{i,d}$	—	—	0.7 d_i
Electron skin depth, $d_{e,d}$	2 km	0.02 $d_{i,d}$	—	—	0.07 d_i
Electron temperature, $T_{e,d}$	20 eV	—	—	—	—
Ion temperature, $T_{i,d}$	10 eV	—	—	—	—
Electron thermal velocity, $v_{the,d}$	3200 km/s	8 v_0	—	—	0.1 v_0
Ion thermal velocity, $v_{thi,d}$	54 km/s	0.1 v_0	—	—	0.01 v_0
Ion gyroradius, $\rho_{i,d}$	500 km	5 $d_{i,d}$	7−10 cm	0.3−1.5 d_i	1.5 d_i
Electron gyroradius, $\rho_{e,d}$	800 m	8×10^{-3} $d_{i,d}$	4−6×10^{-3} cm	2−8×10^{-4} d_i	0.15 d_i
Ion gyroperiod, $\omega_{ci,d}^{-1}$	1 s	1 $\omega_{ci,d}^{-1}$	350 ns	1 ω_{ci}^{-1}	—
Electron gyroperiod, $\omega_{ce,d}^{-1}$	6×10^{-4} s	6×10^{-4} $\omega_{ci,d}^{-1}$	0.2 ns	5.5×10^{-4} ω_{ci}^{-1}	0.01 ω_{ci}^{-1}
Magnetic parameters					
Alfvénic Mach number, M_A	—	—	—	0.3−1.5	1.5
Magnetic obstacle size, L_0	300 km	3 $d_{i,d}$	14−18 cm	0.6−2.5 d_i	1.8 d_i
Standoff magnetic field, B_{std}	5×10^{-4} G	0.07 $m_e c^2/ed_{e,d}$	100−600 G	0.02−0.2 $m_e c^2/ed_e$	2.0 $m_e c^2/ed_e$